Title
Structural Health Monitoring and Smart Sensing: Vibration, Acoustic, and Vision Perspectives

Author
Zare Hosseinzadeh, Ali

Publication Date
2020

UNIVERSITY OF CALIFORNIA SAN DIEGO

Structural Health Monitoring and Smart Sensing: Vibration, Acoustic, and Vision Perspectives

A thesis submitted in partial satisfaction of the requirements
for the degree of Master of Science

in

Structural Engineering with Specialization in
Structural Health Monitoring & Non-Destructive Evaluation

by

Ali Zare Hosseinzadeh

Committee in charge:

Professor Francesco Lanza di Scalea, Chair
Professor Charles R. Farrar
Professor Kenneth J. Loh

2020

The thesis of Ali Zare Hosseinzadeh is approved, and it is acceptable in quality and form for publication on microfilm and electronically.

University of California San Diego

2020

DEDICATION

To my mother

There are no enough words I can use to describe just how important my mother is to me. She gave me life, taught me, dressed me, but most importantly, she loves me unconditioanlly.

Thank you for everything.

Table of Contents

List of Figures

List of Tables

ACKNOWLEDGEMENTS

I would like to express my sincere gratitude to my supervisor, Professor Francesco Lanza di Scalea, for his valuable supports, advice, patience and extraordinary guidance of this research work. I also owe my sincere thanks to the members of my defense committee, Professor Charles R. Farrar and Professor Kenneth J. Loh, for reading the manuscript, and for insightful discussions and suggestions.

I sincerely acknowledge the Followship provided me by the Depertment of Structural Engineering at UC San Digeo. Chapter 2 of this thesis is part of the research project supported by the U.S. Federal Railroad Administration. Their support is greatly appreciated.

I would like to thank Dr. Ki-Young Koo (from University of Exeter, UK) for sharing the raw data of the experiments conducted on the structures studied in Chapter 3.

I sincerely thank my colleagues in Experimental Mechanics & NDE Laboratory at UC San Diego: Diptojit Datta, Ranting Cui, Izabela Batista, Guillermo Azuara, and Chengyang Huang, for their help and technical discussion.

Lastly but not least, I would like to thank my family, especially my mother and my elder brother, for their unconditional love and support, and also my friends at UC San Diego, Pedram Abbasi and Baharak Sayahpour, for their encouragement.

ABSTRACT OF THE THESIS

Structural Health Monitoring and Smart Sensing: Vibration, Acoustic, and Vision Perspectives

by

Ali Zare Hosseinzadeh

Master of Science in Structural Engineering with Specialization in
Structural Health Monitoring & Non-Destructive Evaluation

University of California San Diego, 2020

Professor Francesco Lanza di Scalea, Chair

Structural Health Monitoring (SHM) and condition assessment deal with inspecting the health and integrity of the monitored systems. Although robust damage detection methods have been proposed in the recent two decades, there are intensive ongoing investigations to tackle the practical and technical open challenges, such as smart sensing, sparse sensor measurements and real-time damage detection. This thesis is devoted to discussing pattern recognition and damage detection methods using vibration, acoustic and vision perspectives.

First, a machine learning-based approach is proposed for object classification by texture analysis. Bag-of-Words (BoW) and Support Vector Machine (SVM) techniques are used to extract the features and train an identifier, respectively. The method is particularly exploited for tie/ballast image classification at Rail Defect Facility of UC San Diego by mounting a high-speed camera on a cart moving with walking speed.

Second, a deterministic vibration-based method is proposed for damage quantification in the structures, using sparse sensor measurements. The estimated damages are then further tuned by repeating the proposed approach to reach more accurate results. The method is employed for damage detection in lab-scale and full-scale building structures.

Defect imaging in plates using data-driven Matched Filed Processing (MFP) is the last concept discussed in this thesis. Under the Born approximation, difference between the responses of the damaged and pristine plates is computed as the data set containing the defect’s acoustic signature, and conventional and adaptive beamformers are used to perform the MFP and localize the defect. The method is employed for damage detection in an aluminum plate.

Chapter 1: Introduction

Structural health monitoring (SHM) and damage detection have received considerable attention in the past two decades. Although engineering structures and systems are designed against common loads that they might experience in their lifetime, sudden loadings and/or unexpected situations can cause visible or internal invisible damages that adversely affect the performance and serviceability of the system. Early detection of such damages not only can prevent sudden failure, but also can help engineers to prepare cost-effective renovation plans [1–4]. Different local-scale and global-scale techniques have been developed in the literature for damage identification, localization and quantification. A complete review of these methods can be found in [5–8]. This thesis is aimed at using smart computer vision as well as acoustic sensing to facilitate the condition assessment procedure. Moreover, vibration-based concepts are employed to propose a new model updating and damage detection method using sparse sensor measurements. In the following, an overview of the materials covered in each chapter is presented.

Chapter 2 introduces a machine learning-based approach for tie/ballast image classification. First, a set of images of ties and ballasts are selected as the training data. The features of the images are extracted using Bag-of-Words (BOW) technique. Then, Support Vector Machine (SVM) is applied as a supervised learning method to train an identifier. The method is used for tie/ballast image classification based on the images captured by a high-speed camera mounted on a cart at Rail Defect Facility of UC San Diego. Besides, a deterministic signal-based method is introduced to discriminate ties and ballasts. The main idea is based on the maximum amplitude of the reflected ultrasonic waves from the surface of the objects. Non-contact air-coupled capacitive ultrasonic transducers in pulse-echo mode are used to launch waves to the surface of the ties and ballasts. Comparative studies are carried out to check the accuracy and precision of the vision-based and signal-based approaches in tie/ballast classification.

In Chapter 3, a new vibration-based method is proposed for damage localization and quantification in common civil structures. Damage is defined as changes in the stiffness of the damaged elements. Deflections of the system under a virtual unit load are estimated using the modal data of the first several modes and changes in the deflections between the pristine and damaged cases are used to estimate element-wise damages. The baseline model is updated to an Adapted Baseline (AB) model and the method is repeated to increase the accuracy of the estimated damages till the stopping criterion is satisfied. The method is based on using the full-size mode shape vectors; however, in real SHM programs the number of the sensors attached to the structure might be less than the structural Degrees of Freedom (DOFs). To tackle this problem, the perturbed force-based mode shape expansion technique is employed to expand the experimentally extracted mode shape vectors. The proposed method is validated by studying a lab-scale five-story shear building tested on a shake table, and a full-scale high-rise building structure. A parametric study is also conducted to evaluate the performance of the structural supports.

Defect imaging in plates is the subject of Chapter 4. Matched Field Processing (MFP) in a data-driven platform is used to localize defects in a plate. This method is model-free, and all the process is based on the acquired data by experiments. The pristine and damaged plates are excited using an impact induced by a hammer. Using the time history responses of the pristine plate excited in different points, the replica vectors are made. Then, a set of damage-sensitive data is extracted by subtracting the data of the pristine plate from the data of the damaged plate, and it is used to perform the MFP by means of conventional Bartlett processor as well as adaptive beamformers, like Minimum Variance (MV) and White Noise Constraint (WNC). The applicability of the method is demonstrated by testing an aluminum plate.

Concluding remarks as well as suggestions for future investigations are given in Chapter 5 of this thesis.

In this thesis, the vectors are shown by **bold small letters** while the matrices are denoted by **BOLD CAPITAL LETTERS**. Moreover, the scalers are shown by *italic letters*.

Chapter 2: Machine Learning-based Image Processing for Tie-Ballast Image Classification

2.1. Motivation and problem definition

Analyzing images' texture has been widely used for pattern recognition, abnormality detection, and object classification in different research fields [9–12]. Surface damage detection and classification in concrete slabs [13, 14], crack and deterioration detection on the surface of asphalt roads and pavements [15, 16], and micro-scale tissue image classification for biomedical pattern recognition and abnormality detection [17] are some of the research subjects that have been developed and popularized by leveraging the advances in texture analysis and machine learning.

In the present study, a machine learning-based image processing technique is proposed for tie/ballast image classification using the texture signature of the objects. This idea is a part the solution proposed in response to the necessity of developing a robust and fast speed sensing and monitoring system for the ties, which is eventually aimed at assessing the health of the wooden and/or concrete ties in the railroads. The tie deflection profile can be used to determine adverse support conditions (e.g., center binding) [18, 19]. Developing a system for tie profile imaging can reveal valuable information about the permanent or temporary deflections of the ties that can be further analyzed to establish some criteria on assessing the health of the corresponding ties. For this purpose, an array of non-contact ultrasonic transducers (in pulse-echo mode) are used to image the surface of the ties based on the Time-of-Flight (ToF) of the received waves as the reflections from the ties' surfaces. This system has been proposed by Experimental Mechanics & NDE laboratory at UC San Diego and it is under further investigations for real-time tie assessment. The system is connected to a cart (or train) and acquires the data when the train moves. Determining the object which is probed by the transducers in each instant is of importance to construct the surface profile of the ties. In general, the probed object (tie or ballast) can be identified based on the *strength* of the reflected waves. However, this idea might face uncertainties in some cases. For example, the ballasts are naturally placed in the ties' level, and it is possible that a ballast with flat surface is mistakenly identified as part of a tie if only the strength of the reflected signals are studied for object classification. On the other hand, ties with rugged surfaces (which can be a result of surface damage) may be classified as ballasts because of the observed high attenuation in the amplitude of the reflected waves. Computer vision-based image classification can be helpful in such conditions to robustly confirm the wave-based classification and surface imaging results.

Considering the distinguishable texture of the ties and ballasts, the images can be efficiently classified if their texture is analyzed. Herein, the tie/ballast image classification is considered as *texture classification* problem, and using the features extracted from a set of tie/ballast images, an identifier is trained to automatically label a given image. For this purpose, Support Vector Machine (SVM), a supervised learning technique, is employed to train an identifier based on the texture features extracted by Bag-of-Words (BoW) method.

2.2. Background

2.2.1. Bag-of-Words (BoW) model for texture representation

Texture is one of the basic features of almost all the images that can be effectively used for pattern recognition and image (object) discrimination. In the field of texture-based pattern recognition, *texture representation* is a challenging concept which has been extensively studied in the literature [20]. The texture representation methods can be divided into two main groups: Bag of Words (BoW)-based methods, and Convolutional Neural Networks (CNN)-based methods. A rich review of these methods can be found in

[20, 21]. In this thesis, BoW method is employed for texture representation and analysis. In the following, BoW model is introduced by a simple example related to the text processing.

BoW is a very simple model that has been used for feature extraction from the text documents [22]. In the field of text analysis, BoW model is defined as a representation that maps arbitrary text into fixed-length vectors which counts how many times each word appears. This process is called *vectorization*. To illustrate the main concept of BoW model, consider the following sentences as the responses of three students who have been asked to describe a course that they have in common:

- Student #1: This course is easy and practical.
- Student #2: I like this course.
- Student #3: This course covers practical concepts and I like this course.

Each of these sentences is named a *document*, which consists of several words. In the next step, using a set of “words” found in these documents, a *vocabulary* is made as below:

“this”, “course”, “is”, “easy”, “and”, “practical”, “I”, “like”, “covers”, “concepts”

In this example only one vocabulary is formed; however, the approach can be followed by forming several vocabularies with different lengths. To vectorize a given document, the count of each word in the vocabulary should be determined in the corresponding document. Table 2.1 summarizes the counts of the words in the proposed vocabulary. As a result, each document can be replaced with a 10-entry vector as follows:

Table 2.1: Counts of the words in the example documents.

Document #	this	course	is	easy	and	practical	I	like	covers	concepts
1	1	1	1	1	1	1	0	0	0	0
2	1	1	0	0	0	0	1	1	0	0
3	2	2	0	0	1	1	1	1	1	1

Document #1 = {1, 1, 1, 1, 1, 1, 0, 0, 0, 0};

Document #2 = {1, 1, 0, 0, 0, 0, 1, 1, 0, 0};

Document #3 = {2, 2, 0, 0, 1, 1, 1, 1, 1, 1}.

Utilizing the mentioned count-based vectorization, the contextual information (like the information about the order, structure or location of a specific word) is discarded. The vectorization can also be done by returning “0” or “1” per the existence of the vocabulary’s words in a document; but, count-based vectorization is more preferred because it returns relatively more information about the document.

In the field of computer vision, BoW technique (also often referred to as Bag of Features (BoF) or Bag of Visual Words (BoVW) [20]) is known as an image categorization method which assigns a category label to a given image [23]. *Texture representation* or *texture feature extraction* is the most important part of this technique, which is defined as a transformation to map the texture of the input image into a *feature vector* describing the main properties of the texture. Using different combination of the “visual” words, different visual vocabularies are formed, which are subsequently used to make a *codebook* (or visual *dictionary*), and this codebook can then be used to map the features from local level to global level (entire) of the image. It is important to mention that generally, analyzing sparse vectors (i.e., vectors with considerable zero entries) can be problematic because of making singular (degenerate) matrices. To tackle this issue, visual vocabularies should be selected in a way that such sparsity is minimized. In the following, different steps of the BoW model for texture analysis are summarized [20, 23]. These steps have been schematically shown in Figure 2.1.

1. **Defining local patches:** In the first step, the input image is divided into a pool of *N* image patches over a regular fixed grid [24], interest point detector-based segmentation or randomly sampled patches [25]. In the present study, a fixed gird is used to define the local patches.

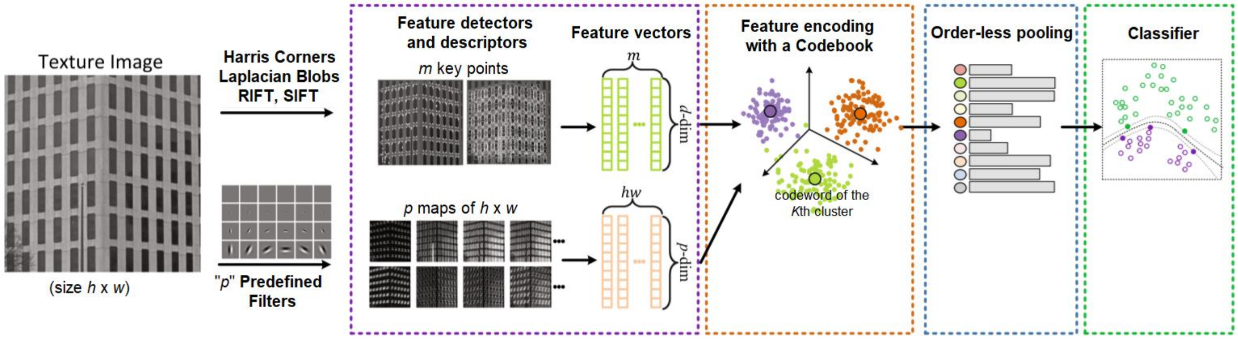

Figure 2.1: Different steps of BoW technique for image analysis (adapted from [20], with some revisions).

2. **Patch representation in the local level:** Texture representation cannot be formed over a single pixel because the texture is a *spatial* phenomenon [20]. Thus, texture pattern in local level (which is a texture representation over local pixel neighborhoods) should be mapped into the global representation of an image to return an accurate texture representation of the entire image. For this purpose, the texture is first transformed to a *pool of local features*, which are then aggregated to make a global representation of the entire image. In the present step, local representation is formed for the extracted N patches in step 1. A set (or pool) of texture features is produced by applying the local texture descriptors to the N patches. Assuming the features of D dimension, the local features of the ith patch in an image is denoted as $\mathbf{x}_i \in \mathbb{R}^D$, where i=1, 2, …, N. To have a successful BoW model, the local descriptors should be distinctive and robust to the possible image transformations (like scale, blur, rotation, illumination, and changes in the viewpoint) [20].
3. **Codebook generation:** In this step, a set of codebooks (i.e., visual dictionaries) is generated using the training data. *Clustering* is a common method to learn a visual vocabulary or codebook. In this study, the K-means clustering technique is leveraged for this purpose and the center of each cluster is defined as a *codeword* (or visual word), denoted by $\mathbf{y}_j \in \mathbb{R}^D$, where j=1, 2, …, K.
4. **Feature encoding:** This step is devoted to mapping each local feature $\mathbf{x}_i$ into one or several codewords, forming a *feature coding vector*, $\mathbf{w}_i \in \mathbb{R}^K$. Feature encoding links local feature

representation to the global feature representation, and it can affect not only the accuracy, but also the speed of the classification method.

5. **Feature pooling:** In this stage, the global feature representation $\mathbf{z}_i$ is achieved for a given image by aggregating the coded feature vectors (i.e., $\mathbf{w}_i$). Note that the properties of texture are usually translationally invariant, and this allows order-less aggregation of local texture features, by operators like the weight-less summation [20, 21, 23]. The results of this stage are presented as a histogram of the codewords frequency for the given test image.

The histogram of the feature frequency in the global level is then used as the basis for classification. Different approaches like Nearest Neighbor Classifier (NNC), Support Vector Machine (SVM), Neural Networks (NNs) and Random Forests (RF) can be employed to train the classifier [21]. In this study, SVM is used as a supervised learning approach.

2.3. Field tests

The field tests were conducted at the Rail Defect Testing Facility of UC San Diego. A high-speed camera was mounted on the prototype attached to a cart to capture the images of the ties and ballasts (see Figure 2.2). The camera holder (blue ring around the camera shown in Figure 2.2) has a special shape which can hold the camera after rotating by –45°. The prototype (designed by Experimental Mechanics & NDE Laboratory at UC San Diego for tie deflection measurement) consists of six capacitive air-coupled ultrasonic transducers (VN Instruments CAP-2) with a central frequency of 135 kHz. The camera is a Basler acA 1300-200uc (USB3.0 version), with an ON semiconductor, Python 1300 Complementary Metal-Oxide-Semiconductor (CMOS) sensor, which can deliver up to 200 frames per second (FPS) with 1.3 Megapixel resolution. The lens of the camera is a Kowa, 1/1.8" Format, Manual Iris version. The focal length of the lens is 4.4-11mm, with a zoom ratio of 2.5x. Based on the existing standards, at least 3" clearance above the surface of the rails is needed for equipment installation, which was considered in prototype design (see Figure 2.3(a)). The distance between the sensors/camera and top surface of the ties is ~11.5". The encoder is connected to the left side of the cart and it is in contact with the front wheel as shown in Figure 2.3(b). The tests were conducted by running the cart with walking speed over nine ties, with a total path length of 20 ft. As the cart moves, the encoder rotates and subsequently the sensors and camera are triggered by the encoder pulse with a 0.25" resolution.

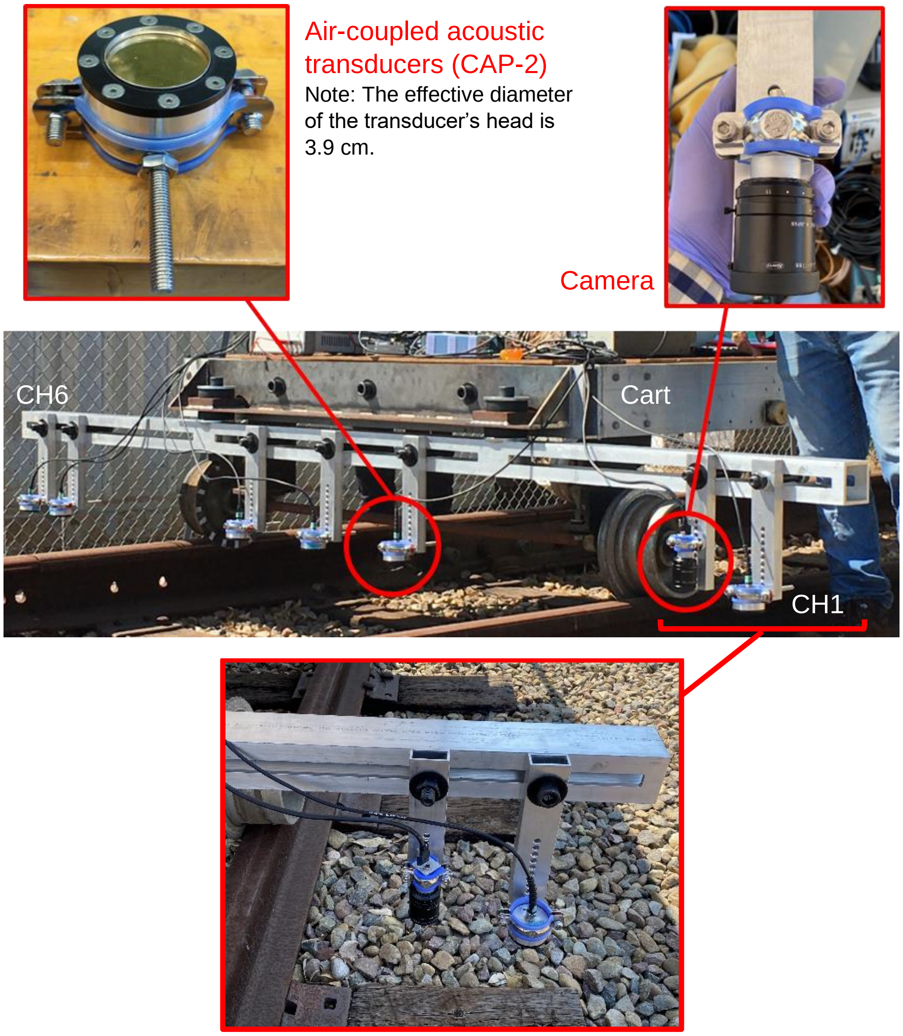

Figure 2.2: The camera mounted on the prototype. ‘CH1’ and ‘CH6’ denote the first and sixth transducers attached to the prototype. CH1 is fixed at a distance of 6" from the right edge of the hollow beam. The distance between the camera and CH1 is 6".

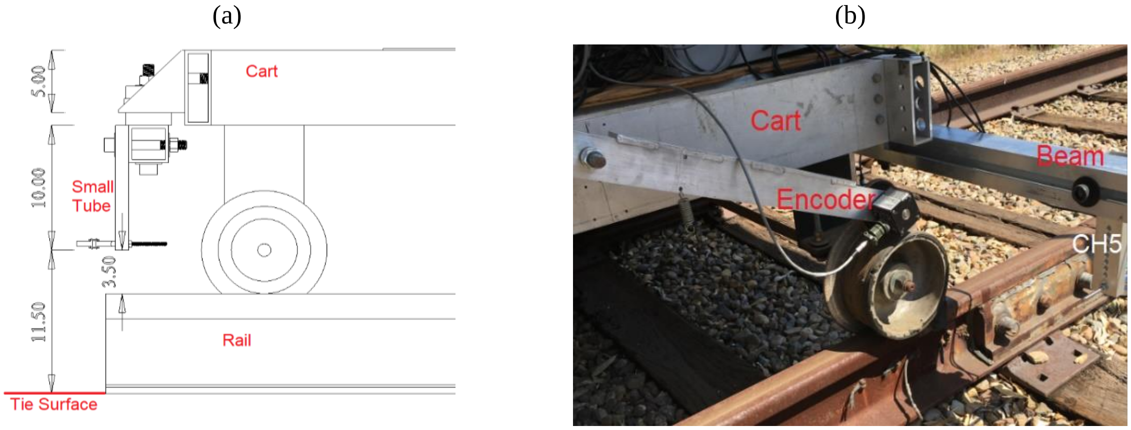

Figure 2.3: (a) Key dimensions of the prototype (unit: inch): the camera is placed ~11.5" above the tie's surface, with a clearance of ~3.5" from the top surface of the rail. (b) Encoder: the transducers and sensors are triggered by an encoder with 0.25" resolution.

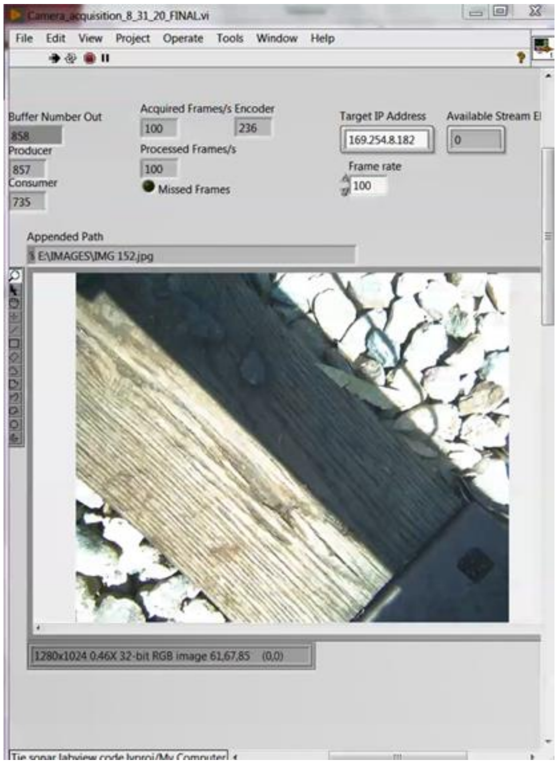

Buffer Number Out 858
Producer 857
Consumer 735
Acquired Frames/s 100
Encoder 236
Processed Frames/s 100
● Missed Frames
Target IP Address 169.254.8.182
Available Stream El 0
Frame rate 100
Appended Path E:\IMAGES\IMG 152.jpg
1280x1024 0.46X 32-bit RGB image 61,67,85 (0,0)
Tie sonar labview code.lvproj/My Computer

Figure 2.4: Front panel of the LabVIEW routine for the camera during a test.

Figure 2.4 shows the front panel of the LabVIEW program developed to communicate with the camera. The camera is connected to a SuperSpeed (SS) USB3.0 port on the computer, which provides the camera with both power supply and fast speed data transmission path. Running the developed LabVIEW code, the camera turns on, and grabs images based on the encoder count number. The encoder count number comes through a network communication with the LabVIEW routine developed for the transducers[1] and this number determines the name of the images which is saved as “jpeg” file in the computer system. If the encoder stops, the count number remains constant and the image is overwritten with a name of that count. The camera frame rate can be controlled through the front panel of the LabVIEW routine (see Figure 2.4). In this field test, the camera was set to grab 100 FPS, which is a reasonable frame rate for the walking speed test.

The code is executed based on a stop command which is issued by the user through the LabVIEW routine of the signal acquisition part. Therefore, the camera’s LabVIEW routine constantly checks the commands through the network communication in terms of receiving the stop command. As soon as this command is received, the camera stops image acquisition; but the code continues running until all the inline images are successfully saved in the hard drive.

2.4. Tie/ballast image classification method

In this section, the details of the computer vision-based tie/ballast image classification method are presented.

2.4.1. Preparing images for analysis

Figure 2.5 shows a typical image captured by the camera. A rotation in the view field of the camera is seen because the camera was rotated by –45° to be rigidly kept by the holder (discussed in section 2.3).

---

[1] Note that the transducers’ LabVIEW routine is the host routine which manages the developed LabVIEW routine for the camera.

Figure 2.5: A typical image captured by the camera.

Therefore, the image captured by the camera should be rotated back to its original configuration before analysis. Also, the image has a wide field of view; however, the Region of Interest (ROI) is a circle equivalent to the transducer’s effective area (a circle with 3.9 cm diameter), located at the center of the rotated image. Therefore, the image should be cropped and focused on the ROI. To crop the image, the actual travelling distance was converted into the pixel domain because the images are in the pixel domain. For this purpose, a couple of points in an image were selected and tracked in the next successive image. Then, pixel-domain displacement was mapped into the actual physical displacement computed by the encoder’s pulse generation frequency as follows. The pixel-domain displacement of a given point in two successive images (which are the images corresponding to two successive encoder counts) was equal to 0.25" —the encoder sends out a trigger pulse in every quarter inch of displacement. A point tracker method was employed to extract the pixel-domain displacements. There are different point tracking algorithms in the field of computer vision. In this study, the Kanade-Lucas-Tomasi (KLT) tracker [26] was employed. In the following, the fundamentals of the KLT tracker are briefly explained.

The mathematical derivation of the KLT method can be found in [26]. The main idea is based on minimizing the Euclidean distance between two image patches by gradient search. Here, the concept is illustrated with a 1D problem by tracking a point on a curve. It is assumed that curve *I* and *J* (shown in Figure 2.6) are two images of a given curve in two successive frames, which are displaced with h. From camera specification viewpoint, h is inexplicitly proportional with the camera's frame rate. The error between these curves, *e* = *I*–*J*, has also been depicted in Figure 2.6. This error in the domain *W* can be defined as follows [27]:

$$\epsilon(h) = \int_W \left(I\left(x+\frac{h}{2}\right) - J\left(x-\frac{h}{2}\right)\right)^2 dx \tag{2.1}$$

Taylor expansion of *I* and *J* around *x* yields:

$$I\left(x+\frac{h}{2}\right) = I(x) + \frac{h}{2}I'(x) + O(h^2) \tag{2.2a}$$

$$J\left(x-\frac{h}{2}\right) = J(x) - \frac{h}{2}J'(x) + O(h^2) \tag{2.2b}$$

The derivatives of *I* and *J* are computed by expanding the Taylor series for Eqs. (2.2a) and (2.2b) as follows:

$$I'\left(x+\frac{h}{2}\right) = I'(x) + \frac{h}{2}I''(x) + O(h^2) \tag{2.3a}$$

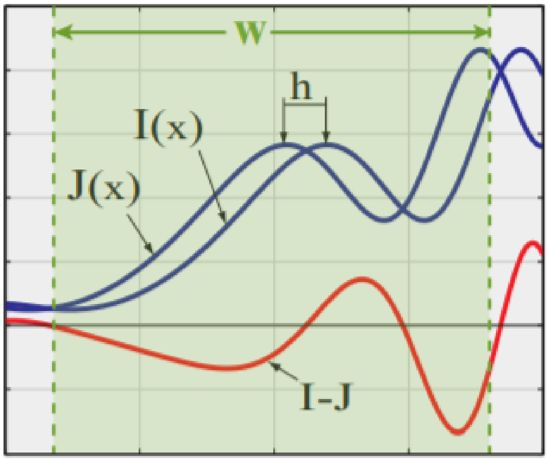

Figure 2.6: Mathematical derivation of the KLT tracking method for a simple 1D problem (adapted from [27]).

$$J'\left(x-\frac{h}{2}\right)=J'(x)-\frac{h}{2}J''(x)+O(h^2) \tag{2.3b}$$

To minimize the error $\epsilon(h)$ (Eq. (2.1)), its derivation with respect to h is set to be 0:

$$\frac{d\epsilon}{dh}=\int_W \left(I(x)+\frac{h}{2}I'(x)-J(x)+\frac{h}{2}J'(x)+O(h^2)\right)$$
$$\times\left(I'(x)+\frac{h}{2}I''(x)+J'(x)-\frac{h}{2}J''(x)+O(h^2)\right)dx=0 \tag{2.4}$$

From Eq. (2.4), the following equation system is derived:

$$\int_W \big(I(x)-J(x)\big)\big(I'(x)+J'(x)\big)dx$$
$$=\frac{h}{2}\int_W \left(\big(I(x)-J(x)\big)\big(I''(x)-J''(x)\big)+\big(I'(x)+J'(x)\big)^2\right)dx+O(h^2) \tag{2.5}$$

In Eq. (2.5), the term $(I(x)-J(x))(I''(x)-J''(x))$ can be discarded because: (1) if $h\to 0$, $(I'(x)+J'(x))^2 \gg (I(x)-J(x))(I''(x)-J''(x))$; (2) the term is computationally heavy; and (3) if h is large enough, scale pyramids can be used to reduce the resolution, and in the lower resolution, h gets small enough again to make the term ignorable [27]. Defining $g(x) = I'(x)+J'(x)$, $e = 2\int_W(I(x) - J(x)).g(x)dx$, and $Z = \int_W g^2(x)dx$, Eq. (2.5) is shorten as:

$$Z.h=e \tag{2.6}$$

Solving Eq. (2.6), the translation h can be achieved. Following similar strategy, the translational vector **h** is computed for 2D problems (like tracking points in successive frames of a footage stream) as follows:

$$\mathbf{Zh}=\mathbf{e} \tag{2.7}$$

where,

$$\mathbf{Z}=\int\int_W \begin{bmatrix} g_x^2 & g_x.g_y \\ g_y.g_x & g_y^2 \end{bmatrix} d\mathbf{p} \tag{2.8a}$$

$$\mathbf{e} = 2.\int\int_{W} \begin{bmatrix} (I-J)g_x \\ (I-J)g_y \end{bmatrix} d\mathbf{p} \qquad (2.8b)$$

In this study, the KLT tracker embedded in MATLAB computer vision toolbox (with some adjustments) is employed to convert the physical displacements to the pixel-domain displacements. First, the RGB image sequences are converted to grayscale format, where the hue and saturation information is eliminated and only the luminance of the images is retained. Then, an area in the image's field of view (in the first image of the sequence) is selected and the robust trackable features (points) are automatically identified. Here, the Speeded-Up Robust Features (SURF) algorithm [28] is used to find blob features. The robust trackable points are basically corner points that do not suffer from any aperture problem. In the next step, the shift (displacement) of the trackable points in the successive images are tracked. The framework of the tracking approach is based on local optimization, which was illustrated before in a 1D example and generalized for a typical 2D problem (Eqs. (2.1) to (2.8)). A squared distance criterion over a local region with respect to the transformation parameters is used to define the objective function. Then, the point displacement is approximated with a linear term using Taylor series. In the present application, the mentioned framework is used to track the 2D in-plane displacement of the robust trackable points in the successive images.

2.4.2. Training the tie/ballast identifier using Support Vector Machine (SVM)

The cropped images are used to train an identifier using the Support Vector Machine (SVM) method. The SVMs are supervised learning methods, which employ data analysis and pattern recognition for classification and regression analysis by building a set of hyperplanes to classify all the inputs into a high-dimensional or even infinite spaces [29, 30]. The SVM methods can be categorized based on the structure and attributes of the embedded classifier. A complete review of SVM methods can be found in [29–32]. The SVM with linear classifier is one of the well-known SVM methods which uses one hyperplane for classification purposes. The main concept of a typical SVM method is schematically shown in Figure

2.7. Based on this figure, the closest values to the classification margin are known as support vectors and an SVM is aimed at maximizing the margin between the hyperplane and the support vectors [29].

Given a labeled training data set (which means supervised learning), the SVM's output is an optimal hyperplane classifying the new examples. In the present study, the texture of the object is used to extract the main image features for training an identifier. Specifically, two key features are extracted: the 2D Fast Fourier Transform (2D FFT) and the histogram of the visual words. These two features are studied to check their suitability in terms of classifying a given test image. In Table 2.2, the 2D FFT and histogram of 100 visual words for a sample image of tie and ballast are shown. The magnitude of the dominant frequencies forms a trace which can be employed for tie/ballast classification. Moreover, the details of the histograms extracted for the ties and ballasts can be used as an effective index for image classification. In general, the histogram of the ties is sparse, with almost a constant number of appearances for the visual words. However, the histogram of the ballasts reveals a complex combination of different visual words. This trend is justifiable if the visible texture of the ties is compared with the visible texture of the ballasts. For this, it is assumed that reconstructing the texture of the ties and ballasts is desired. The texture of a wooden tie can be constructed by repeating a limited number of special visual units because its texture is unique and periodic. Ballasts, however, have more complex texture that a combination of different visual units is needed to reconstruct an image of the ballasts. Therefore, it is concluded that both the 2D FFT and histogram of the visual words can be suitable features to classify ties and ballasts.

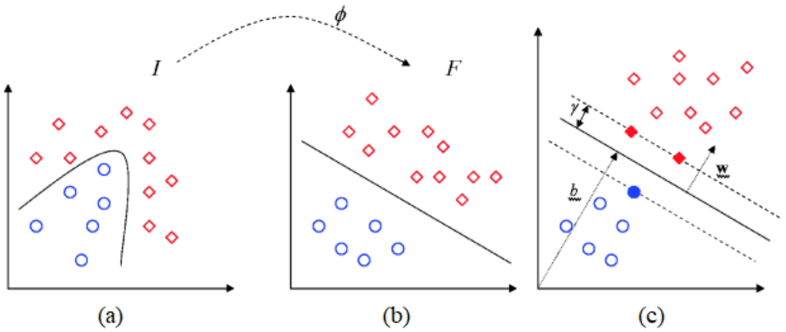

Figure 2.7: The SVM method: (a) Simplifying the classification task by feature map, (b) hyperplane to separate the data, and (c) maximal margin hyperplane with its support vectors [30].

Table 2.2: The 2D FFT and histogram of visual word occurrence for a typical tie and ballast image.

Object	Tie	Ballast
		
2D-FFT	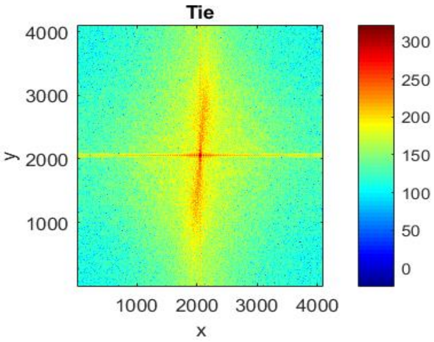	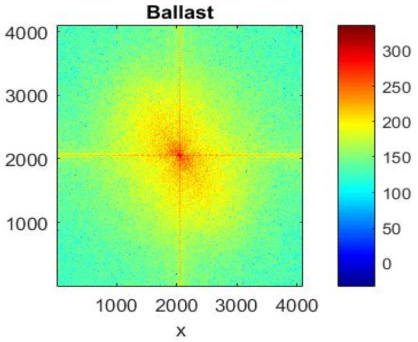
Histogram of visual words	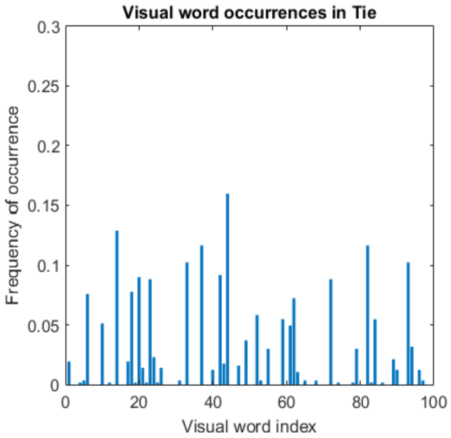	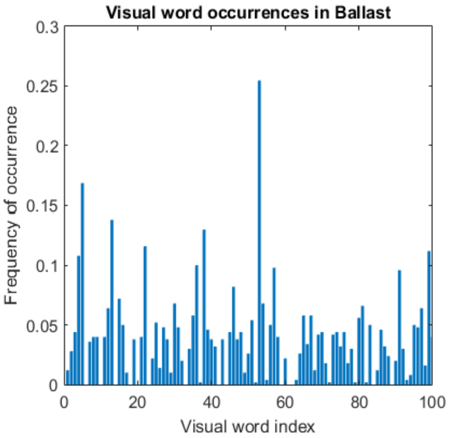

2.5. Implementation, results and discussion

In this section, the proposed method is employed for tie/ballast image classification by analyzing the images captured at the Rail Defect Testing Facility of UC San Diego. A 20 ft-long segment of the railroad was monitored in five independent tests using a data acquisition system consists of six CAP-2 ultrasonic transducers —the platform for non-contact fast-speed tie assessment system—, and a camera. The details of the tests as well as the data acquisition system were discussed in section 2.3.

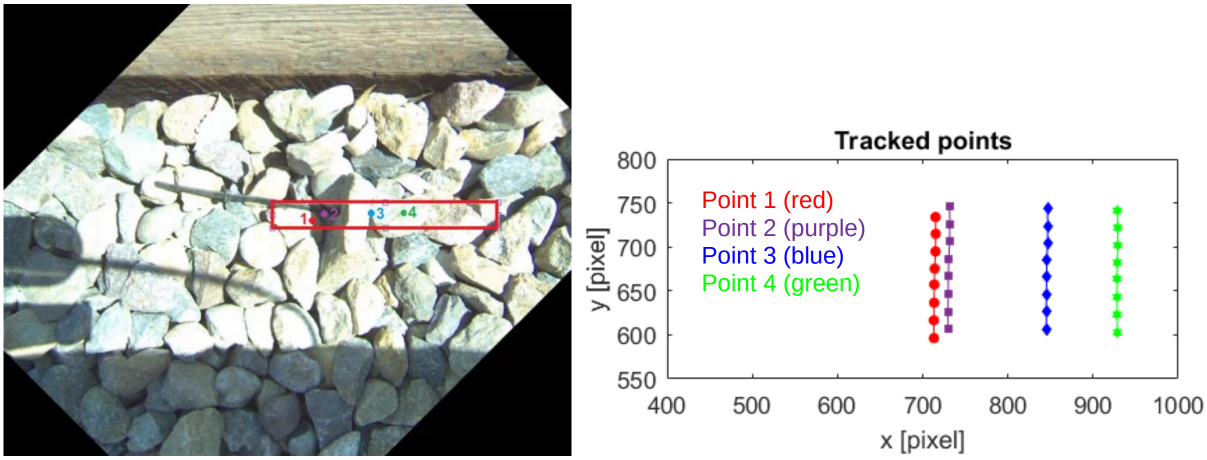

Figure 2.8: Tacking automatically selected robust features in eight successive images by the KLT tracker.

The proposed machine learning-based image classification method was discussed in detail in section 2.4. To implement the method, at first step, the KLT tracker was used to map the actual travelling distance into the pixel domain. Figure 2.8 shows the selected zone as well as the automatically selected robust points (denoted by numbers 1 to 4). These points were tracked in 8 successive images and the pixel-domain displacements are plotted in Figure 2.8. The tracked points reveal straight traveling lines, with no lateral movements. The displacement of any of the tracked points in two successive images should be equal to 0.25". Using this criterion, it is concluded that every 20 pixels on the images is equivalent with 0.25". Therefore, the ROI in the pixel domain will be a circle (at the center of the rotated images) with a diameter of 122.84 pixels. Using this information, the images were prepared for the analysis.

Figure 2.9 shows the details of image preparation for a typical image: the image is rotated by 45° to be in the original *x*-*y* plane. Then, only the ROI is cropped and is saved as a new image. Note that all the procedure is done in MATLAB [33] using functions of the Computer Vision toolbox.

In the next step, sample images of the ties and ballasts (cropped images, focused on the ROI) are randomly selected among all the images and the identifier is trained using the SVM method. The initial evaluations indicated that using 2D FFT and histogram of the visual words, an effective set of features can be extracted for the classifier training step (see section 2.4.2). However, detailed investigations revealed th-

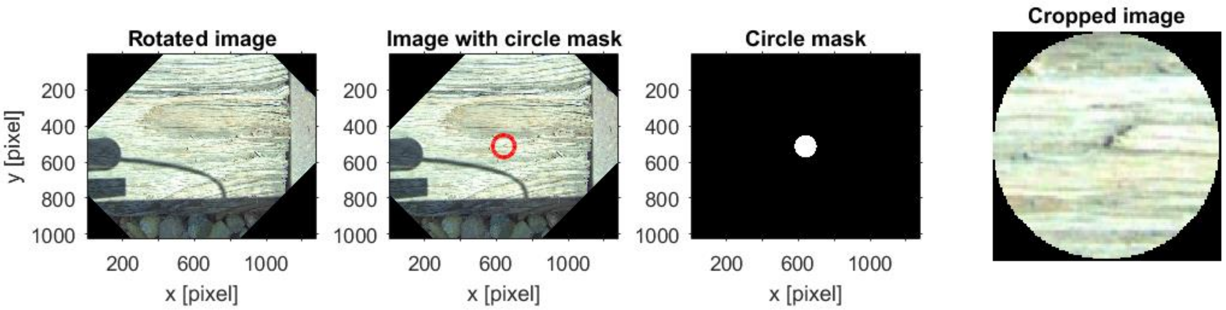

Figure 2.9: Preparing images for analysis.

-at 2D FFT not only decreases the speed of the image evaluation because of the required side computations, but also cannot add much more distinguishable details in some cases. Because of the relatively small ROI, in some cases the edges of the ballasts produce locally aligned textures and the associated 2D FFT is almost like the 2D FFT of the ties. On the other hand, the machine learning toolbox of MATLAB has accelerated functions for BoW algorithm which include the SVM method. Therefore, the speed of the training part is considerably increased if only the histogram of the visual words is employed as the texture features. In the following, the optimal training system was programmed using the histogram of the visual words as the object's features.

In tests #1, 3, 4, and 5, about 4% of all the images (i.e., 20 images of the ties and 20 images of the ballasts) and in test #2, about 3% of all the captured images (i.e., 15 images of the ties and 15 images of the ballasts) were used to implement the proposed method. In test #1, for example, 24576 features were totally extracted for each category (i.e., ties and ballasts) and 80% of the strongest features for each category was selected to make 500 visual vocabularies using *K*-means clustering approach. The confusion matrix of the evaluation process for the test set, as well as another set of 40 randomly selected images, revealed that the trained classifier has an accuracy equal to 100%.

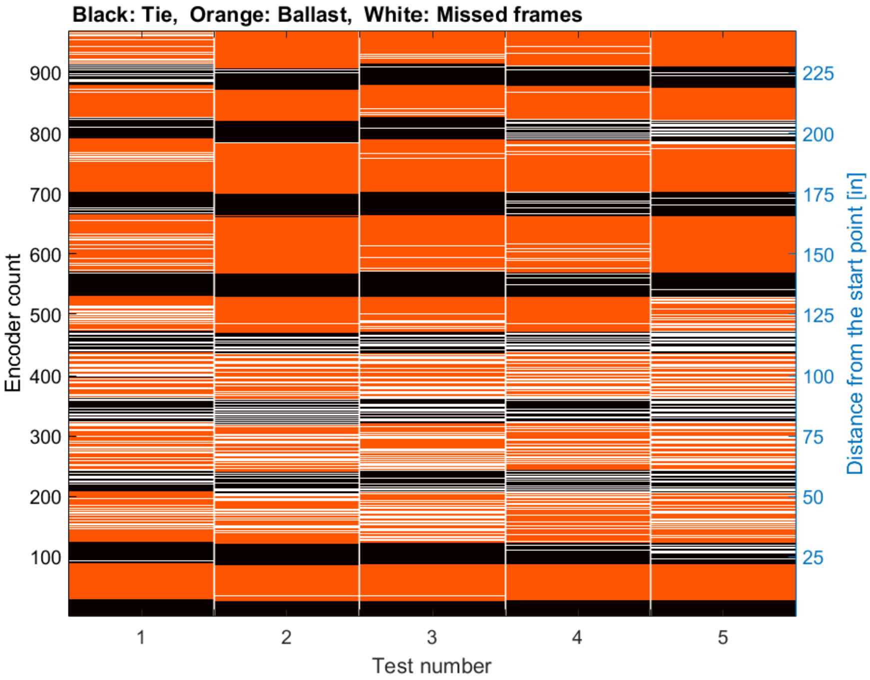

Figure 2.10: Tie/ballast classification using image-based approach.

For each test, the explained procedure was repeated, and the trained classifier was used to classify the tie/ballast images. Figure 2.10 shows the classification results for all the five tests. Ties and ballasts are plotted with black and orange colors, respectively. The width of each cell in vertical direction is equal to one count of the encoder (i.e., 0.25"). The results indicate that the method can properly classify ties and ballasts in different tests. Moreover, the number of the identified ties (9 ties) and their width match with the field observations. In the results shown in Figure 2.10, white cells represent the "*missed*" frames. That is because of the current buffer size that limits the effective frame rate. To tackle this issue, a couple of solutions are suggested as follows:

(1) Increasing the buffer size by saving the captured images in a Real-Time Performing System (RTPS): This solution relies on a promotion in the hardware. Generally, PXIs/PXIes with RTPS can be used to save the images with higher buffer size comparing with the regular systems. This

solution is effective only if a GigE version of the camera is used. Note that in the present research, USB3.0 version of the camera was used which is not compatible with RTPS. This idea is under further investigations by Experimental Mechanics & NDE Lab at UC San Diego.

(2) Extracting the ROI of the missed images from the last successfully captured/saved image: Generally, there are overlaps among the successive images captured by the camera. The proposed method uses central segment of the *i*th image as the ROI_i. Because of the overlap between two successive images, the ROI in the (*i*+1)th image can be extracted from the *i*th image. This idea can be used to tackle the mentioned missed frames issue.

In the following, the missed frames are recovered using the suggested solution (2). As an illustrative example, missed frames #153 and 155 in test #1 are recovered using frames #152 and 154, respectively. Figure 2.11 shows frames #152 and 154 with the corresponding ROIs, as central circles with diameter of 122.84 pixels (the red circles). The center of the ROI_{153} and ROI_{155} can be reached by shifting the center of the ROI_{152} and ROI_{154} by 20 pixels (equal to the encoder's resolution, which is 0.25") along *y* axis, respectively (blue circles in Figure 2.11). Figure 2.12 shows the focused ROI for frames #152, 153, 154, 155, and 156. Visually inspecting the movement of the ballasts in the ROIs reveals the accuracy of the suggested solution to tackle the missed frames issue. The idea can also be generalized to find the optimal number of the images needed to cover the entire test path. Figure 2.13 shows frame #152 containing ROI_{152} and all the next ROIs that can be extracted from this frame. The ROIs for the next 22 images can be extracted using only top half of the image #152 (see Figure 2.13). Therefore, in each 24 counts of the encoder, one image should be captured and saved. Note that in this calculation only half of each image is used to extract the ROIs of the next frames. This generalized idea is under implementation for another field test at the Rail Defect Facility of UC San Diego.

In the following, the illustrated solution in Figure 2.11 is employed to tackle the missed frames issue. Figure 2.14 shows the tie/ballast image classification results for the case that the missed frames are extracted from the last existing images. There is a full accordance between the general appearance of the ties/ballasts in this figure and in the original results reported in Figure 2.10. Moreover, the accuracy and precision of the suggested solution for recovering the missed frames are approved by the results summarized in Figure 2.14.

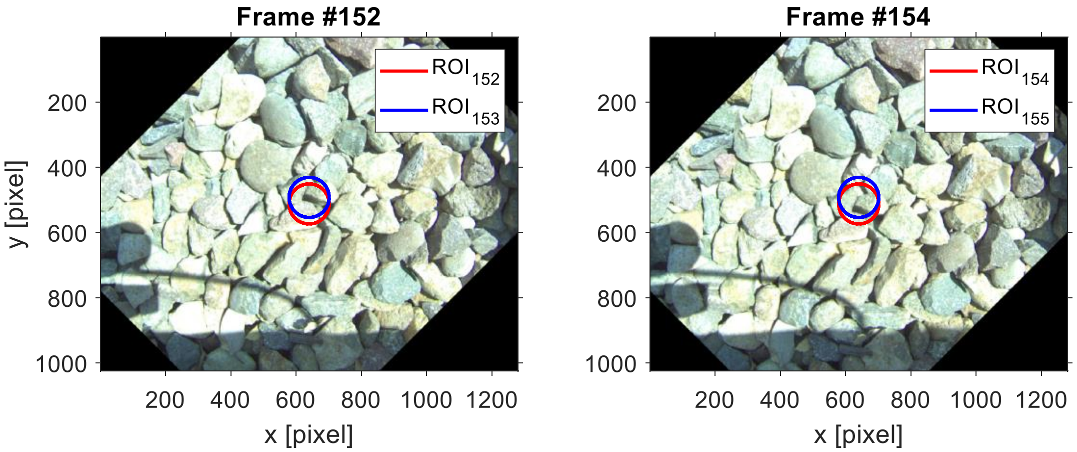

Figure 2.11: The ROIs for frames #152, 153 (missed frame), 154, and 155 (missed frame), in test #1.

Figure 2.12: The ROIs for frames #152–156 in test #1. ‘*’ denotes the frames which were originally missed and recovered by analyzing the previous captured images.

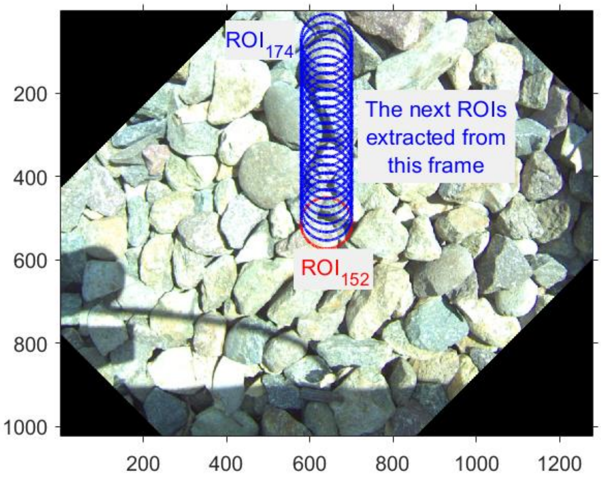

Figure 2.13: Image #152 (test #1): ROI$_{152}$ and the subsequent 22 ROIs that can be extracted from this image.

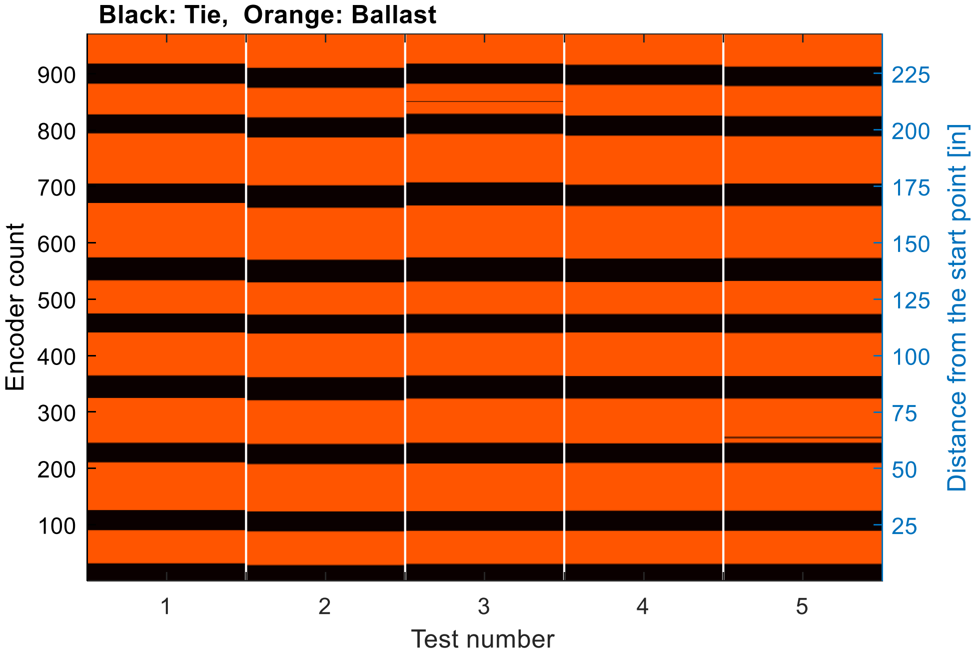

Figure 2.14: Tie/ballast classification using image-based approach. Missed frames has been recovered from the last existing images.

This section ends with a study to compare the performance of the proposed image-based method with a signal-based approach for tie/ballast classification. The signal-based classification method is derived by tracking the *amplitude* of the reflected waves. The ultrasonic transducers (in pulse-echo mode) send waves out and receive the reflected waves. Based on the amplitude of the reflected waves, the nature of the reflecting surface can be identified. The ballasts are in chaotic shapes, sizes and orientations, which result in highly scattered reflections. Therefore, a highly attenuated signal is expected to be received as the reflected waves from the ballasts' surface, which appears as a signal with low amplitude. Comparing with the ballasts, the ties' surface is much flatter, which result in relatively low attenuation (i.e., low-level scattering) or large amplitudes. Figure 2.15 shows typical reflections from the ties' and ballasts' surfaces, which confirms the described amplitude changes of the reflected waves. Therefore, ties and ballasts can be identified based on the amplitude of the reflected waves.

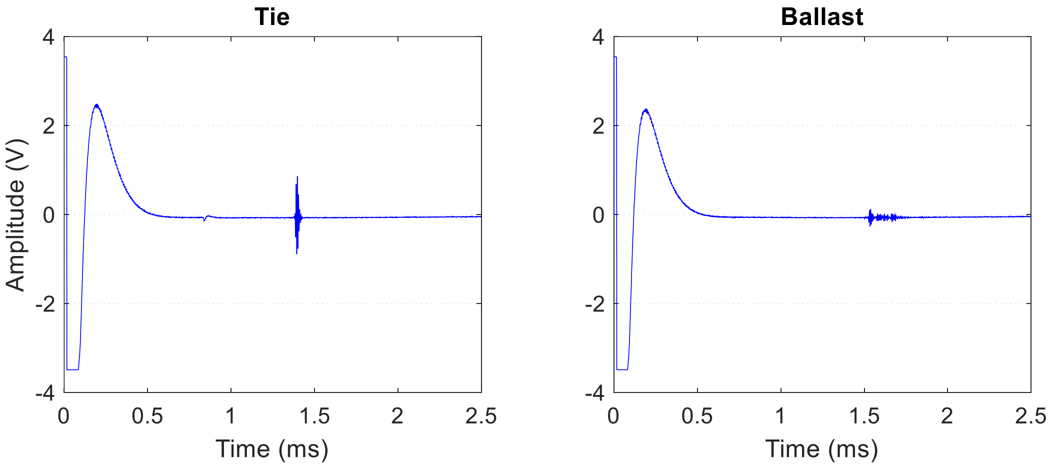

Figure 2.15: Typical reflected ultrasonic waves from the surface of the wooden ties and ballasts.

Two comparative studies are conducted to evaluate the performance of the image-based and signal-based tie/ballast classification methods. In the first comparative study, the signal-based classification is applied to the entire array of the transducers (the main platform developed for measuring the tie deflection —see section 2.3) and a probed surface is labeled as tie if at least four transducers report a reflected wave with an amplitude greater than 0.75 V. The signals were acquired in test #2 using six transducers on the array. Figure 2.16 shows the obtained results using signal-based and image-based methods for this test. In the image-based approach, not only the original set of images (i.e., images with the missed frames), but also the fully recovered set of images were used for tie/ballast image classification. First, it is re-emphasized that the robustness of the suggested approach to recover the ROIs of the missed frames is confirmed based on the results. Comparing image-based and signal-based methods, in general, there is a good agreement between the two methods. In the signal-based method, however, tie #8 is not identified. The field observations revealed that this tie is *not aligned* with the array of the transducers (see Figure 2.17). As a result, the acoustic reflections from the tie do not reach to multiple transducers simultaneously, and the signal-based tie identification approach fails.

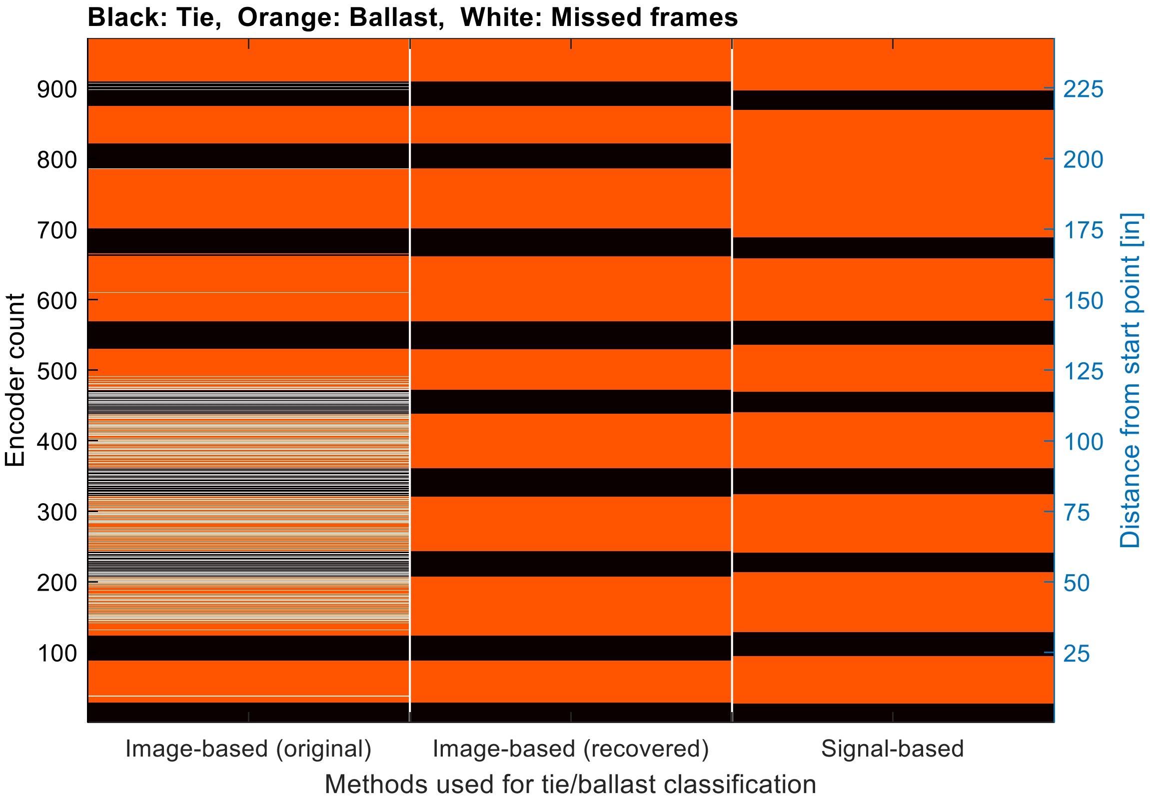

Figure 2.16: Comparison between image-based and signal-based approaches for tie/ballast classification in test #2. The signal-based classification is based on analyzing the signals received by all the transducers on the array.

Figure 2.17: Misalignment of tie #8. The box denoted by ‘C’ shows the area scanned by the camera.

The second comparative study is devoted to investigating the performance of the image-based method compared with the signal-based approach by analyzing the signals acquired by transducer #1 (located next to the camera, denoted by CH1 in Figure 2.2). To study the effects of the threshold value in signal-based tie/ballast classification, two different thresholds (0.6 V and 0.75 V) are considered. If the amplitude of the received signal is greater than these thresholds, the reflecting surface is labeled as tie. Otherwise, it will be labeled as ballast. Figures 2.18 and 2.19 show the obtained results for test #2 and #5, respectively. Note that in these figures, the image-based identification has been applied to the full set of images, including the recovered ROIs of the missed frames. Similar to the first comparative study, there is acceptable accordance between signal-based and image-based classification methods. Regardless the selected threshold value, tie #8 can be identified in the signal-based method because the misalignment issue cannot be realized by only one sensor. However, some of the ballasts have been mistakenly labeled as ties which is probably because of having a reflecting surface similar to the ties’ surfaces. Moreover, the signal-based classification method depends on the selected threshold.

Based on the obtained results in the discussed comparative studies, the vision-based method can be considered as a useful back-up to the signal-based method for tie vs. ballast discrimination.

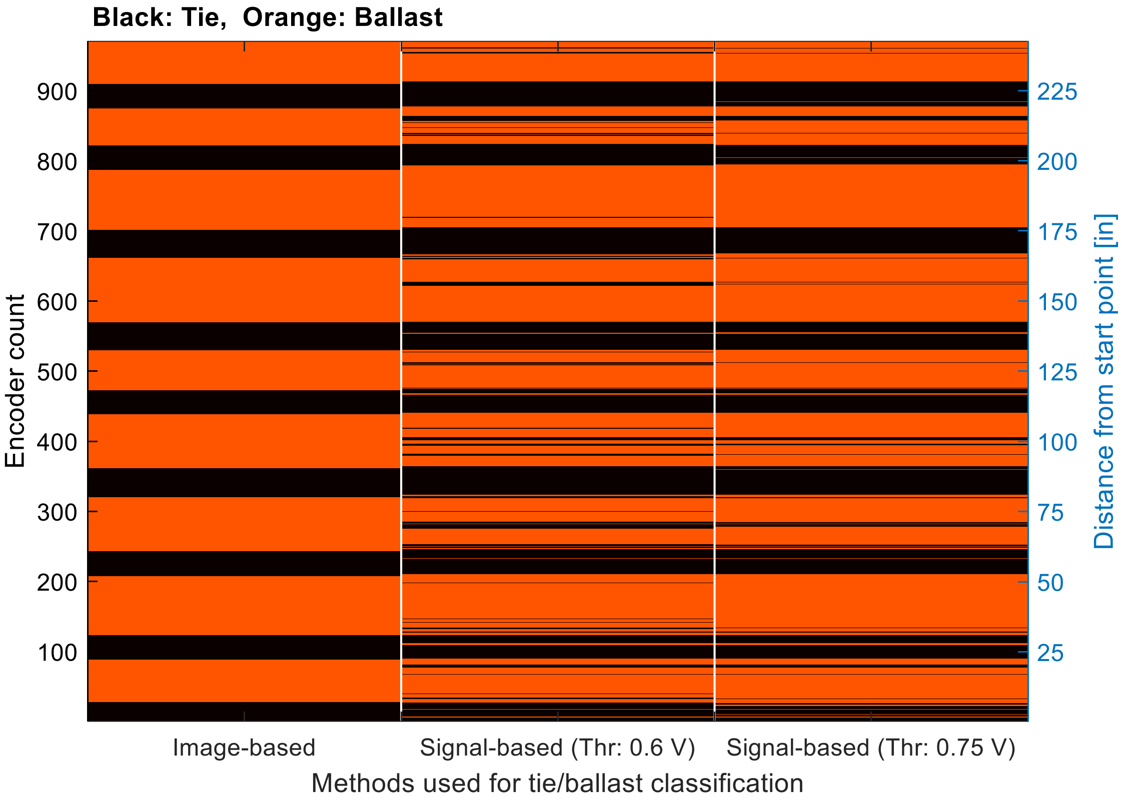

Figure 2.18: Comparison between image-based (containing the recovered ROIs of the missed frames) and signal-based approaches for tie/ballast classification in test #2. In the signal-based approach, the signals acquired by transducer #1 (denoted by 'CH1' in Figure 2.2) were analyzed. 'Thr' denotes the selected threshold (amplitude) that is used for tie/ballast discrimination.

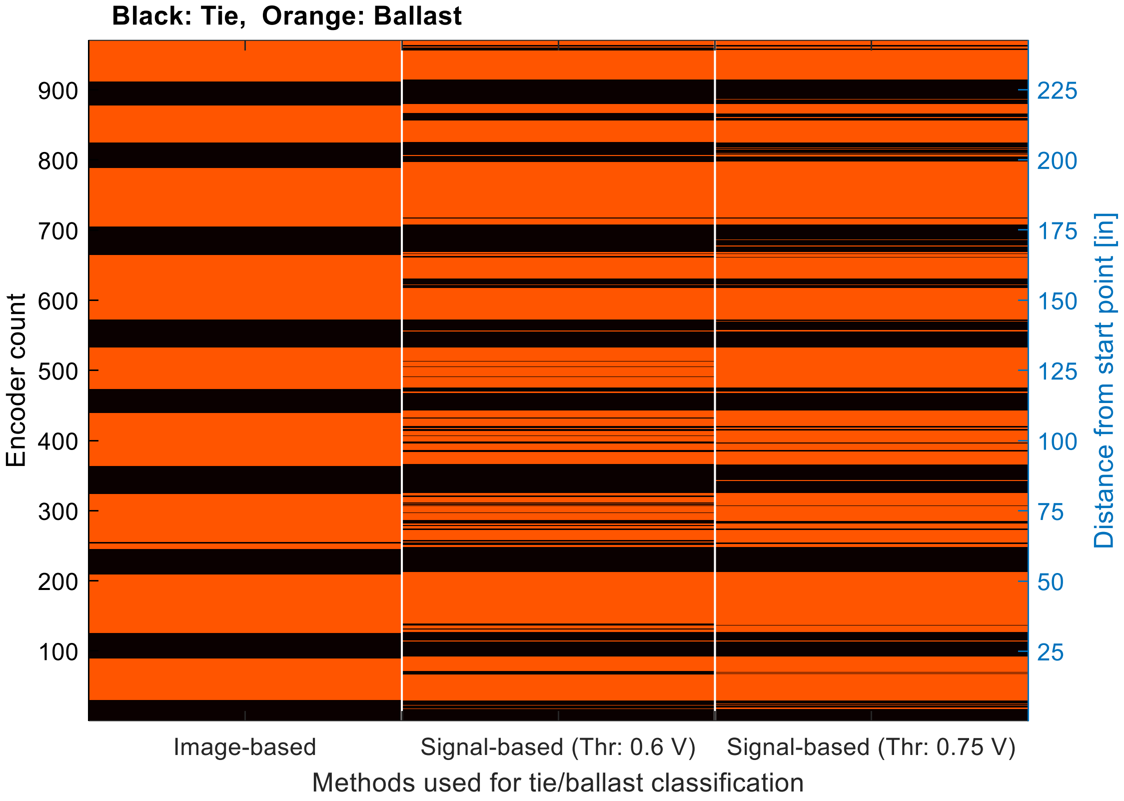

Figure 2.19: Comparison between image-based (containing the recovered ROIs of the missed frames) and signal-based approaches for tie/ballast classification in test #5. In the signal-based approach, the signals acquired by transducer #1 (denoted by 'CH1' in Figure 2.2) were analyzed. 'Thr' denotes the selected threshold (amplitude) that is used for tie/ballast discrimination.

Chapter 3: Vibration-based Method for Structural Damage Localization and Quantification

3.1. Introduction

Among different damage detection methods, vibration-based approaches have been extensively used for structural damage localization and quantification by studying the dynamic behavior of the entire system in a global scale. These methods are based on the relationship between the physical properties (i.e., mass and stiffness) and the vibration parameters (i.e., structural frequencies and mode shapes) of the system [34]. In general, damage causes changes in the physical properties of the structural system which affect the vibration characteristics. Therefore, evaluating the vibration parameters of a given system, can be potentially used for damage identification and quantification [34, 35]. Based on this definition, damage detection is classified as an *inverse problem*: The vibration parameters are considered as the inputs and the goal is to find the structure's physical properties in a way that the measured vibration characteristics are achieved. Different approaches can be utilized to solve such an inverse problem [36–38]. Herein, these methods are classified as *iterative* and *deterministic* model updating approaches.

Iterative methods are basically based on error and trial concept [39]. An error function is proposed to minimize the difference between the behavior of the monitored structure and its analytical model (with unknown damage variables). The unknown variables are guessed in each iteration and the error function is evaluated to check the suitability of the guessed variables. Such a problem is a highly ill-posed problem, with an inherently complex solution domain, and a robust search method is required to solve it. Gradient-based search algorithms can be used to solve such problems; however, they might face some uncertainties in converging to the global optimal point because of their dependency on the initial guesses. Derivative-free optimization algorithms (e.g., metaheuristic nature-inspired optimization algorithms [39]) can offer more robust seeking techniques to tackle this problem.

In deterministic approaches, a damage index is developed to identify the location and the severity of the structural damage. In the latter, an explicit expression between the unknown damage severities and damage-sensitive parameters is derived in a way that the damage severity in the element level is returned [40, 41]. In general, deterministic methods are simple to implement and are attractive in terms of high-speed damage quantification. However, they have some shortcomings: Most of the deterministic methods are adapted for simple structures and they cannot be implemented for damage detection in complex systems. Generally, they are classified as ill-posed problems and noisy input data can adversely affect their success in real applications. Moreover, deterministic methods need sensor installation in almost all the structural Degrees of Freedom (DOFs) to return more robust damage detection results.

3.2. Motivation and scope

Damage in structures can be modeled as stiffness reduction in the damaged elements. Such an assumption has been accepted and widely used in different research works [35, 39, 42]. Following this definition of structural damage, in this chapter a new vibration-based damage detection method is proposed aiming at structural damage localization and quantification. Based on the presented brief review of the vibration-based model updating and damage detection methods in section 3.1, some of the main challenges and/or shortcomings of such methods are listed as follows:

(1) An accurate model of the intact structure is needed,

(2) Sensor installation in all the DOFs is required,

(3) To quantify damage, iterative approaches in the optimization framework should be used.

In this section, a new deterministic approach with an iterative self-tuning capability is proposed as an effort to tackle the practical and computational difficulties associated with challenges (2) and (3). Changes in the static deflections (estimated by the modal data) are computed and a simple relationship between the unknown damage severities and damage-sensitive vibration characteristics is derived. Using the proposed method, the baseline model is updated to a transition model named "*Adapted Baseline (AB)*" model. Then, the method is repeated to adjust the estimated damage severities in the AB model in a way that this model converges to a behavior close to the monitored structure's behavior. The method can be used for Finite Element (FE) model updating of all the engineering structures, without any change in the main principles. The method is also generalized for a case in which sparse sensors are used for data acquisition. Using the data of a series of tests carried out on lab-scale and full-scale shear building structures, the performance of the proposed method is assessed. Also, a parametric study is conducted to evaluate the general performance of the supports in the studied full-scale shear-type building.

3.3. The proposed damage detection method

3.3.1. Fundamentals

A structural system with N_e elements and N degrees of freedom (DOFs) is considered. Defining damage as some reduction in the stiffness matrix of the damaged element(s), the global stiffness matrix of the damaged structure, $\mathbf{K}^d$, can be formulated as follows:

$$\mathbf{K}^d = \sum_{e=1}^{N_e}(1-d_e)\mathbf{K}_e^u \ \ , \ 0 \le d_e \le 1.0 \tag{3.1}$$

where, superscripts u and d denote undamaged and damaged states, respectively. $\mathbf{K}_e$ denotes the stiffness matrix of the *e*th element and d_e is the amount of damage in the *e*th element, which is a number between 0 (for the healthy case) and 1 (for the fully damaged case). Eq. (3.1) can be re-written as:

$$\mathbf{K}^d = \mathbf{K}^u - \mathit{\Delta}\mathbf{K} \tag{3.2}$$

in which, $\Delta\mathbf{K}$ is:

$$\Delta\mathbf{K} = \sum_{e=1}^{N_e} d_e \mathbf{K}_e^u \tag{3.3}$$

Based on Hooke's law, if $\mathbf{f}_I$ is applied to all DOFs, the static displacement of the damaged structure, $\mathbf{u}^d$, is calculated as:

$$\mathbf{K}^d \mathbf{u}^d = \mathbf{f}_I \tag{3.4a}$$

or

$$\mathbf{u}^d = \mathbf{G}^d \mathbf{f}_I \tag{3.4b}$$

where, $\mathbf{f}_I$ is defined as the unit static force vector ($\mathbf{f}_I=\{1.0\ 1.0\ \ldots\ 1.0\}^T$) ($\mathbf{f}_I$ has N entries), and $\mathbf{G}^d$ is the flexibility matrix of the damaged structure. Because the flexibility matrix can be calculated by means of the modal data of the first several mode(s), it is more preferred to employ Eq. (3.4b) to estimate the static displacement of the structure using the extracted modal data from dynamic tests. Note that following this strategy, not only can the practical difficulties associated with static tests be tackled, but also the sensitivity of the modal data to structural damage is exploited.

Using the first two terms of the Taylor expansion, $\mathbf{u}^d$ can be computed as below:

$$\mathbf{u}^d \approx \mathbf{u}^u + \sum_{e=1}^{N_m} d_e \left(\frac{\partial \mathbf{u}^d}{\partial d_e}\right)\Bigg|_{d_e=0} \tag{3.5}$$

where, $\mathbf{u}^u$ is the static displacement of the undamaged structure. By differentiating from both sides of Eq. (3.4b) with respect to the damage ratio of the eth element, d_e, Eq. (3.6) is yielded:

$$\frac{\partial \mathbf{u}^d}{\partial d_e} = \frac{\partial \mathbf{G}^d}{\partial d_e}\mathbf{f}_I + \mathbf{G}^d \frac{\partial \mathbf{f}_I}{\partial d_e} \tag{3.6}$$

Because $\mathbf{f}_I$ is not a function of d_e, its differentiation with respect to d_e will be zero:

$$\frac{\partial \mathbf{f}_I}{\partial d_e} = \mathbf{0} \tag{3.7}$$

In the following, $\partial\mathbf{G}^d/\partial d_e$ is calculated. Note that because the flexibility matrix is the inverse of the stiffness matrix, the relationship between the flexibility and stiffness matrices for the damaged structure is released as:

$$\mathbf{G}^d\mathbf{K}^d = \mathbf{I} \tag{3.8}$$

where, **I** is the unity matrix. By differentiating from both sides of Eq. (3.8) with respect to d_e, Eq. (3.9) is released:

$$\frac{\partial \mathbf{G}^d}{\partial d_e}\mathbf{K}^d + \mathbf{G}^d\frac{\partial \mathbf{K}^d}{\partial d_e} = \mathbf{0} \tag{3.9}$$

Considering the damage definition presented in Eq. (3.1), $\partial\mathbf{K}^d/\partial d_e = -\mathbf{K}_e^u$. Therefore, Eq. (3.9) is rewritten as:

$$\frac{\partial \mathbf{G}^d}{\partial d_e} = \mathbf{G}^d\mathbf{K}_e^u\mathbf{G}^d \tag{3.10}$$

By substituting Eq. (3.7) and (3.10) into Eq. (3.6), Eq. (3.11) is yielded:

$$\frac{\partial \mathbf{u}^d}{\partial d_e} = \mathbf{G}^d\mathbf{K}_e^u\mathbf{G}^d\mathbf{f}_I \tag{3.11}$$

Finally, considering Eq. (3.5) and Eq. (3.11), differences between static displacements of the damaged and undamaged structures is achieved as:

$$\mathbf{u}^d - \mathbf{u}^u \approx \sum_{e=1}^{N_e} d_e(\mathbf{G}^u\mathbf{K}_e^u\mathbf{G}^u\mathbf{f}_I) \tag{3.12}$$

This equation can be re-written in matrix format as follows:

$$\mathbf{u}^d - \mathbf{u}^u \approx \mathbf{A}^u.\mathbf{d} \tag{3.13}$$

where,

$$\mathbf{A}^u = [\mathbf{G}^u\mathbf{K}_1^u\mathbf{G}^u\mathbf{f}_I \quad \mathbf{G}^u\mathbf{K}_2^u\mathbf{G}^u\mathbf{f}_I \quad \cdots \quad \mathbf{G}^u\mathbf{K}_{N_e}^u\mathbf{G}^u\mathbf{f}_I] \tag{3.14a}$$

$$\mathbf{d} = \{d_1 \quad d_2 \quad \dots \quad d_{N_e}\}^T \quad ; \quad 0 \le d_i \le 1.0 \quad , \qquad i = 1, 2, \dots, N_e \tag{3.14b}$$

The vector **d** returns damage severity of the elements and it can be calculated using least-square method as follows:

$$\mathbf{d} = ((\mathbf{A}^u)^T.\mathbf{A}^u).(\mathbf{A}^u)^T.\left(\mathbf{u}^d - \mathbf{u}^u\right) \tag{3.15}$$

where, $\mathbf{u}^d$ and $\mathbf{u}^u$ are computed using the modal data of the first p mode(s) as:

$$\mathbf{u}^d = \left(\mathbf{\Phi}_p^d\right).\left(\mathbf{\Omega}_p^d\right)^{-1}.\left(\mathbf{\Phi}_p^d\right)^T.\mathbf{f}_I \tag{3.16a}$$

$$\mathbf{u}^{u} = \left(\boldsymbol{\Phi}_{p}^{u}\right).\left(\boldsymbol{\Omega}_{p}^{u}\right)^{-1}.\left(\boldsymbol{\Phi}_{p}^{u}\right)^{T}.\mathbf{f}_{I} \tag{3.16b}$$

in which, $\boldsymbol{\Phi}_p$ and $\boldsymbol{\Omega}_p$ are the matrix containing the first p mode shape vector(s) and a diagonal matrix of the first p eigenvalue(s) (i.e., the square of the first p natural frequencies), respectively. Using Eq. (3.15), damages in the monitored system can be estimated. In the next section, the details of the proposed method are presented.

3.3.2. The proposed method

In section 3.3.1, the fundamentals and formulation of the proposed method were derived. In the present section, different steps of the method are explained. The flowchart of the proposed method is shown in Figure 3.1. First, the structure is tested in the field and the acceleration time histories under an external ambient or synthetically generated excitation are recorded by accelerometers. Then, the modal data (i.e., frequencies and mode shape vectors) of the monitored structure is extracted. In most of the SHM programs, the number of the sensors are less than the ideal number of the structural DOFs. But the proposed method requires a set of full-size mode shape vectors. If sparse sensors are used for data acquisition, the full-size mode shapes can be estimated using mode shape expansion approaches. In this thesis, the Perturbed Force-based Mode Shape Expansion (PF-MSE) technique [43] is used for this purpose. PF-MSE technique is explained in section 3.3.3. Utilizing the first p modes' data (i.e., the frequencies and full-size mode shape vectors), the proposed method is implemented by developing an analytical (or baseline) model of the monitored structure. This model is based on the intact structure's specifications, with unknown variables in all the elements representing unknown damage parameters (see Eq. (3.1)). Employing Eq. (3.15) the baseline model is updated to a transition *Adapted baseline* (AB) model. In the next step, the AB model is considered as a *new* baseline model and the proposed deterministic approach is repeated to tune damage severities. The updating procedure is stopped in the ith round of updating if the magnitude of tuning parameters for most the elements is close to zero.

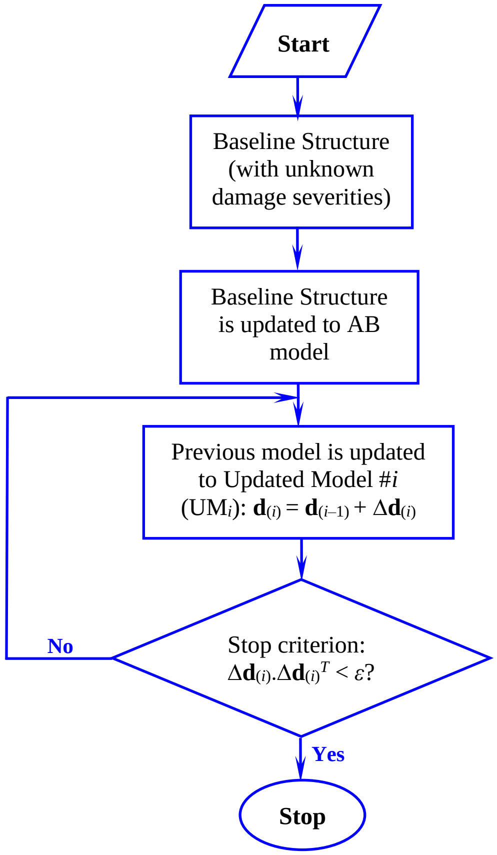

Figure 3.1: The flowchart of the proposed method. $\mathbf{d}_{(i)}$ and $\Delta\mathbf{d}_{(i)}$ denote the total and tuning damage severity vectors in the *i*th iteration, respectively.

3.3.3. Mode shape expansion to compensate the effects of the sparse sensor measurements

In the actual monitoring programs, it is difficult to attach sensors to all the effective DOFs highlighted in the FE model. Therefore, the number of the sensors attached to the system (N_s) is almost always less that the total number of the effective DOFs (N). This means that the extracted mode shape vectors will be in the order of N_s. However, in most of the applications (e.g., structural model updating and damage detection), full size mode shape vectors are required. To tackle this issue and estimate the full-size mode shape vectors, Mode Shape Expansion (MSE) techniques can be used. In this thesis, an MSE technique is employed to make full size mode shape vectors required in computing the static deflections of the structure using Eqs. 3.16(a) and 3.16(b). In the following, the MSE technique is briefly introduced.

The dynamic equilibrium equation for a structural system with *N* DOFs is written as follows:

$$\left(\mathbf{K}-\omega_i^2\mathbf{M}\right)\boldsymbol{\varphi}_i=\mathbf{0} \tag{3.17}$$

where, **K** and **M** are the global stiffness and mass matrices, respectively, and ω_i and $\boldsymbol{\varphi}_i$ are the *i*th natural frequency and the associated mode shape vector, respectively. The full set of analytical DOFs are divided into two sets, the measured DOFs at the test points (as *master* DOFs, denoted by superscript "*m*") and the remaining unmeasured DOFs (as *slave* DOFs, denoted by superscript "*s*"). Eq. (3.17) is rewritten in the partitioned format as follows:

$$\begin{bmatrix}\mathbf{K}^{mm} & \mathbf{K}^{ms}\\ \mathbf{K}^{sm} & \mathbf{K}^{ss}\end{bmatrix}\begin{Bmatrix}\boldsymbol{\varphi}_i^m\\ \boldsymbol{\varphi}_i^s\end{Bmatrix}-\omega_i^2\begin{bmatrix}\mathbf{M}^{mm} & \mathbf{M}^{ms}\\ \mathbf{M}^{sm} & \mathbf{M}^{ss}\end{bmatrix}\begin{Bmatrix}\boldsymbol{\varphi}_i^m\\ \boldsymbol{\varphi}_i^s\end{Bmatrix}=\begin{Bmatrix}\mathbf{0}\\ \mathbf{0}\end{Bmatrix} \tag{3.18}$$

From the second row of Eq. (3.18), the unmeasured part of the *i*th mode shape vector can be obtained:

$$\boldsymbol{\varphi}_i^s=-\left[\mathbf{K}^{ss}-\omega_i^2\mathbf{M}^{ss}\right]^{-1}\left[\mathbf{K}^{sm}-\omega_i^2\mathbf{M}^{sm}\right]\boldsymbol{\varphi}_i^m \tag{3.19}$$

The *i*th expanded full-size mode shape vector, is assembled using the sub-mode shape vectors related to the measured part, $\boldsymbol{\varphi}_i^m$, and unmeasured part, $\boldsymbol{\varphi}_i^s$, as follows:

$$\boldsymbol{\varphi}_i=\begin{Bmatrix}\boldsymbol{\varphi}_i^m\\ \boldsymbol{\varphi}_i^s\end{Bmatrix}=\mathbf{T}\boldsymbol{\varphi}_i^m \tag{3.20}$$

where, **T** is the transformation matrix between the incomplete and full-size models. Depending on the model expansion method, different representations of **T** have been developed in the literature. One of the simplest approaches is *static* or Guyan model expansion (mainly known as Gyuan model *reduction*[2] method) [43,

---

[2] Note that using the same transformation matrix, the mass and stiffness matrices of the full-size system can be reduced to the order of the measured (master) DOFs. For example, in Guyan method, the reduced mass and stiffness matrices are computed as follows:

$$(\mathbf{M}_{reduced})_{m\times m}=\mathbf{T}_{Guyan}^T\mathbf{M}\mathbf{T}_{Guyan} \quad , \quad (\mathbf{K}_{reduced})_{m\times m}=\mathbf{T}_{Guyan}^T\mathbf{K}\mathbf{T}_{Guyan}$$

Model reduction concept is of interest if iterative optimization-based model updating is employed for damage detection (for example, see [45, 46]). In such cases, the modal data of the monitored structure is extracted in the tested points. Subsequently, the change in the physical properties (e.g., change in the stiffness if Eq. (3.1) is employed to

44], which is based on static stiffness by neglecting the inertial forces at the unmeasured DOFs. The transformation matrix for this technique is given by [43]:

$$\mathbf{T}_{Guyan} = \begin{bmatrix} \mathbf{I} \\ -(\mathbf{K}^{ss})^{-1}\mathbf{K}^{sm} \end{bmatrix} \tag{3.21}$$

There are also other model reduction approaches that consider the inertial terms and are known as *dynamic* methods [47–51]. Although the transformation matrices of the dynamic model expansion methods have extra terms comparing with Eq. (3.21), the entries of these matrices are mainly based on the physical properties or modal data of the reference structure. In the following, Eq. (3.21) is inspected in detail to highlight its shortcomings in terms of returning accurate expanded mode shape vectors.

Based on Eq. (3.21), the transformation matrix requires the stiffness matrix of the model. However, in the damage detection methods (developed by defining damage as stiffness reduction (i.e., Eq. (3.1)), there is no information about the stiffness of the monitored structure. Therefore, the stiffness of a reference model (basically, intact or undamaged model) is used to form Eq. (3.21), which can be a source of the error in the expanded mode shape vectors. On the other hand, the discrepancy between the reference model and the actual tested structure (potentially the damaged structure) is not considered in the static or conventional dynamic MSE techniques. This also causes considerable errors in the estimated mode shape vectors for the monitored structure. To tackle these issues and estimate unmeasured entries of the mode shape vectors with high accuracy, Chen [43] proposed a Perturbed Force-based Mode Shape Expansion (PF-MSE) technique to formulate the transformation matrix by considering the unknown discrepancy between the physical properties of the monitored structure and the reference model. Note that such an MSE technique is well-suited to extract the full-size mode shape vectors of the tested structures in the applications like structural damage detection, in which the physical properties of the tested structures are partially unknown.

---

define damage) are guessed in different iterations and used to construct the full-size mass and stiffness matrices of the analytical model. These matrices are then condensed using the model reduction approaches and modal data of the condensed analytical model is extracted and compared with the test modal data.

In this thesis, the PF-MSE is employed to extract the full-size model shape vectors which are subsequently fed into the proposed method as the input data. In the PF-MSE technique, the discrepancy in the mass and stiffness matrices are considered as below:

$$\mathbf{M}_t = \mathbf{M} + \Delta\mathbf{M} \tag{3.22a}$$

$$\mathbf{K}_t = \mathbf{K} + \Delta\mathbf{K} \tag{3.22b}$$

where, $\mathbf{M}_t$ and $\mathbf{K}_t$ denote the mass and stiffness matrices of an analytical model for the tested structure, respectively, $\mathbf{M}$ and $\mathbf{K}$ are the mass and stiffness matrices of the reference model, respectively, and $\Delta\mathbf{M}$ and $\Delta\mathbf{K}$ are the unknown perturbation in the mass and stiffness matrices between the reference model and the tested structure, respectively. In the damage detection applications, the perturbation matrices can represent the structural damage, and the reference model is considered as the intact structure. The PF-MSE technique is based on expressing the mode shape vectors as a linear combination of the independent analytical eigenvectors. Then, the incomplete set of the measured DOFs are scaled with an Adjusting Factor (AF) to make the measured mode shapes close to the corresponding part of the reference model's mode shape vectors. Finally, the full-size mode shape vectors of the tested structure are computed by Eq. (3.20), utilizing a mode-wise transformation matrix as follows [43]:

$$\mathbf{T}_i = \begin{bmatrix} \mathbf{I} \\ \displaystyle\sum_{j=1}^{n} \frac{(\boldsymbol{\varphi}_r)_j^s (\boldsymbol{\varphi}_r)_j^T \mathbf{B}_i^+}{\left((\omega_t)_i^2 - (\omega_r)_j^2\right)} \end{bmatrix} \quad , \quad \mathbf{B}_i = \sum_{j=1}^{n} \frac{(\boldsymbol{\varphi}_r)_j^m (\boldsymbol{\varphi}_r)_j^T}{\left((\omega_t)_i^2 - (\omega_r)_j^2\right)} \tag{3.23}$$

where, subscripts *i* and *j* show the *i*th and *j*th mode, respectively, *t* and *r* denote the information related to the tested structure and reference model, respectively, *n* is the number of the available modes (which is equal to *N* in an ideal case that all the structural modes are extracted from the modal analysis). Also, it is recalled that superscripts *m* and *s* denote DOFs associated with the measured (master) and unmeasured (slave) DOFs, respectively, which are determined based on the measurement configuration developed for acquiring data from the tested structure. Moreover, **B** is the sensitivity coefficient matrix which brings the effects of AF and the perturbation force into the MSE technique, and "+" is the Moore-Penrose pseudoinverse operator. Note that in the presence of noisy modal data, **B** belongs to a highly ill-posed domain and $\mathbf{B}^{+}$ is computed by Tikhonov regularization [43].

3.4. Experimental validations

3.4.1. Lab-scale five story shear building structure on a shake table

In this section the proposed method is utilized for damage detection and quantification in a five-story shear building structure tested on a shaking table (see Figure 3.2). This structure has been previously studied for damage identification and localization [52]. In this thesis, the raw data of the tests was analyzed to extract the modal data and implement the proposed method.

The physical properties of the frame are as follows: mass m=16.09 kg, bending stiffness EI=20 Nm^2, story length h=34.3 cm, and damping c=3.27 Ns/m. In addition, the modulus of elasticity, the Poisson's ratio, and the mass density for the steel used in this building are ρ=7850 $\mathrm{kg/m}^3$, v=0.28, and E=200 GPa, respectively. The damage pattern was introduced by 10% reduction in the stiffness of the of the first story. The columns' cross sections in the intact and damaged states are shown in Figure 3.3.

A white noise broadband excitation was applied to the structure by a shake table for 10 minutes, and five accelerometers were attached to the building (one accelerometer to each story) to record the structural time history responses with a sampling frequency of 20 Hz [52]. Both the intact and damaged structures were tested eight times to investigate the effects of the measurement uncertainties on the modal data and subsequently, on the performance of the proposed method. Figure 3.4 shows the time history responses recorded by the sensors for a typical test. Data-drive stochastic subspace identification method [53] is employed for modal parameter identification. Figure 3.5 shows the first three mode shapes extracted in the healthy and damaged states. Although small discrepancy between the mode shapes of the intact and damaged structures is observed, no detailed decision can be made on the health of the monitored structure only by inspecting the general trend of the mode shapes. The first three modes' frequencies and the associated MAC values (as an index representing the amount of correlation between the mode shape vectors in the intact and damaged cases) are presented in Table 3.1 for one typical test. This table reveals that by occurring damage in the structure, the frequencies decrease in comparison with the pristine state. However, based on the summarized MAC values in Table 3.1, it is difficult to judge the health of the monitored structure by evaluating the amount of correlation between the mode shapes vectors in two states.

Figure 3.2: Experimental setup of the five-story shear building structure on the shake table.

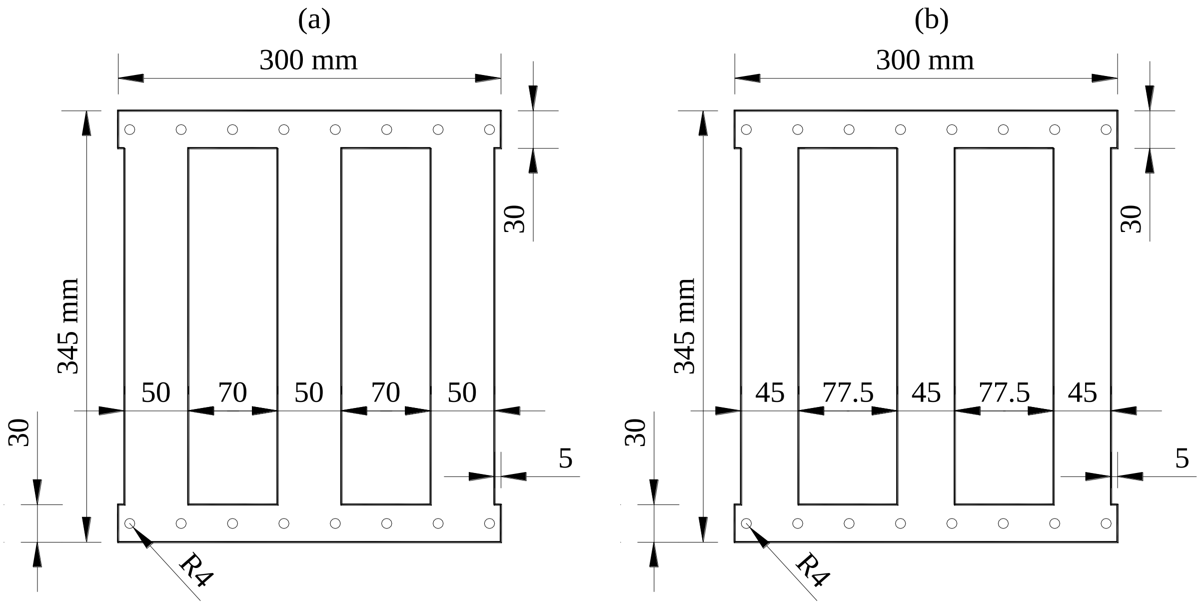

Figure 3.3: Column shapes for the lab-scale five-story building structure: (a) undamaged and (b) damaged states (units: mm).

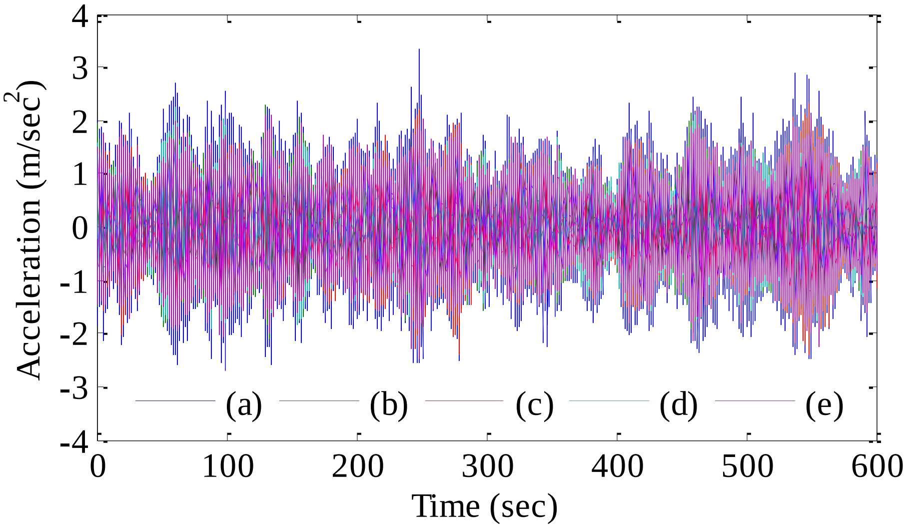

Figure 3.4: Recorded time history responses by the sensors for a typical test: (a) first floor, (b) second floor, (c) third floor, (d) fourth floor, and (e) fifth floor responses.

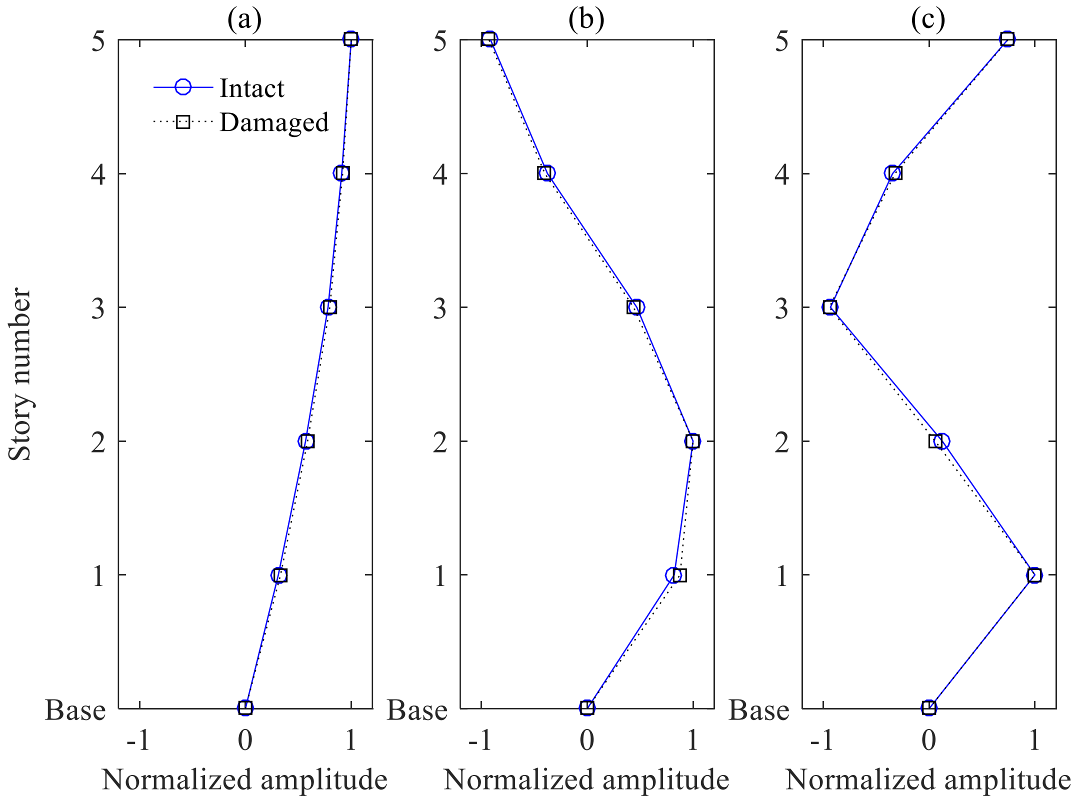

Figure 3.5: Mode shapes of the lab-scale five-story shear frame in the intact and damaged states: (a) first mode, (b) second mode, and (c) third mode.

Table 3.1: The modal frequencies and MAC values for different states of the lab-scale five-story shear frame.

Parameter	**State**	**The first mode**	**The second mode**	**The third mode**
Frequency (Hz)	Intact	1.24	3.70	5.91
	Damaged	1.21	3.63	5.84
MAC [*]	Damaged	0.9998	0.9987	0.9980

[*] MAC is the correlation between mode shape vectors. The structure is labeled as "undamaged" if MAC = 1.0.

The proposed method is employed to identify damage location and severity in the monitored structure using the first two and three modes' data (i.e., p=2 and 3). First, an analytical model of the monitored structure (with unknown damage parameters) was developed as the baseline model and its suitability was verified using the modal data of the intact structure tested immediately after assembling on the shake table[3]. For this purpose, the modal data of the tested structure in undamaged state is utilized for model updating. The time histories recorded by all the attached sensors are analyzed in the present study ($N_s = N$). Therefore, the extracted mode shape vectors are in full size and no MSE is required. Note that in all the studies, the stop criterion (see Figure 3.1) is defined as ε=1×10^{-10}. The obtained results are shown in Figures 3.6 and 3.7 for p=2 and p=3 cases, respectively. In these figures, the results of the first updating stage (in which the AB model is achieved) as well as the final results are shown for eight independent tests. In some of the tests, small damage severities have been reported for the first story, which are justifiable considering the effects of the measurement noise. However, the average / standard deviation of the reported damage severities for the first story in eight independent tests are 0.2% / 0.47 and 0.19% / 0.47 for p=2 and p=3, respectively. Therefore, regardless the number of the utilized modes to update the model, damage in all the stories are equal (or very close) to zero, and the suitability of the developed analytical model of the constructed structure is confirmed.

In the following, the proposed method is used for damage identification and quantification in the damaged structure. Modal data of the first two and three modes (i.e., p=2 and 3) are employed to update the baseline model. In this study, the responses of a full set of sensors are used for extracting the modal data. The stop criterion is defined as ε=1×10^{-10}. The obtained results for all eight independent tests using the first two and three modes' data are shown in Figures 3.8 and 3.9, respectively. Based on the results, the method can correctly identify and quantify the modeled damage (i.e., 10% damage in the first story), with no false-positive or -negative alarms. The mean / standard deviation of the reported damage severities for the first story are 11.79% / 1.03 and 10.92% / 1.63, for p=2 and p=3, respectively. Therefore, not only is the acceptable accuracy of the method revealed, but also its precision (i.e., repeatability) is confirmed. In p=2, the first updating stage (i.e., the damage detection results which are used to form the transition AB

---

[3] In actual SHM programs, such a model is numerically developed using as-built maps, but a kind of verification is needed to match the behavior of the numerical model with the actual behavior of the undamaged structure. Leveraging "digital twins" concept, more realistic baseline of the structure can be developed [54]. Also, hybrid numerical/experimental approaches can also be employed to develop suitable analytical models if the as-built maps are not available [55].

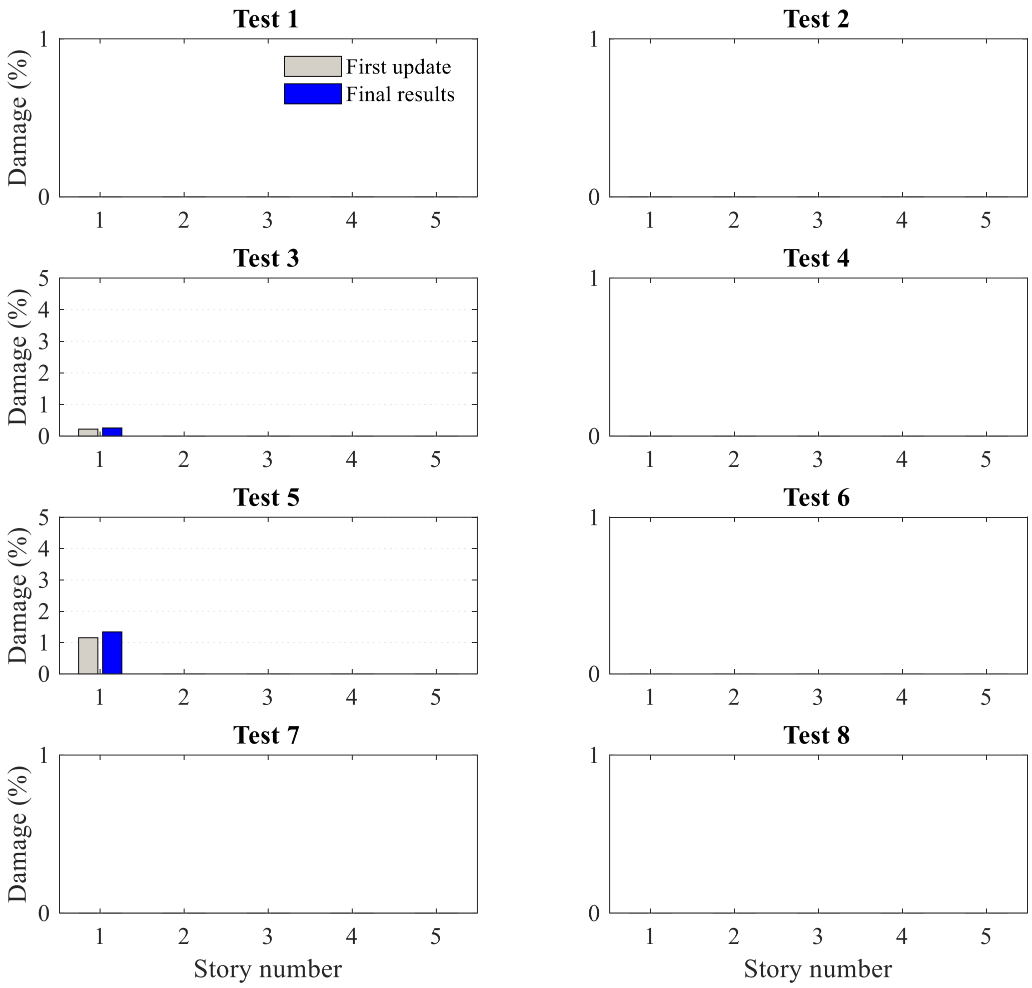

Figure 3.6: Damage detection results for the lab-scale five-story building structure in undamaged case: *p*=2. The results are used for calibrating the analytical model of the intact structure.

model) performs well, and the subsequent updating stages have small tuning effects on the reported damage parameters for the AB model. In *p*=3, however, the advantage of the further updating can be clearly observed. Inspecting the damage severities denoted as "First update" in Figure 3.9, there are overestimations in the damage severities reported for story #1 (for example, see Test #3 in Figure 3.9). Moreover, some small damage severities have been reported in the healthy stories (for example, see Test #1 in Figure 3.9). In the next updating stages, however, these overestimations and false-positive results are effectively tuned, and more accurate results are reported as the final damage detection results.

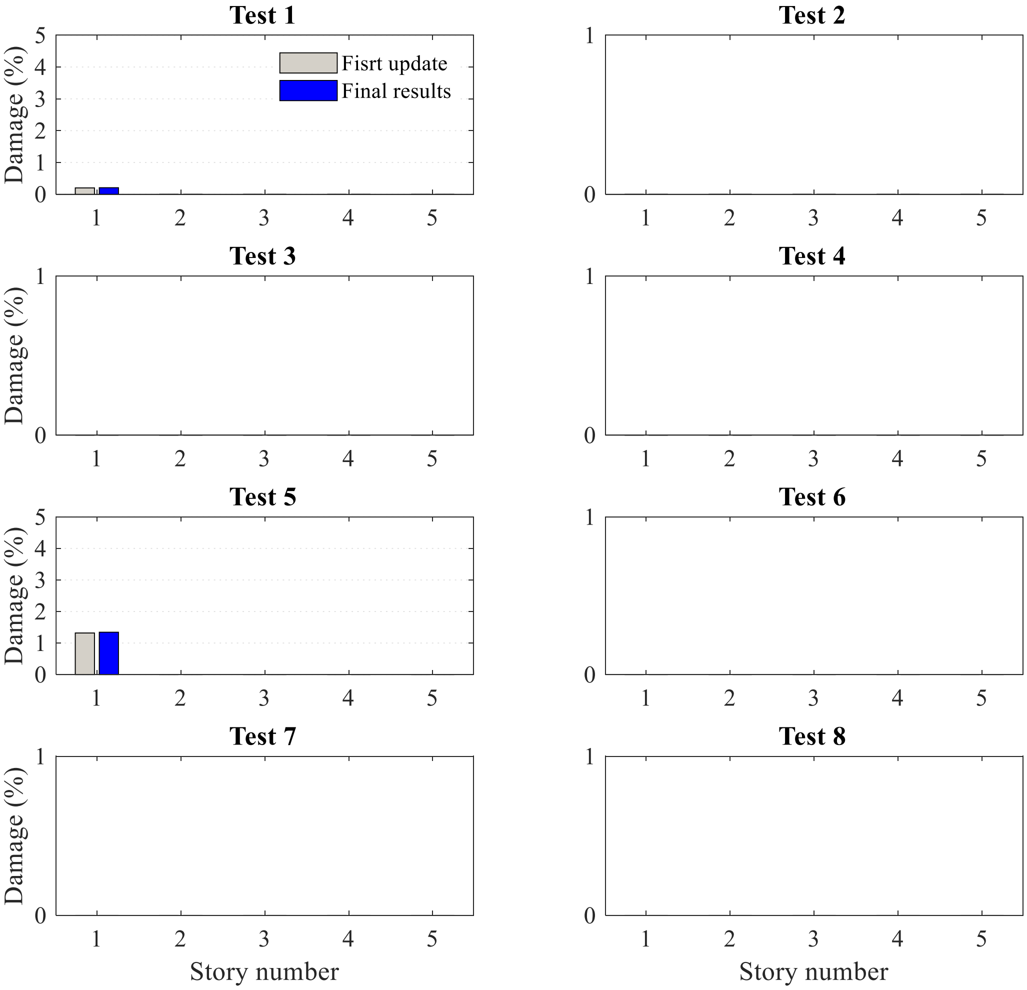

Figure 3.7: Damage detection results for the lab-scale five-story building structure in undamaged case: *p*=3. The results are used for calibrating the analytical model of the intact structure.

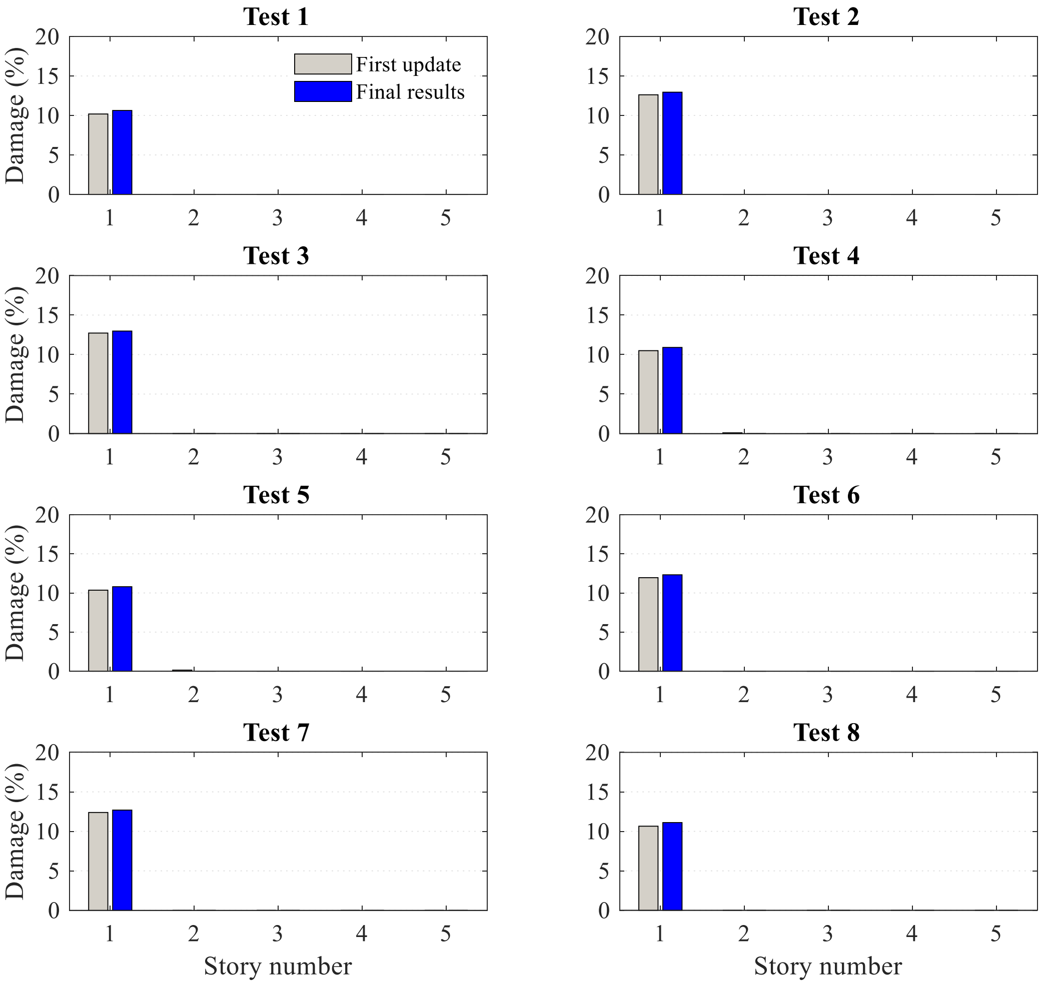

Figure 3.8: Damage detection results for the lab-scale five-story building structure in the damaged case: p=2 and N_s=5.

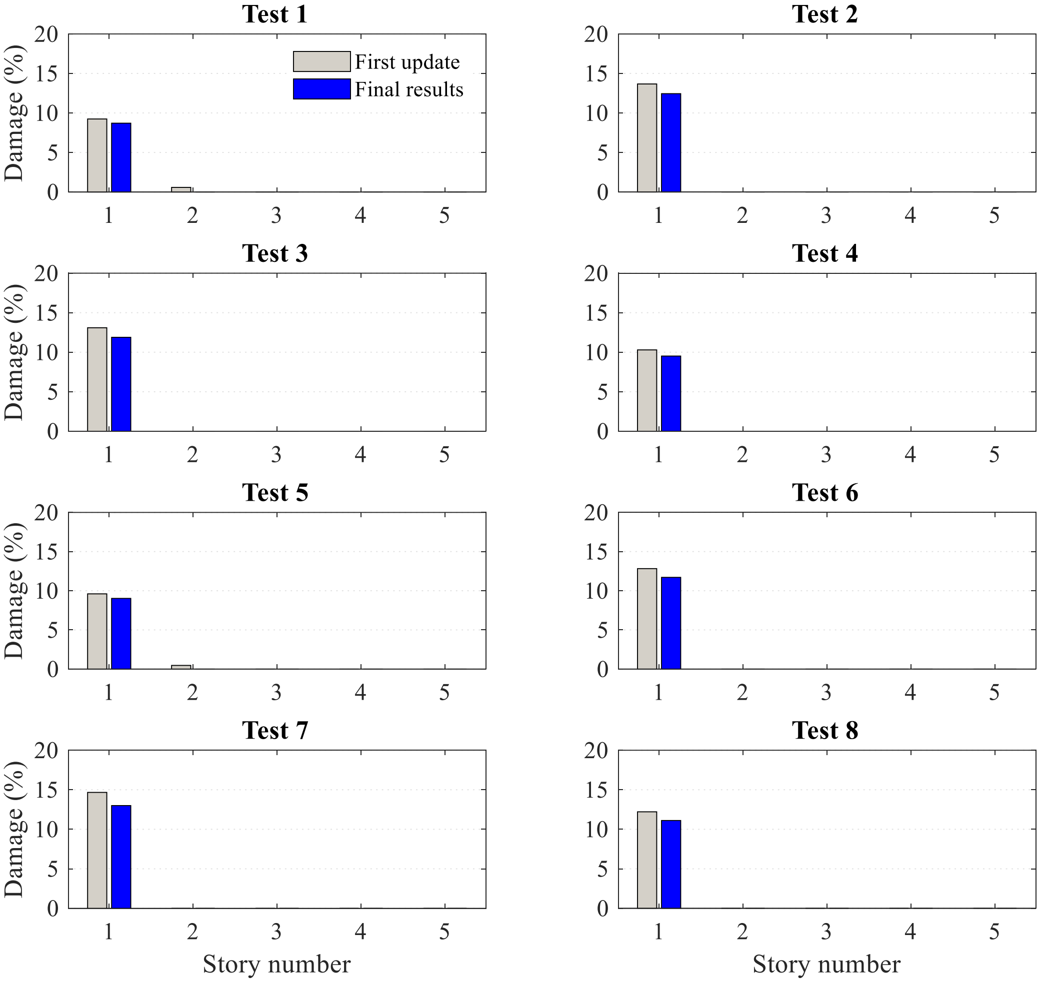

Figure 3.9: Damage detection results for the lab-scale five-story building structure in the damaged case: p=3 and N_s=5.

The performance of the proposed method was investigated using the data of a full set of sensors (i.e., $N = N_s = 5$). In the following, the robustness of the proposed method is evaluated for the cases in which a limited number of sensors are used for data acquisition. Table 3.2 summarizes the details of the sensor installation configurations as well as the number of the available modes for damage detection. In Configs. 1–3, the method is performed using the first two and three modes' data (i.e., p=2, 3); however, Configs. 4–9 concentrated on damage detection using only the first two modes' data (i.e., p=2). Each case is solved eight times (based on the experimental data of eight independent tests), and the mean and one standard deviation of the obtained results are reported as the damage detection results. Figures 3.10 to 3.12 show the obtained results for Configs. 1 to 3, respectively, and the obtained results for the remaining configurations are shown in Figure 3.13. The results emphasize the robust and viable performance of the proposed method for damage detection using sparse sensor measurements even though only 40% of the structural DOFs are equipped with the sensors. Moreover, the results reveal the effectiveness of the proposed iterative updating algorithm in terms of increasing the accuracy of the detected damages in the first updating stage. Note that the AB model, as the transition model, returns acceptable results if the first two or three modes' data are employed; however, the accuracy of the estimated damage features considerably increases using the subsequent updating stages.

Table 3.2: Details of the studied cases to evaluate the performance of the proposed method for damage detection in the lab-scale five-story building structure using sparse sensor measurements

Configuration #	Sensor locations (story number)	Number of the available modes (p)
Config. 1	1, 3, 5	2, 3
Config. 2	1, 3, 4	
Config. 3	1, 2	
Config. 4	4, 5	2
Config. 5	2, 5	
Config. 6	3, 4	
Config. 7	1, 4, 5	
Config. 8	2, 3, 5	
Config. 9	2, 4, 5	

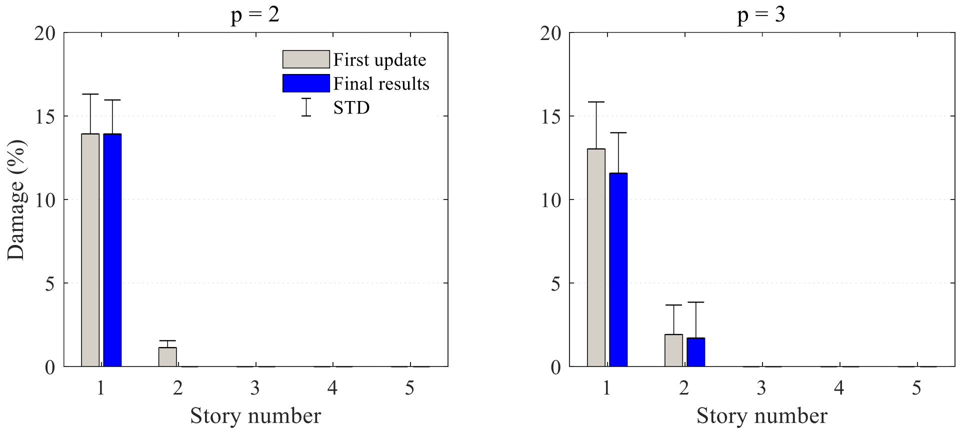

Figure 3.10: The mean and one standard deviation of the obtained damage detection results for lab-scale five-story building structure in the damaged case: sensor configuration #1 – sensors were attached to the 1st, 3rd, and 5th floors.

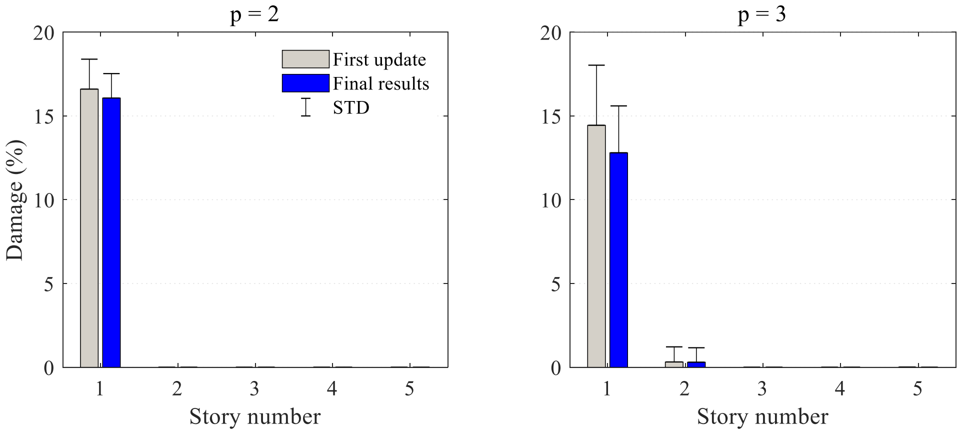

Figure 3.11: The mean and one standard deviation of the obtained damage detection results for lab-scale five-story building structure in the damaged case: sensor configuration #2 – sensors were attached to the 1st, 3rd, and 4th floors.

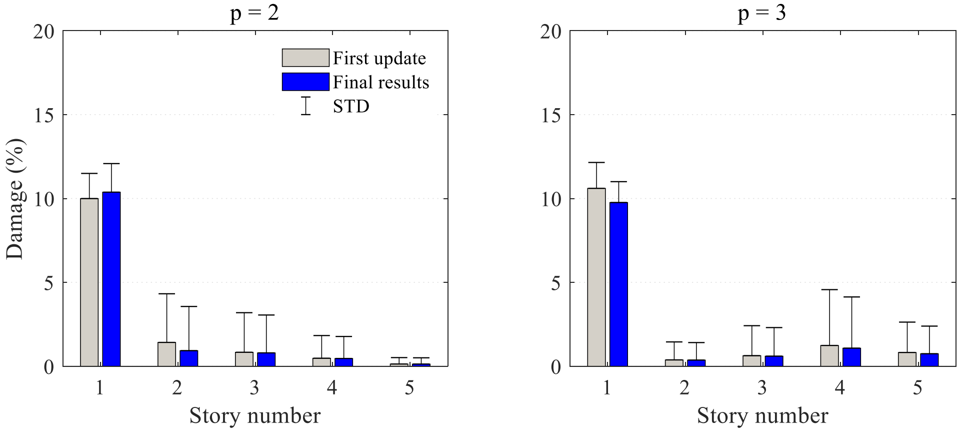

Figure 3.12: The mean and one standard deviation of the obtained damage detection results for lab-scale five-story building structure in the damaged case: sensor configuration #3 – sensors were attached to the 1st and 2nd floors.

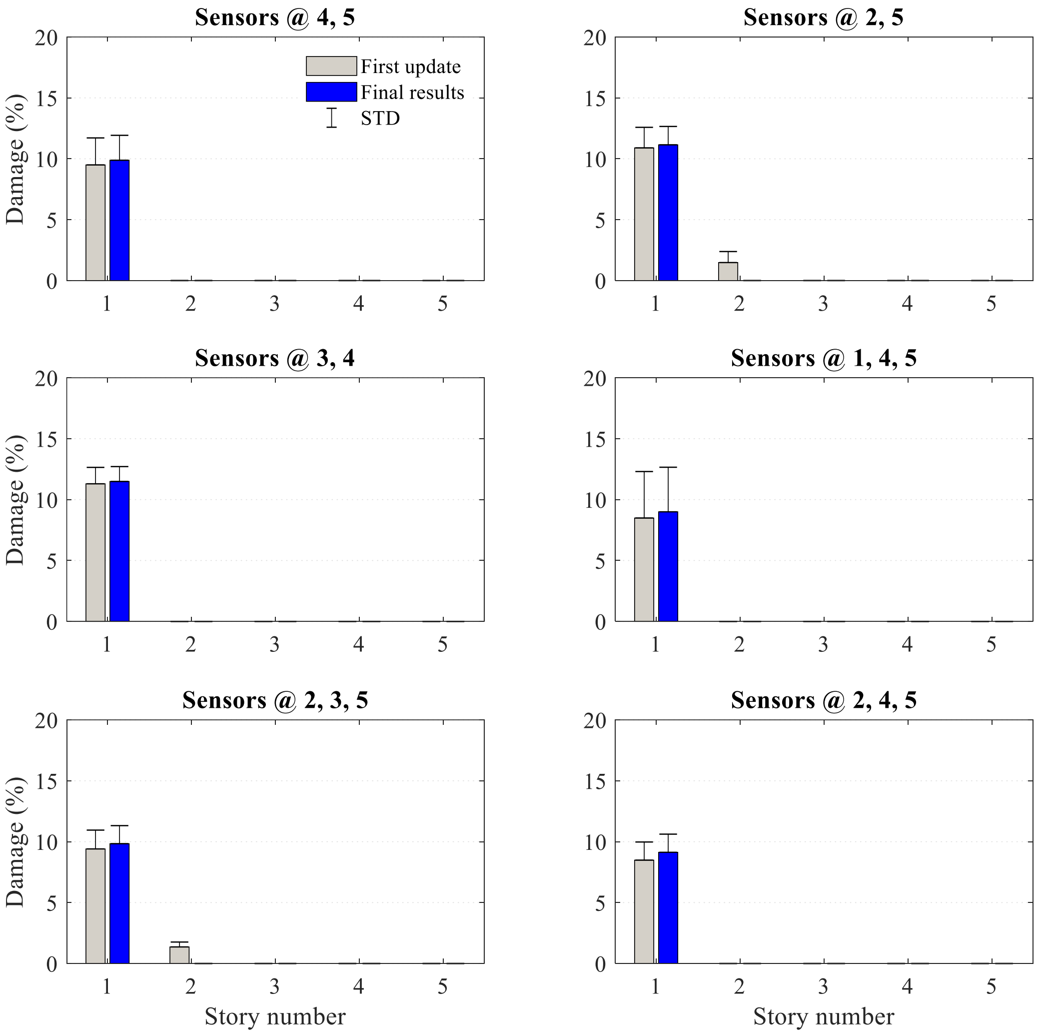

Figure 3.13: The mean and one standard deviation of the obtained damage detection results for lab-scale five-story building structure in the damaged case (*p*=2): sensor configurations 4–9.The number of the stories equipped with sensors has been indicated as the title of each figure.

3.4.2. Full-scale five-story shear building structure

3.4.2.1. The test structure and numerical modelling

The test structure is a five-story building structure as shown in Figure 3.14, named UNISON modal-test tower, and it has been constructed at UNISON Corporation, Cheonan, Korea, to evaluate the effectiveness of the approaches devoted to structural vibration control and damage detection [56]. In this thesis, the raw data of the tests was analyzed to extract the modal data and implement the proposed method.

This building is a steel frame structure with a total height of 30.0 m and slab size of 6.0 m × 6.0 m. Details of the columns' and beams' cross sections are shown in Figure 3.15. A concrete slab with 15 cm thickness covers the floor beams. Each floor is kept by four H-shape steel columns and the length, cross section, and moment of inertia for each column are 6.0 m, 1.78×10^{-2} m^2, and 9.95×10^{-5} m^4, respectively (see Figures 3.14 and 3.15). The fifth story has been covered by a steel container box with 2.0 cm thickness to protect facilities such as an exciter (which is used to produce ambient vibration) and a computer system (used to save the recorded structural responses). The mass density, modulus of elasticity, and Poisson's ratio for floor beams, columns and container box are equal to ρ=7850 kg/m^3, E=200 GPa, and ν=0.3, respectively.

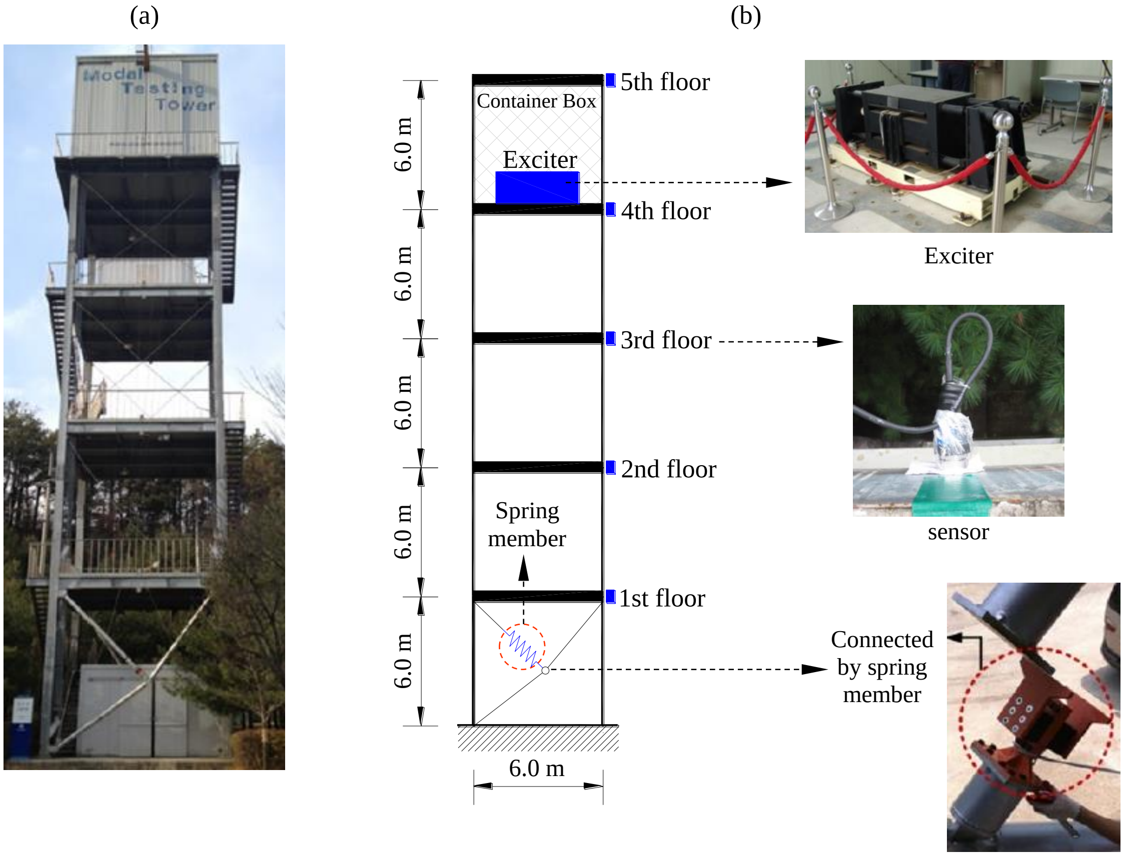

Figure 3.14: (a) UNISON test tower and (b) details of the test structure and measurement setup.

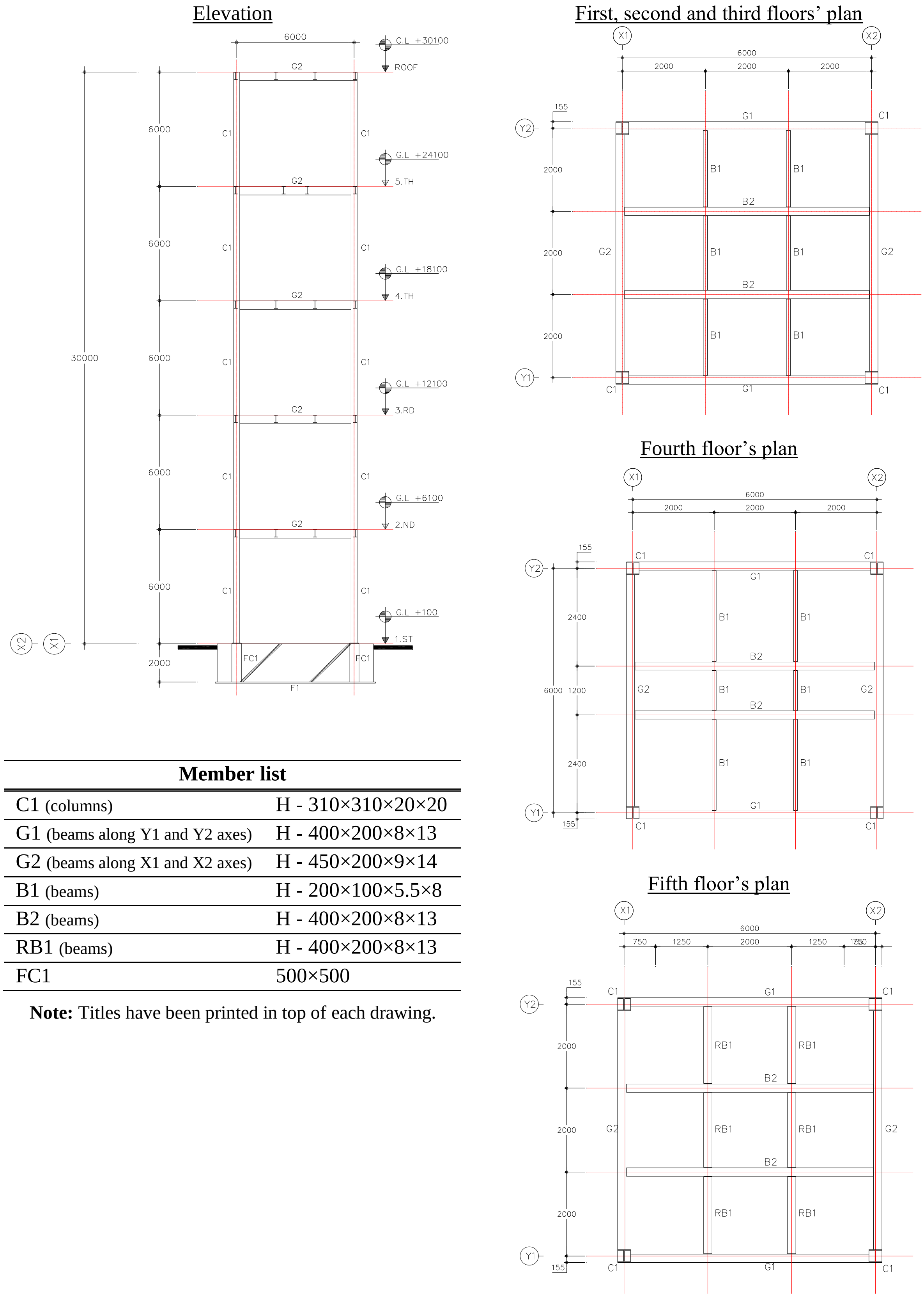

Member list	
C1 (columns)	H - 310×310×20×20
G1 (beams along Y1 and Y2 axes)	H - 400×200×8×13
G2 (beams along X1 and X2 axes)	H - 450×200×9×14
B1 (beams)	H - 200×100×5.5×8
B2 (beams)	H - 400×200×8×13
RB1 (beams)	H - 400×200×8×13
FC1	500×500

Note: Titles have been printed in top of each drawing.

Figure 3.15: Details of the columns' and beams' cross sections for the UNISON tower (units: mm).

The material properties of the floor slabs are as ρ=2300 kg/m^3, E=30 GPa, and v=0.18. The mass of the first, second, and third stories are equal to 19.7 ton. The fourth and fifth stories' masses are equal to 22.352 ton (including the mass of the exciter and other equipment in the fourth story) and 19.775 ton, respectively. With this condition, the structure is considered as an irregular structure in terms of the mass distribution. Because of such irregular distribution of the masses, the behavior of the structure should be evaluated to determine if it is unidirectional. Considering the irregular mass distribution in the height, the rotational behavior of the system should be inspected at level of the upper floors. Thus, based on the behavior of the system in the fourth-floor level, a general conclusion can be made on the entire structure's behavior. For this purpose, the captured video with a surveillance camera installed at the roof level of the fifth story —watching down to the story's floor (i.e., the fourth floor)— is analyzed to find the inter-story displacements. The footage was in low quality, with no tangible information on the camera specifications. Loading and analyzing the video in MATLAB revealed that the footage had been made by a frame rate of 56 FPS. In the analyses, only a segment with a duration of 20 sec was used to track a couple of robust features in the Region of Interest (ROI). Figure 3.16(a) shows a typical frame of the captured footage, including the two robust features automatically selected by SURF algorithm. The points were tracked frame-by-frame using KLT[4] method and the relative displacements (i.e., drifts) of the points in x-y[5] pixel-plane were plotted to check the vibration orientation of the floor during a typical excitation (see Figure 3.16(b)). Based on the results, it is concluded that the structure at the level of the fourth floor is mainly oscillated in the x direction and this emphasizes the unidirectional behavior of this floor. Note that x-y pixel-domain drifts also reveal some tendency of the floor (which is a *rigid* steel-concrete composite floor) to rotate with respect to the z axis (the axis along the structure's height); however, the main trend of oscillation is in the x direction. Therefore, in the present study, the behavior of structure is assumed as a *unidirectional* behavior.

---

[4] KLT tracker was introduced in Chapter 2.

[5] In general, such a plot is known as "Lissajous curve." Considering the control theory of the LTI systems, this plot can be used to evaluate the system's behavior with respect to a reference system.

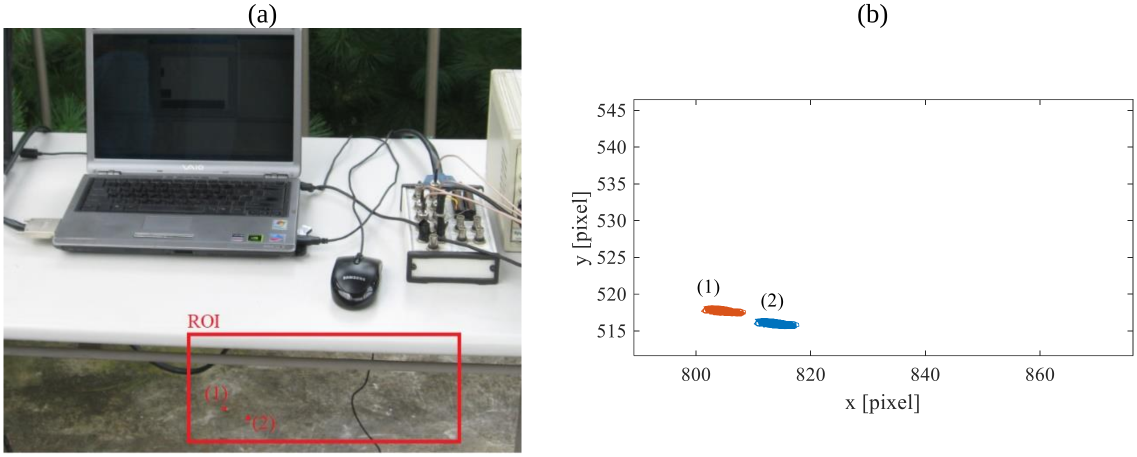

Figure 3.16: (a) A typical frame of the footage captured by a surveillance camera attached to the fifth story's roof. The ROI and the two tracked robust features are shown in this figure. (b) The pixel-domain relative-displacements of the tracked points.

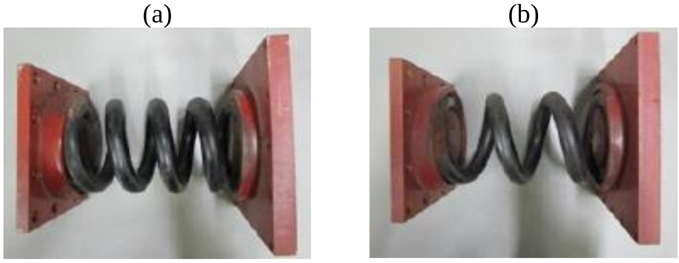

Figure 3.17: Spring members utilized in fabricating the (a) intact and (b) damaged structures.

At the first story of the building, there was a spring member connecting the brace element to the first floor (see Figure 3.14(b)), and damage was introduced by changing the stiffness of this spring member. Two spring members with different stiffness were used, as shown in Figure 3.17. To estimate the actual stiffness of the spring members considering manufacturing errors, an experimental test was conducted by means of a universal test machine (UTM) even though their stiffness has been printed on them [56]. The output of this experiment was plotted as a force-displacement curve of the spring member. If the curve is fitted by a line, the slope of this line will reflect the stiffness of the spring member. The estimated stiffness for the spring members shown in Figures 3.17(a) and 3.17(b) was 1.485 kN/mm and 0.696 kN/mm, respectively. The stiffest spring member was utilized to fabricate the intact structure, and the other spring member was used to build the damaged structure [56].

Because the purpose of this study is to quantify the damage occurred in each story, it is essential to estimate the stiffness of the stories in each case as a forward problem, which will be used to verify the accuracy of the obtained damage detection results. To do so, a numerical model of the intact and damaged structure was simulated in the workspace of ABAQUS [57], a commercial finite element software. Shell elements were used to model the floor slabs. Moreover, the columns and beams were modeled by beam elements while the brace member was made by truss element. Then, the static displacements of each story under a known external load F at the level of each story were extracted as the results of the static analysis in ABAQUS. Finally, the stiffness of the ith story, K_i, was calculated using the Hook's law as follows:

$$K_i = \frac{\sum_{j=i}^{5} F_j}{d_i - d_{i-1}} \ , \ \ i = 1, 2, 3, 4, 5 \ ; \ \ d_0 = 0 \tag{3.24}$$

where, F_j and d_i are the static force applied to the jth story and the static displacement of the ith story, respectively. Figure 3.18 shows the static deflections of the FE model of the UNISON tower in the intact and damaged cases, modeled in ABAQUS. Assuming F_j = 2000 N, and using Figure 3.18 and Eq. (3.24), the estimated stiffness for the first story in the intact and damaged cases are 25.9 kN/m and 16.69 kN/mm, respectively. By comparing the stiffness of the first story in the intact and damaged case, the damage pattern is summarized as 35.56% damage at the first story.

Moreover, the stiffness of the second, third, fourth, and fifth stories are equal to 4.23 kN/mm, 4.13 kN/mm, 3.98 kN/mm, and 3.68 kN/mm; respectively. Therefore, the nature of the stiffness distribution in the structure is also irregular. As a result, the structure is considered as a full-size structure, with irregular mass and stiffness distributions.

Note that the computed masses and stiffnesses are based on the as-built maps and numerical simulations, and the numerical model of the baseline (intact) structure should be verified using the experimental data of the healthy structure. In the following subsection, the experiments as well as model verification and damage detection results are discussed.

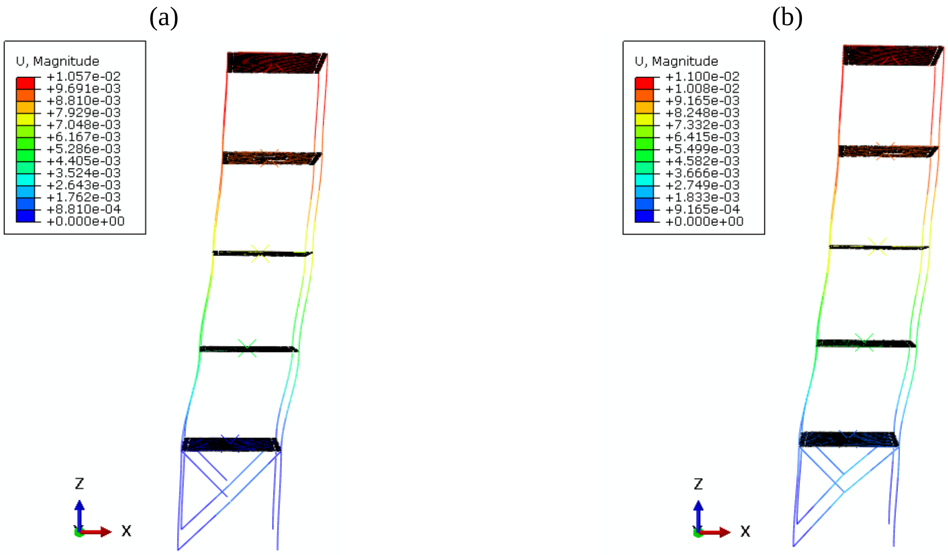

Figure 3.18: Static displacements of the UNISON tower under F_j = 2000 N, j=1, 2, 3, 4, and 5; modeled in ABAQUS for (a) intact and (b) damaged cases.

3.4.2.2. Experiments and data acquisition

The structure was excited by randomly generated acceleration with 600 sec duration using an exciter device placed at the fourth floor (see Figure 3.14(b)). The time history of acceleration responses was measured by sensors installed at the level of the floors with a sampling frequency of 20 Hz [56]. The sensors were PCB 393B12 accelerometers with 10 Volts/g sensitivity. In Figure 3.14(b), a typical sensor installed on the structure is shown. To consider the uncertainties like measurement noise or environmental effects, the measurement was repeated seven times for each case (i.e., the intact and damaged cases), and the measured data was stored on a laptop computer through a signal coordinator and an A/D board [56]. A typical time history of acceleration responses for the damaged structure is shown in Figure 3.19.

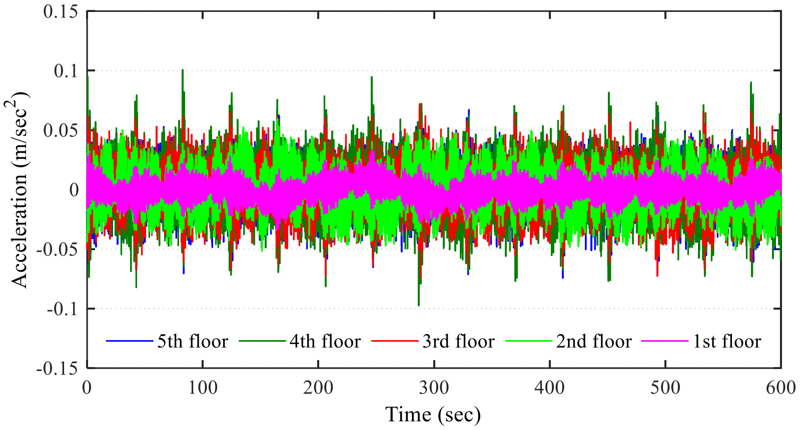

Figure 3.19: Acceleration time history responses of the damaged structure for a typical test.

The modal data of the monitored structure for all the experiments were extracted by ARTeMIS software [58]. Figure 3.20 shows the changes in the modal frequency of the first and second modes for the intact and damaged structures in all the seven independent tests. Although the changes of the frequencies can reveal damage occurrence, no more detailed information about the damage location and/or severity is inferable from frequency change plot. The mode shapes of the first and second modes are shown in Figure 3.21 for a typical test of the undamaged and damaged cases, when a full set of sensors is used for data acquisition. It is observed that the mode shapes of the undamaged and damaged structures are close together, and no clear conclusion can be drawn on the health of the structure by inspecting the mode shapes.

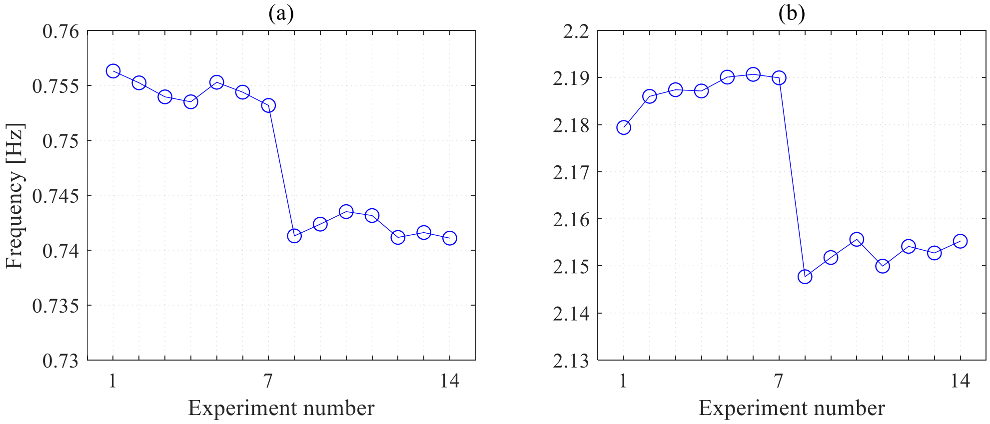

Figure 3.20: The frequencies of the UNISON tower for undamaged (experiments #1–7) and damaged (experiments #8–14) cases: (a) first mode and (b) second mode.

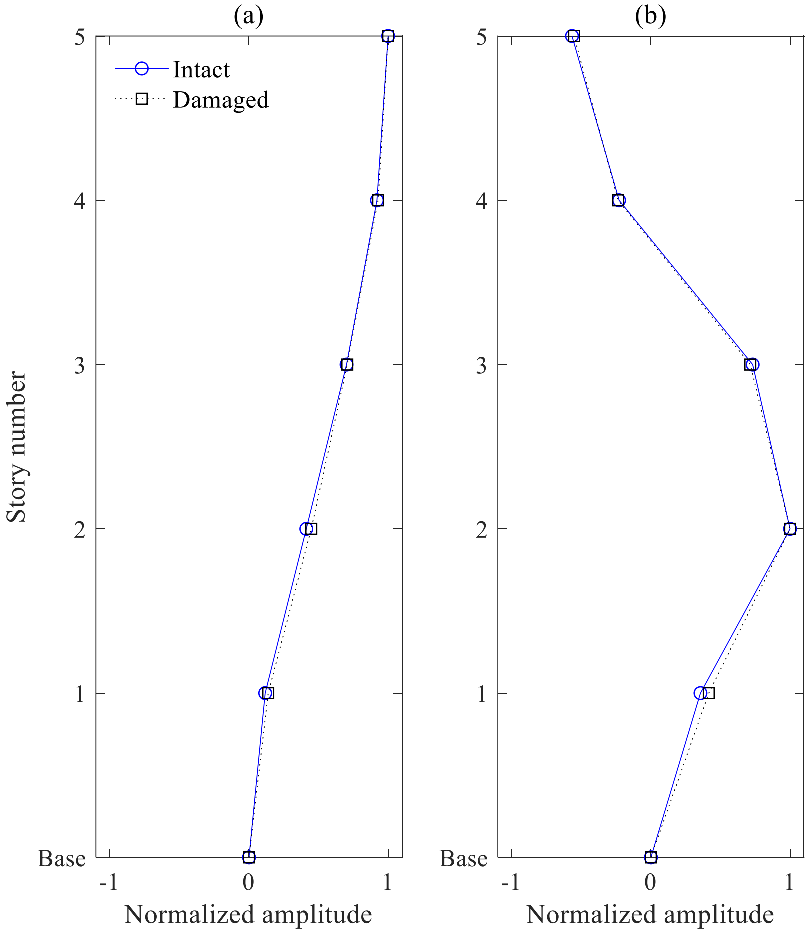

Figure 3.21: Mode shapes of the UNISON tower in the intact and damaged states: (a) first mode and (b) second mode.

3.4.2.3. Condition assessment: Evaluating the support performance

One of the important challenges in the field of structural condition assessment is the performance evaluation of the supports. Construction errors or damage at the base level of the structural systems can cause changes in the expected behavior of the supports. In the following, the behavior of the UNISON tower's supports is evaluated by a simple frequency-wise approach. Based on the design maps, the support should be a "fixed" support, which rejects all the translational and rotational displacements. Making translational restrictions is relatively easy during construction. Moreover, such restrictions mainly remain effective during the building's lifetime. Rotational restrictions and their ideal performance, however, might face uncertainties not only during the construction, but also during the structural lifetime. Herein, a numerical model of the pristine structure is developed by replacing the rotational DOF of the support with a spring, and the spring's stiffness is swept in a reasonable range to make frequency-stiffness plot for the building. Then, the frequency of the tested structure in the intact case is compared with the plot to check if the expected behavior for a fully fixed support is satisfied. In the following, a parametric study for the support evaluation in the shear buildings is presented.

First, the stiffness matrix of a 2D frame with shear behavior is derived considering rotational spring in support. Such a model is beneficial if health assessment of the supports is of interest. The element shown in Figure 3.22 represents the first story of a *N*-story shear building structure, in which, a rotational spring with stiffness of k_θ has been connected to a pinned support. Based on the DOF numbering scheme shown in this figure, the Hook's law for the element (which represents the first story) is written as:

$$\begin{Bmatrix} f_1 \\ f_2 \\ f_3 \\ f_4 \end{Bmatrix} = \frac{EI}{h^3} \begin{bmatrix} 12 & 6h & -12 & 6h \\ 6h & 4h^2 & -6h & 2h^2 \\ -12 & -6h & 12 & -6h \\ 6h & 2h^2 & -6h & 4h^2 \end{bmatrix} \begin{Bmatrix} u_1 \\ u_2 \\ u_3 \\ u_4 \end{Bmatrix} \tag{3.25}$$

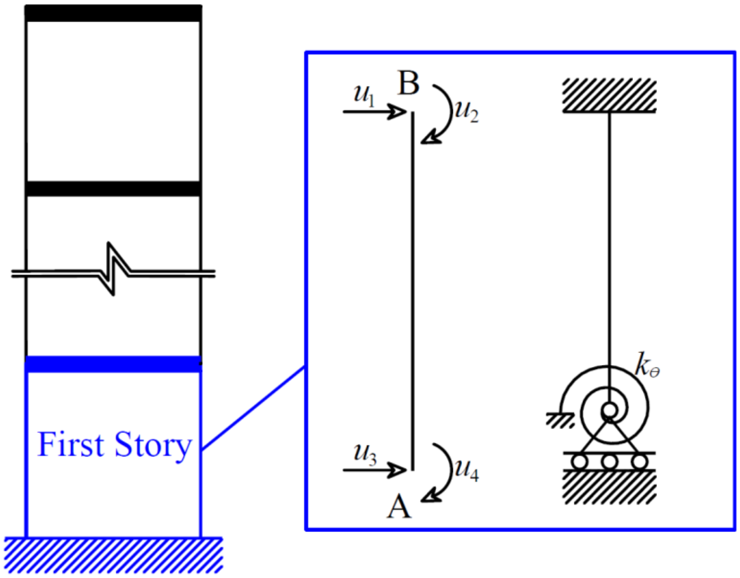

Figure 3.22: The first story of a shear building structure with rotational spring to derive the stiffness matrix of the first story, including the stiffness imposed by the support.

where, f_i and u_i are the force and displacement at the ith DOF, respectively, and E, I, and h are the Young's modulus, moment of inertia, and height of the first story, respectively. The boundary condition of point B returns u_1=u_2=0. On the other hand, it is known that $f_4 = -k_\theta u_4$. Therefore, the equation related to the fourth row of Eq. (3.25) is rewritten as:

$$-k_\theta u_4 = \frac{EI}{h^3}(-6hu_3 + 4h^2 u_4) \tag{3.26}$$

or,

$$u_4 = \frac{6EI/h^2}{(4EI/h) + k_\theta} u_3 \tag{3.27}$$

Using Eq. (3.27), the equation related to the third row of Eq. (3.25) yields:

$$f_3 = \left(\frac{12EI}{h^3} - \frac{6EI}{h^2}\frac{6EI/h^2}{(4EI/h) + k_\theta}\right) u_3 \tag{3.28}$$

where, the term in parenthesis is the total stiffness of the column with rotational spring element:

$$k_1^T = \frac{12EI}{h^3} - \frac{6EI}{h^2}\frac{6EI/h^2}{(4EI/h) + k_\theta} \tag{3.29}$$

Note that, if $k_\theta \rightarrow \infty$, then $k_1^T \rightarrow 12EI/h^3$, which means the support is completely fixed and no displacement is allowed along the rotational DOF. However, if $k_\theta \rightarrow 0$, then $k_1^T \rightarrow 3EI/h^3$, which reflects a behavior associated with a column with pinned support. Considering Eq. (3.29) and defining $k_i = 12E_iI_i/h_i^3$ as the stiffness of the ith story of a N-story structure with shear behavior, the global stiffness matrix of the system is presented as:

$$\mathbf{K} = \begin{bmatrix} k_1 - \dfrac{3k_1h^2/4}{h^2 + 3\,k_\theta/k_1} + k_2 & -k_2 & 0 & \cdots & 0 \\ -k_2 & k_2 + k_3 & -k_3 & \cdots & 0 \\ 0 & -k_3 & k_3 + k_4 & \cdots & 0 \\ \vdots & \vdots & \vdots & \ddots & \vdots \\ 0 & 0 & 0 & \cdots & k_N \end{bmatrix} \tag{3.30}$$

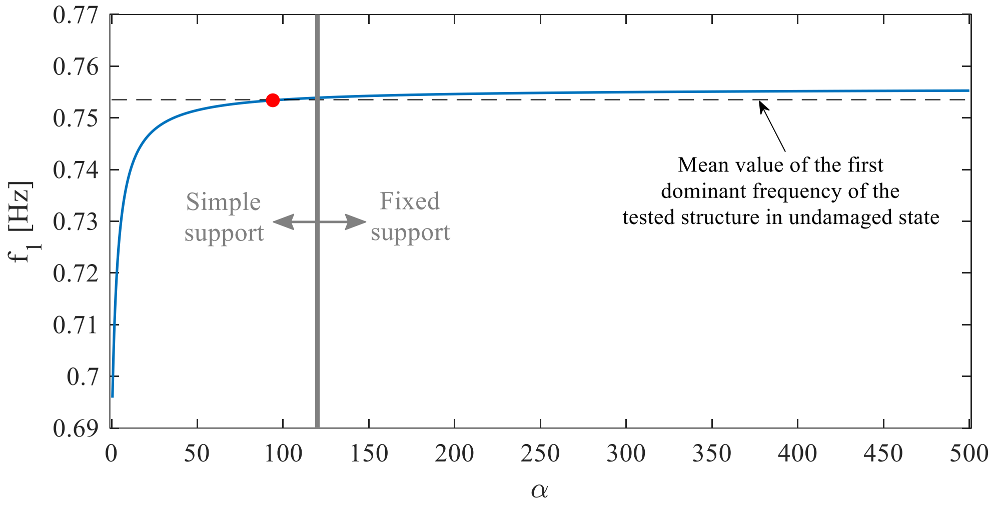

Figure 3.23: f_1-α plot to evaluate the performance of the support in UNISON tower (red point represents the behavior of the UNISON tower tested in pristine case).

where k_1 is the stiffness of the first story assuming fully fixed support, which is tuned by $0.75k_1h^2/(h^2+3\alpha)$ and α is defined as $\alpha = k_\theta/k_1$. Using Eq. (3.30) along with a lumped-mass matrix (representing the mass of the UNISON tower), the frequency of the structure can be found by the classical modal analysis. Figure 3.23 shows f_1 (the first dominant frequency) as a function of α. Based on this figure, if α is equal or greater than ~120, the first dominant frequency of the system is almost a fixed number and this is the optimal α to consider the behavior of the support as fully fixed support. To evaluate the performance of the support in UNISON tower, the mean value of the first frequency (computed by analyzing the acquired data from seven independent tests conducted on the pristine structure) is used to find α from f_1-α plot. Referring to Figure 3.23, $\alpha = 95$ for the UNISON tower, which reveals almost fully fixed behavior of the support.

3.4.2.4. Damage detection results

The proposed method is used for damage detection and quantification in the UNISON tower. Three configurations for sensor installation were considered:

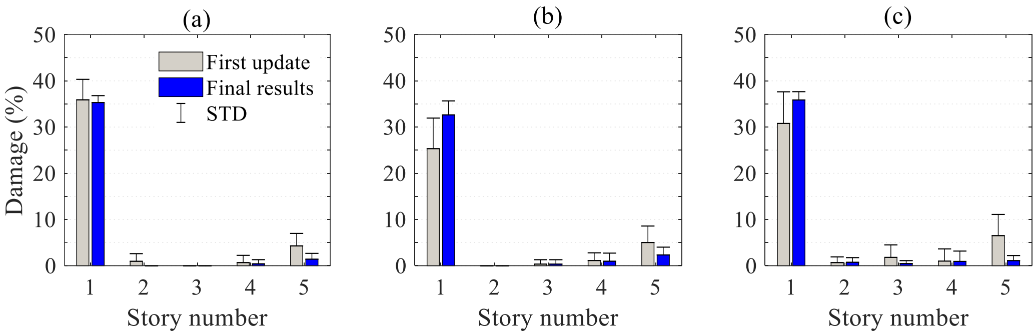

Figure 3.24: The mean and one standard deviation of the obtained damage detection results for UNISON tower in the damaged case (*p*=2): (a) Config. 1, (b) Config. 2, and (c) Config. 3.

- Config. 1: Sensors are attached to all the floors,
- Config. 2: Three sensors are attached to the 1st, 4th, and 5th floors, and
- Config. 3: Three sensors are attached to the 2nd, 3rd, and 5th floors.

Although sensors were attached to all the floors in Config. 1, in Configs. 2 and 3 only three floors were equipped with the sensors. Moreover, in Config. 2, there is a sensor at the level of the first floor, which represents the DOF directly related to the damaged story. In Config. 3, however, sensors were attached to the DOFs with no connection to the damaged story.

In each configuration, the numerical model of the structure was developed in MATLAB and the modal data of the first two modes in the intact state was used to update the baseline model to a verified model. Then, the verified baseline model was served as the analytical baseline model (with unknown damage severities) for damage identification. Similar to section 3.4.1, the stop criterion for iterative model updating procedure is defined by setting ε equal to 1×10^{-10} (see Figure 3.1 to find ε's definition). Figure 3.24 shows the mean and one standard deviation of the obtained damage detection results for the seven independent tests of the damaged structure. The results associated with initial update (i.e., updating the verified baseline model to the AB model) as well as the final damage detection results have been shown in this figure. The first update returns initial estimation of the damage severities, which contains false-positive results, reporting the fifth story as a damaged story. The final results —which are the results of further updates aimed at tuning the damage parameters reported in the AB model— return more accurate damage severities. Note that the standard deviations of the obtained results are small numbers, which is interpreted as high precision (or repeatability) of the proposed method in solving ill-posed problems. Specifically, the standard deviations of the final results are relatively less than the standard deviations of the initial results (used to form the AB model), which reveals the robust performance of the proposed iterative algorithm in tuning the initial estimations. In addition, the results emphasize the acceptable performance of the proposed method in structural damage detection using sparse sensor measurements.

Chapter 4: A Data-Driven Matched Field Processing for Defect Detection in Plates: Preliminary Study

4.1. Introduction

Matched Field Processing (MFP) is a generalized beamforming method that matches the received data to a dictionary of replica vectors to localize source(s) (e.g., acoustic sources) in the complex media [59, 60]. The approach has also been used for passive structural monitoring and defect detection [61–63]. The MFP requires an accurate model of medium, and this is a challenge in some applications. To tackle this issue, data-driven MFP has been recently introduced [64, 65]. Data-driven methods are considered as *model-free* methods which do not require prior knowledge of the propagation environment to localize a defect. This chapter introduces a data-driven MFP method for defect detection in plates. The replica vectors are made using the Fast Fourier Transform (FFT) of the time history responses of the pristine plate under excitation induced by an impact hammer. Subtracting the data of the pristine plate from the data of the damaged plate, a set of data is extracted which contains the *acoustic signature* of the defect. This set of data is then used for MFP by means of conventional Bartlett processor and adaptive beamformers, like Minimum Variance (MV) and White Noise Constraint (WNC). The method is used for defect identification in an aluminum plate.

4.2. The method

Consider a plate with N attached sensors as the receivers. Applying an external excitation, the received time history responses with the sensors are denoted by $\mathbf{d}_i$, $i = 1, 2, \ldots, N$. The MFP can be used to identify the location of the applied excitation, $\mathbf{x}_a$, by backpropagating the received data and matching them up with a dictionary of the possible look directions (i.e., replicas). For this purpose, a numerical model of the plate should be developed knowing the properties of the medium. Then, the response of the plate to a virtual exciting noise should be analytically extracted by placing the excitation in a typical point $\mathbf{x}_j$, $j = 1, 2, \ldots, N_e$. These points are considered as the candidate look directions (or sources) and the FFT of the associated responses in a certain frequency, f, is used to make the dictionary of replica vectors, $\{\mathbf{w}(\mathbf{x}_j)\}$. Note that each replica vector contains N entries. Correlating the replicas with the backpropagated data (in the frequency domain) can identify the source location. Different beamformers can be used for this purpose. In this study, the conventional Bartlett beamformer as well as two well-known adaptive beamformers, Minimum Variance (MV) and Whine Noise Constraint (WNC), are used. In the following, these beamformers are briefly introduced.

The *Bartlett processor* is a spatial matched filter processor which inspects the amount of correlation between the normalized replica vectors and the data [59]. Using the FFT of the received data in a certain frequency (denoted by $\mathbf{s}(f)$, which is a vector with N complex entries), the Cross-Spectral Density Matrix (CSDM), $\mathbf{C}$, is derived as follows:

$$\mathbf{C} = \mathbf{s}(f).\mathbf{s}^H(f) \tag{4.1}$$

in which, H denotes the Hermitian operator. Note that $\mathbf{C}$ is an N by N matrix. For a candidate source location $\mathbf{x}_j$, the Bartlett output is computed as:

$$P_B(\mathbf{x}_j) = \mathbf{w}^H(\mathbf{x}_j).\mathbf{C}.\mathbf{w}(\mathbf{x}_j) \tag{4.2}$$

Generally, the peak-to-background ratio is not optimal in Bartlett processor because of high sidelobes [64]. But adaptive beamformers, like MV and WNC, can return results with high resolution.

The *MV processor* is defined as follows [66]:

$$P_{MV}(\mathbf{x}_j) = \mathbf{w}_{MV}^H(\mathbf{x}_j).\mathbf{C}.\mathbf{w}_{MV}(\mathbf{x}_j) \tag{4.3}$$

where,

$$\mathbf{w}_{MV}(\mathbf{x}_j) = \frac{\mathbf{C}^{-1}.\mathbf{w}(\mathbf{x}_j)}{\mathbf{w}^H(\mathbf{x}_j).\mathbf{C}^{-1}.\mathbf{w}(\mathbf{x}_j)} \tag{4.4}$$

Comparing to the Bartlett processor, the MV can return results with higher resolution; however, it is very sensitive to any mismatch between the data vector and the replica vector [67].

The *WNC processor* is another adaptive beamformer which can tackle modest mismatches induced by the modelling errors or manipulation of the received data [67, 68]. The WNC processor is defined as:

$$P_{WN}(\mathbf{x}_j) = \mathbf{w}_{WN}^H(\mathbf{x}_j).\mathbf{C}.\mathbf{w}_{WN}(\mathbf{x}_j) \tag{4.5}$$

where,

$$\mathbf{w}_{WN}(\mathbf{x}_j) = \frac{(\mathbf{C} + \alpha\mathbf{I})^{-1}.\mathbf{w}(\mathbf{x}_j)}{\mathbf{w}^H(\mathbf{x}_j).(\mathbf{C} + \alpha\mathbf{I})^{-1}.\mathbf{w}(\mathbf{x}_j)} \tag{4.6}$$

in which, $\mathbf{I}$ is the identity matrix, and α is the added white noise which not only reduces the signal gain degradation induced by mismatches, but also makes ($\mathbf{C}+\alpha\mathbf{I}$) invertible.

$\mathbf{x}$ of the maximum P for a given beamformer represents the source location. In the mentioned formulations, the dictionary of the replica vectors is formed by numerical simulations using the specifications of the propagation environment. Employing a data-driven method can result in a model-free approach to make the dictionary of the replica vectors. For this purpose, all the candidate points of the given test piece are perturbated with a controlled noise excitation and the received data by N sensors are processed to make the replica vectors. Then, the data-driven replica dictionary can be correlated with a given test data to localize the excitation source. Note that using such a dictionary, the environmentally induced mismatch in the replicas will considerably be reduced.

In the following, the mentioned method is generalized for defect localization. The defect can be defined as a perturbation (or a secondary source) in the environment which can be potentially identified by tracking the acoustic signature of the environment if the response data is isolated in a way that any other set of responses induced by the primary source is removed or weakened. Under the Born approximation, such an isolated data set can be reached by subtracting the response data of the pristine structure from the response data of the damaged structure as follows:

$$\mathbf{d}_{dif,i} = \mathbf{d}_{m,i} - \mathbf{d}_{p,i} \quad , \qquad i = 1, 2, \ldots, N \tag{4.7}$$

where, $\mathbf{d}_{m,i}$ and $\mathbf{d}_{p,i}$ denote the data acquired by the *i*th sensor under a controlled noise perturbation at a certain location in the damaged and pristine states, respectively, and $\mathbf{d}_{dif,i}$ is the isolated data set (associated with the *i*th sensor), which is of interest for defect localization. Applying the excitation at a certain location is important to assure that the primary source's acoustic effect will be removed from the test data. Next, the MFP can be applied to the set of $\mathbf{d}_{dif}$s for defect detection and localization using the described beamformers. In the next section, the presented data-driven method is used for not only impact source detection, but also defect localization in a plate.

4.3. Experimental study

Figure 4.1 shows the experimental setup, which is a small 15 cm by 15 cm thin aluminum plate with a central 10 cm by 10 cm grid of cells —containing a total of 25 cells (each 2 cm by 2 cm). The plate is placed on three fixed supports (shown in Figure 4.1(a)), which provides the plate with enough freedom

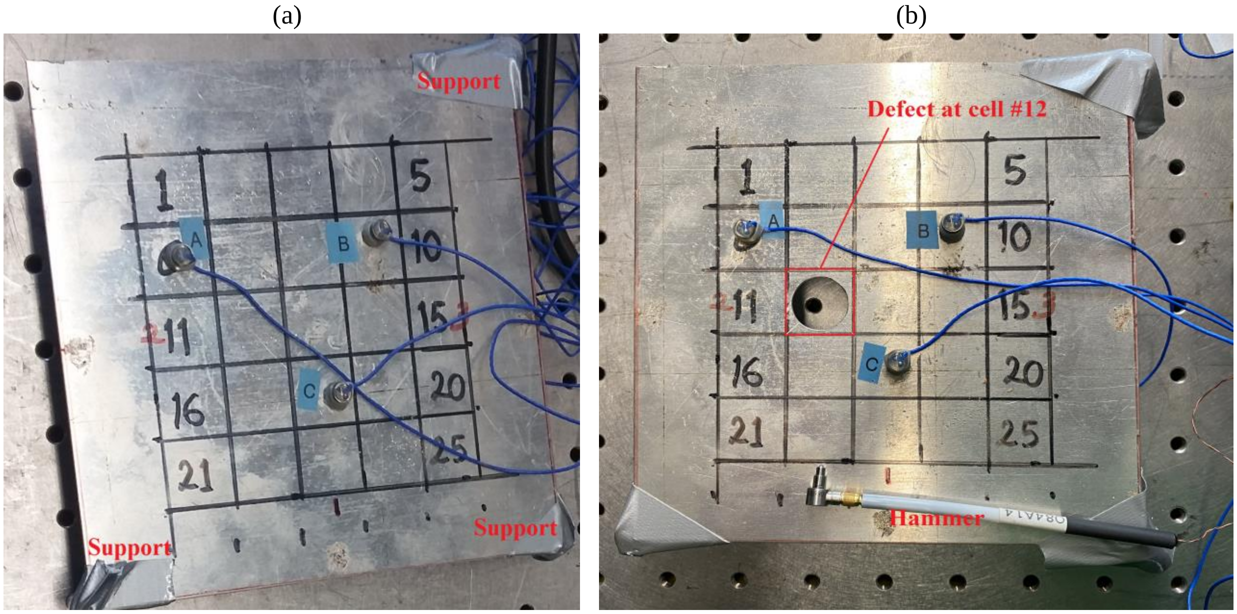

Figure 4.1: (a) Pristine plate and (b) damaged plate. A small hammer is used to excite the plate.

to vibrate under a broad-band excitation applied by an impact hammer. Three PCB shear accelerometers (placed in cells #6, #9 and #18) are used for data acquisition. A defect, as a hole drilled in cell #12 (see Figure 4.1(b)) is also made to evaluate the applicability of the presented method for defect localization. The pristine plate was excited using a small impact hammer (shown in Figure 4.1) by hitting the center of all the 25 cells, and the time history responses (with a sampling frequency of 80 MHz) were saved in a laptop for further analysis. A lowpass filter (with cutoff frequency of 10 kHz) was applied to the data. Moreover, the data was downsampled by a factor of 400 and a truncated version of the data in an interval of [0.5t 0.75t], t is the total acquisition time, was proceeded to the next steps. Note that in some cases, some of the received signals at the first instances were in outside of the accelerometers' acceptable range, which formed a saturated time history response. The mentioned data preparation step can fix such issues.

4.3.1. Primary source localization

Using the data-driven replica dictionary, the MFP can be implemented to localize the impact source. Using acquired data in the pristine case, the dictionary of the replica vectors was made. Then, data sets of the excitations applied to cells #1, #5, #20, and #23, were selected as the impact sources to perform the primary source localization. Here, there is a complete match between the test data and candidate solutions in the replica dictionary because the test data are selected from the developed dictionary. The main purpose of this study is to highlight the promising and shortcomings of the beamformers in source localization using the presented data-driven method. The obtained results are shown in Figures 4.2 to 4.5. Note that all the calculations were performed using the frequency associated with the first peak in the FFT plot of the test data. All the results emphasize the acceptable performance of the data-driven MFP in localizing the impact source. The beauty of the data-driven methods is that, they are categorized as model-free methods and no details of the environment's specifications is required. In terms of the performance of the employed beamformers, all can effectively localize the primary sources; however, the MV and WNC (specified as 10 dB down) return results with higher resolutions and the lower sidelobes comparing with the Bartlett processor. It is worth mentioning that because of a perfect match between the replicas and test data, the maximum values of the processors (appeared at the location of the detected primary source) are identical for a given case.

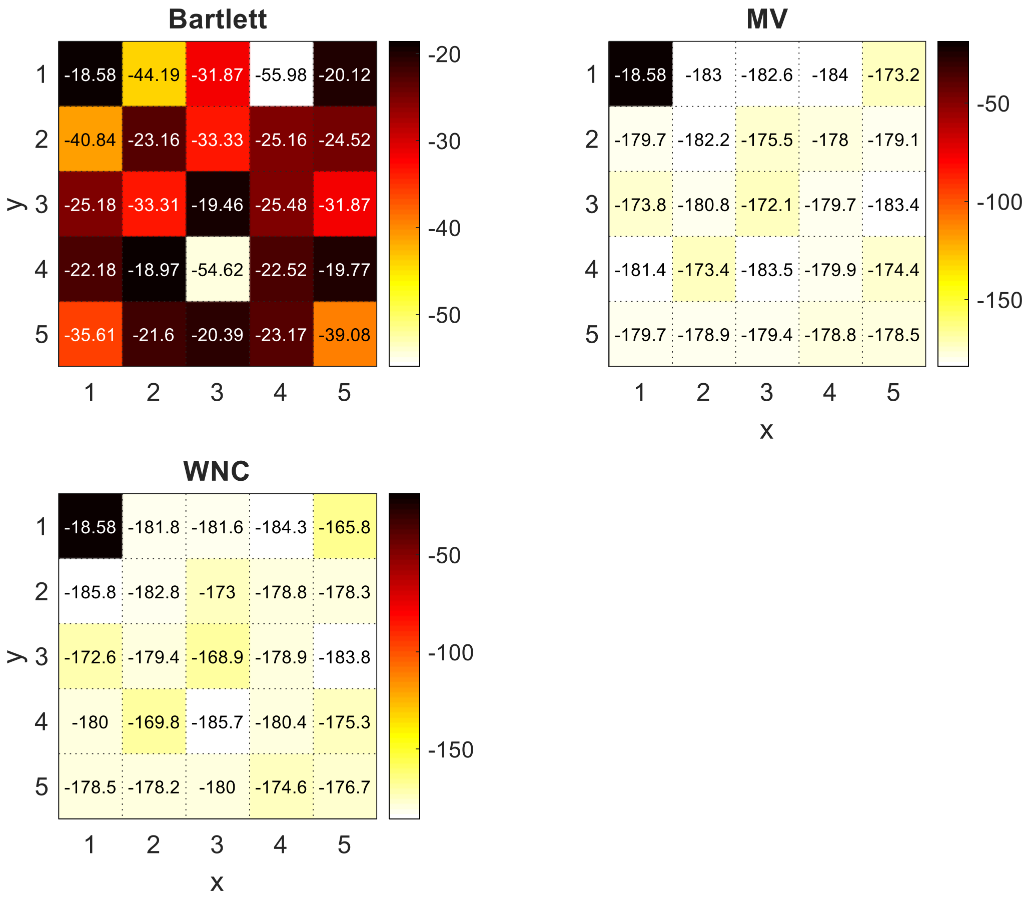

Bartlett

y \ x	1	2	3	4	5
1	-18.58	-44.19	-31.87	-55.98	-20.12
2	-40.84	-23.16	-33.33	-25.16	-24.52
3	-25.18	-33.31	-19.46	-25.48	-31.87
4	-22.18	-18.97	-54.62	-22.52	-19.77
5	-35.61	-21.6	-20.39	-23.17	-39.08

MV

y \ x	1	2	3	4	5
1	-18.58	-183	-182.6	-184	-173.2
2	-179.7	-182.2	-175.5	-178	-179.1
3	-173.8	-180.8	-172.1	-179.7	-183.4
4	-181.4	-173.4	-183.5	-179.9	-174.4
5	-179.7	-178.9	-179.4	-178.8	-178.5

WNC

y \ x	1	2	3	4	5
1	-18.58	-181.8	-181.6	-184.3	-165.8
2	-185.8	-182.8	-173	-178.8	-178.3
3	-172.6	-179.4	-168.9	-178.9	-183.8
4	-180	-169.8	-185.7	-180.4	-175.3
5	-178.5	-178.2	-180	-174.6	-176.7

Figure 4.2: The obtained results for the primary source localization (values are in [dB]). The actual location of the primary source: cell #1, located in the first row/first column.

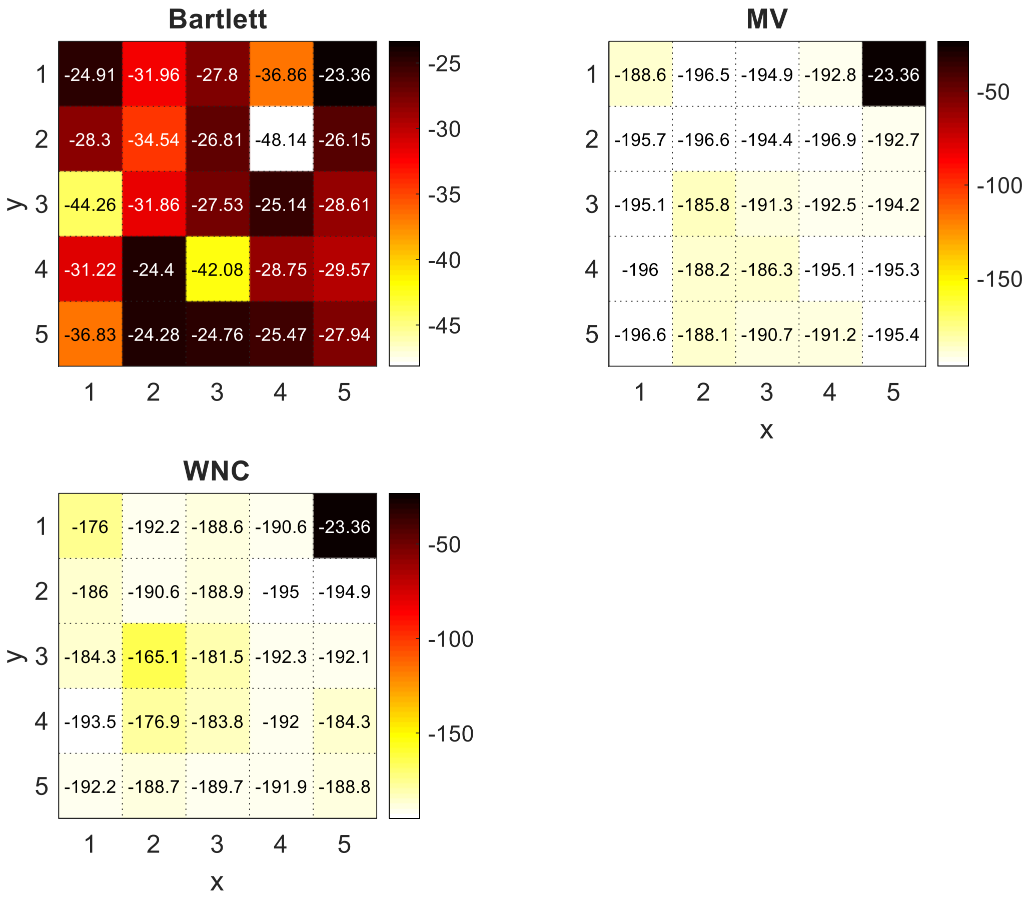

Bartlett

y \ x	1	2	3	4	5
1	-24.91	-31.96	-27.8	-36.86	-23.36
2	-28.3	-34.54	-26.81	-48.14	-26.15
3	-44.26	-31.86	-27.53	-25.14	-28.61
4	-31.22	-24.4	-42.08	-28.75	-29.57
5	-36.83	-24.28	-24.76	-25.47	-27.94

MV

y \ x	1	2	3	4	5
1	-188.6	-196.5	-194.9	-192.8	-23.36
2	-195.7	-196.6	-194.4	-196.9	-192.7
3	-195.1	-185.8	-191.3	-192.5	-194.2
4	-196	-188.2	-186.3	-195.1	-195.3
5	-196.6	-188.1	-190.7	-191.2	-195.4

WNC

y \ x	1	2	3	4	5
1	-176	-192.2	-188.6	-190.6	-23.36
2	-186	-190.6	-188.9	-195	-194.9
3	-184.3	-165.1	-181.5	-192.3	-192.1
4	-193.5	-176.9	-183.8	-192	-184.3
5	-192.2	-188.7	-189.7	-191.9	-188.8

Figure 4.3: The obtained results for the primary source localization (values are in [dB]). The actual location of the primary source: cell #5, located in the first row/fifth column.

4.3.2. Secondary source (damage) localization

Using the impact hammer, the damaged plate was excited by hitting at the center of the plate (i.e., cell #13). As the first investigation, the necessity of the introduced differencing method (Eq. (4.7)) is illustrated. Figure 4.6 shows the MFP-based defect localization results for a case that $\mathbf{d}_m$ was used as the test data (with no subtraction between the data of the damaged and pristine states). Moreover, the replica vectors were made using the data acquired from the pristine state. Based on this figure, the location of the both secondary source (i.e., the defect, which is in cell #12, located in the third row/second column) and primary source (i.e., the impact location, which is in cell #13, located in the third row/third column) are highlighted. This means that two perturbation sources, associated with the location of the impact and defect, are reported in the ambiguity plot of the damaged plate. Note that the MFP evaluates the energy of the scattered waves and there is no difference between the primary (impact) and secondary (defect) sources in terms of wave scattering. Eq. (4.7) is an effort to isolate the data which are purely related to the energy scattering induced by the defect. In the following, the presented method is applied for defect detection. Different steps of the method are summarized as below:

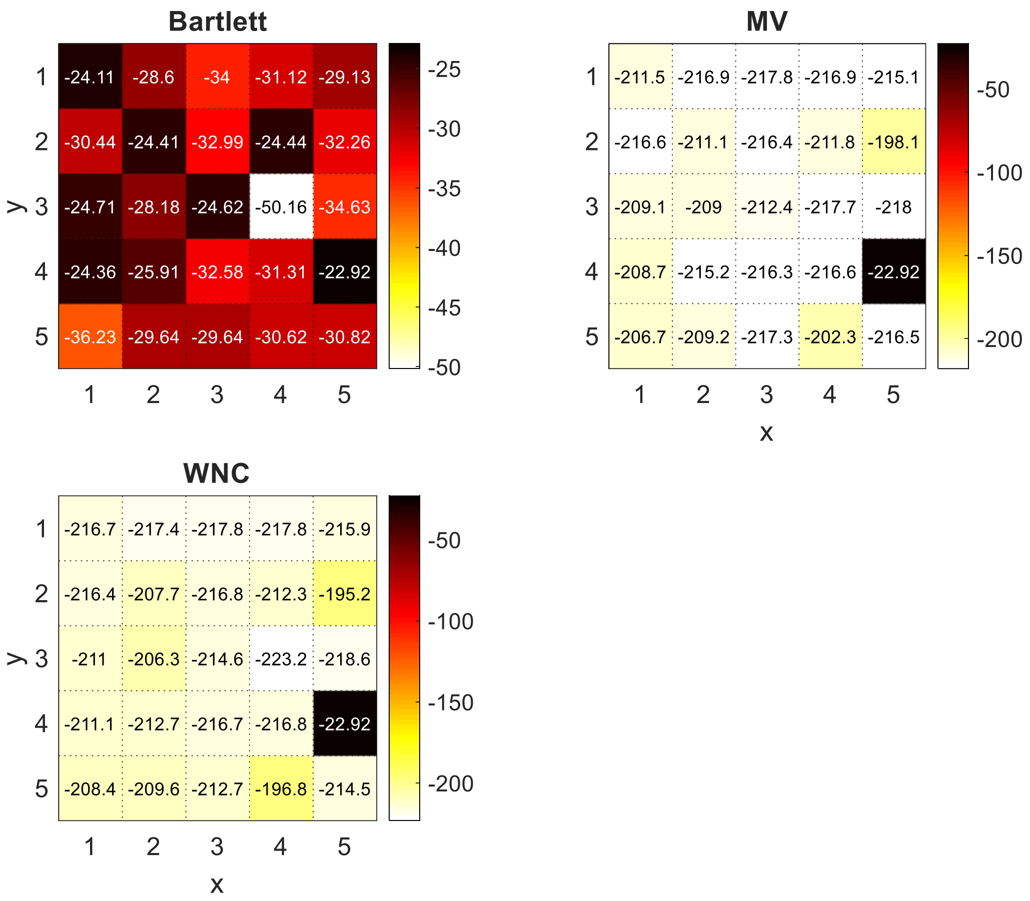

Bartlett

y	1	2	3	4	5
1	-24.11	-28.6	-34	-31.12	-29.13
2	-30.44	-24.41	-32.99	-24.44	-32.26
3	-24.71	-28.18	-24.62	-50.16	-34.63
4	-24.36	-25.91	-32.58	-31.31	-22.92
5	-36.23	-29.64	-29.64	-30.62	-30.82

MV

y	1	2	3	4	5
1	-211.5	-216.9	-217.8	-216.9	-215.1
2	-216.6	-211.1	-216.4	-211.8	-198.1
3	-209.1	-209	-212.4	-217.7	-218
4	-208.7	-215.2	-216.3	-216.6	-22.92
5	-206.7	-209.2	-217.3	-202.3	-216.5

WNC

y	1	2	3	4	5
1	-216.7	-217.4	-217.8	-217.8	-215.9
2	-216.4	-207.7	-216.8	-212.3	-195.2
3	-211	-206.3	-214.6	-223.2	-218.6
4	-211.1	-212.7	-216.7	-216.8	-22.92
5	-208.4	-209.6	-212.7	-196.8	-214.5

Figure 4.4: The obtained results for the primary source localization (values are in [dB]). The actual location of the primary source: cell #20, located in the fourth row/fifth column.

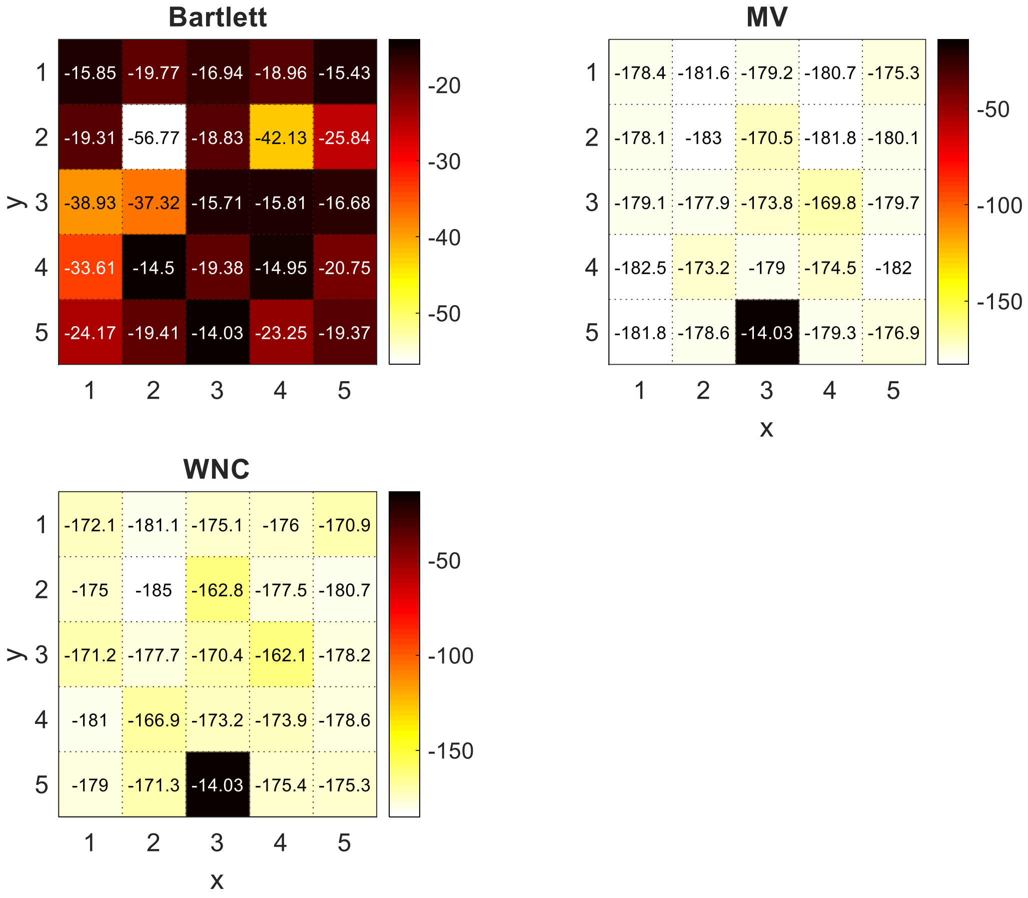

Figure 4.5: The obtained results for the primary source localization (values are in [dB]). The actual location of the primary source: cell #23, located in the fifth row/third column.

- For a certain frequency, the data-driven replica vectors are computed using the time history responses of the pristine plate,
- Eq. (4.7) is formed using the time history responses of the damaged and pristine plates, when the excitation (i.e., controlled noise) is applied at cell #13,
- For the selected certain frequency, the MFP is performed using the Bartlett, MV, and WNC processors.

The obtained results are shown in Figure 4.7. Based on this figure, all the beamformers can identify the location of the defect. Note that the sidelobes of the Bartlett processor are relatively high and for this

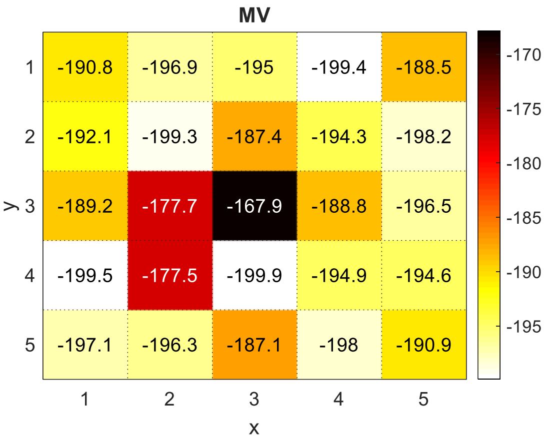

MV

y \ x	1	2	3	4	5
1	-190.8	-196.9	-195	-199.4	-188.5
2	-192.1	-199.3	-187.4	-194.3	-198.2
3	-189.2	-177.7	-167.9	-188.8	-196.5
4	-199.5	-177.5	-199.9	-194.9	-194.6
5	-197.1	-196.3	-187.1	-198	-190.9

Figure 4.6: The results of the MV processor for the secondary source (defect) localization without applying the subtraction step defined by Eq. (4.7) (values are in [dB]).

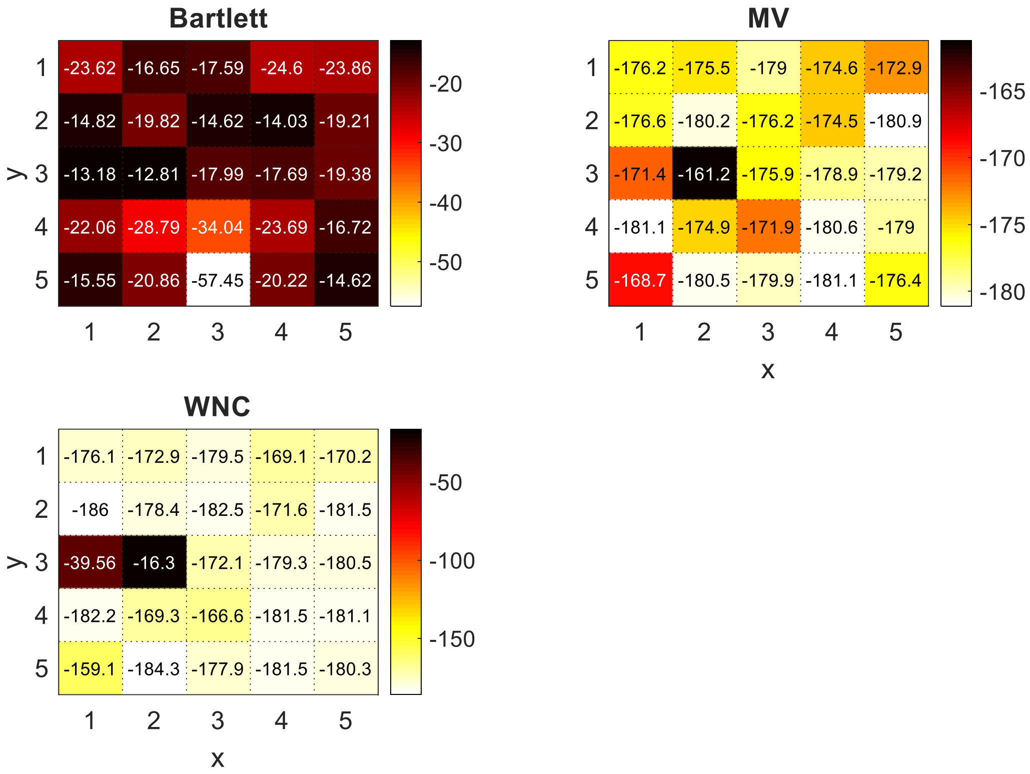

Bartlett

y \ x	1	2	3	4	5
1	-23.62	-16.65	-17.59	-24.6	-23.86
2	-14.82	-19.82	-14.62	-14.03	-19.21
3	-13.18	-12.81	-17.99	-17.69	-19.38
4	-22.06	-28.79	-34.04	-23.69	-16.72
5	-15.55	-20.86	-57.45	-20.22	-14.62

MV

y \ x	1	2	3	4	5
1	-176.2	-175.5	-179	-174.6	-172.9
2	-176.6	-180.2	-176.2	-174.5	-180.9
3	-171.4	-161.2	-175.9	-178.9	-179.2
4	-181.1	-174.9	-171.9	-180.6	-179
5	-168.7	-180.5	-179.9	-181.1	-176.4

WNC

y \ x	1	2	3	4	5
1	-176.1	-172.9	-179.5	-169.1	-170.2
2	-186	-178.4	-182.5	-171.6	-181.5
3	-39.56	-16.3	-172.1	-179.3	-180.5
4	-182.2	-169.3	-166.6	-181.5	-181.1
5	-159.1	-184.3	-177.9	-181.5	-180.3

Figure 4.7: Defect localization results in the tested thin aluminum plate.

reason the defect location cannot be identified with high resolution. The MV can clearly identify the defect location with a better resolution comparing with Bartlett processor, but the sidelobes are still in high levels.

The WNC can identify the location of the defect with the highest resolution. As expected, the WNC can strongly suppress the sidelobes and the defect location is clearly highlighted.

Chapter 5: Conclusions

This thesis was focused on smart sensing and structural damage detection. First, a machine learning-based method was proposed for image classification using BoW and SVM techniques. The method was successfully used for tie/ballast image classification at the Rail Defect Testing Facility of UC San Diego. Second, a vibration-based damage detection method was proposed using the static deflections of the structural systems computed with the modal data of the first several modes. This method was applied to damage localization and quantification in a lab-scale five-story shear building structure tested on a shake table as well as a full-scale high-rise building. The results emphasized the accuracy and precision of the proposed method in damage detection even though sparse sensor measurements were used as the test data. Data-driven MFP was the last concept covered in this thesis. The MFP has been used for defect detection. But most of the methods require information of the environment to obtain the dictionary of the replicas (as the candidate solutions). Using data-driven concept, a model-free approach is developed for MFP which can be used for defect localization if the difference between the responses of the damaged and pristine systems is fed to the processor. The method was employed for defect detection in an aluminum plate using the conventional and adaptive beamformers. The results indicated WNC as the best processor for defect detection with high resolution for this application.

In the following, suggestions for future investigations are listed:

- Using GigE cameras to tackle the buffer issues in saving images: A USB3.0 camera was used in Chapter 2 to capture tie/ballast images and save them in a computer system. Although this camera was able to efficiently capture and save the images, some of the frames were missed because of buffer issues. Using GigE cameras can help to tackle this issue because GigE cameras can be connected to Real Time Performing Systems (RTPS) offering higher buffer size.

- Investigating the applicability of the proposed vibration-based damage detection method in identifying damages in top stories: Based on the experimental data availability, the proposed method in Chapter 3 was used for detecting damages occurred in the first story. The application of the method has been numerically investigated by the author for detecting damages in other stories; however, experimental validations are needed.
- Employing “Spatial Smoothing” to remove (or weaken) the effects of the primary acoustic source in data-driven MFP-based defect detection method: In Chapter 4, the signature of the primary source was removed using a subtraction method. Another method can be investigated employing a Spatial Smoothing [69] approach, which uses the details of the excitation location of in the damaged plate to weaken the signature of the primary source and highlight the secondary source.

References

[1] P. C. Chang, A. Flatau, S. C. Liu. 2003. “Review paper: Health monitoring of civil infrastructure,” Structural Health Monitoring, 2(3): 257–267.

[2] J. P. Lynch, K. J. Loh. 2006. “A summary review of wireless sensors and sensor networks for structural health monitoring,” The Shock and Vibration Digest, 38(2): 91–128.

[3] C. R. Farrar, K. Worden. 2007. “An introduction to structural health monitoring,” Philosophical Transactions of the Royal Society of London A: Mathematical, Physical and Engineering Sciences, 365(1851): 303–315.

[4] J. M. W. Brownjohn. 2007. “Structural health monitoring of civil infrastructure,” Philosophical Transactions of the Royal Society, Series A: Mathematical, Physical and Engineering Sciences, 365(1851): 589–622.

[5] X. Wang, C. C. Chang, L. Fan. 2001. “Nondestructive damage detection of bridges: A status review,” Advances in Structural Engineering, 4(2): 75–91.

[6] S. K. Verma, S. S. Bhadauria, S. Akhtar. 2013. “Review of nondestructive testing methods for condition monitoring of concrete structures,” Journal of Construction Engineering, 2013, 834572.

[7] P. Cawley. 2018. “Structural health monitoring: Closing the gap between research and industrial deployment,” Structural Health Monitoring, 17(5): 1225–1244.

[8] O. Avci, O. Abdeljaber, S. Kiranyaz, M. Hussein, M. Gabbouj, D. J. Inman. 2021. “A review of vibration-based damage detection in civil structures: From traditional methods to Machine Learning and Deep Learning applications,” Mechanical Systems and Signal Processing, 147, 107077.

[9] S. Livens, P. Scheunders, G. Van de Wouwer, D. Van Dyck, H. Smets, J. Winkelmans, W. Bogaerts. 1996. “A texture analysis approach to corrosion image classification,” Microscopy Microanalysis Microstructures 7(2): 143–152.

[10] R. J. Dekker. 2003. “Texture analysis and classification of ERS SAR images for map updating of urban areas in The Netherlands,” IEEE Transactions on Geoscience and Remote Sensing, 41(9): 1950–1958.

[11] M. O’Byrne, F. Schoefs, B Ghosh, V. Pakrashi. 2013. “Texture analysis based damage detection of ageing infrastructural elements,” Computer-Aided Civil and Infrastructure Engineering, 28(3): 162–177.

[12] P. Zhou, G. Zhou, Z. He, C. Tang, Z. Zhu, W. Li. 2019. “A novel texture-based damage detection method for wire ropes,” Measurement, 106954.

[13] S. Kabir, P. Rivard, G. Ballivy. 2008. “Neural-network-based damage classification of bridge infrastructure using texture analysis,” Canadian Journal of Civil Engineering, 35(3): 258–267.

[14] J. Deng, Y. Lu, V. C-H. Lee. 2020. “Imaging-based crack detection on concrete surfaces using You Only Look Once network,” Structural Health Monitoring, 1–16, DOI: 10.1177/1475921720938486.

[15] M. O. Sghaier, R. Lepage. 2015. "Road damage detection from VHR remote sensing images based on multiscale texture analysis and dempster shafer theory," 2015 IEEE International Geoscience and Remote Sensing Symposium (IGARSS), 26–31 July 2015, Milan, Italy.

[16] Z. Tong, J. Gao, A. Sha, L. Hu, S. Li. 2018. "Convolutional Neural Network for asphalt pavement surface texture analysis," Computer-Aided Civil and Infrastructure Engineering, 33(12): 1056–1072.

[17] V. Andrearczyk, P. F. Whelan. 2017. "Chapter 4 - Deep learning in texture analysis and its application to tissue image classification," Biomedical Texture Analysis, Fundamentals, Tools and Challenges, 95–129.

[18] H. Yu, B. P. Marquis, D. Y. Jeong. 2017. "Failure analysis of railroad concrete crossties in the center negative flexural mode using finite element method," Proceedings of the Institution of Mechanical Engineers, Part F: Journal of Rail and Rapid Transit, 231(5): 610–619.

[19] H. Yu. 2016. "Estimating deterioration in the concrete tie-ballast interface based on vertical tie deflection profile: a numerical study," JRC2016-5783, Proceedings of ASME Joint Rail Conference, Columbia, SC, April 2016, pp. 1–9.

[20] L. Liu, J. Chen, P. Fieguth, G. Zhao, R. Chellappa, M. Pietikäinen. 2019. "From BoW to CNN: Two decades of texture representation for texture classification," International Journal of Computer Vision, 127: 74–109.

[21] M. Mirmehdi, X. Xie, J. Suri. 2008. "Handbook of texture analysis," Imperial College Press, London, UK.

[22] D. Yan, K. Li, S. Gu, L. Yang. 2020. "Network-based Bag-of-Words model for text classification," IEEE Access, 8: 82641–82652.

[23] C. Wang, K. Huang. 2015. "How to use Bag-of-Words model better for image classification," Image and Vision Computing, 38: 65–74.

[24] L. Sharan, C. Liu, R. Rosenholtz, E. Adelson. 2013. "Recognizing materials using perceptually inspired features," International Journal of Computer Vision, 103(3): 348–371.

[25] S. Ullman, M. Vidal-Naquet, E. Sali. 2002. "Visual features of intermediate complexity and their use on classification," Nature Neuroscience, 5(7): 682–687.

[26] C. Tomasi, T. Kanade. 1991. "Detection and tracking of point features," Technical Report (CMU-CS-91-132), Carnegie Mellon University, Pittsburgh, PA, pp. 1-38, April 1991.

[27] J. Hedborg, J. Skoglund, M. Felsberg. "KLT tracking implementation on the GPU," https://www.diva-portal.org/smash/get/diva2:241567/FULLTEXT01.pdf.

[28] H. Bay, A. Ess, T. Tuytelaars, K. Van Gool. 2008. "Speeded-Up Robust Features (SURF)," Computer Vision and Image Understanding. 110(3): 346–359.

[29] R. Gove, J. Faytong. 2012. "Chapter 4 - Machine learning and event-based software testing: Classifiers for identifying infeasible GUI event sequences," Advances in Computers, 86: 109–135.

[30] M. Y. Kao. 2008. "Encyclopedia of algorithms," Springer, ISBN 978-0-387-30162-4.

[31] M. A. Hearst, S. T. Dumais, E. Osuna, J. Platt, B. Scholkopf. 1998. “Support vector machines,” IEEE Intelligent Systems and their Applications, 13(4): 18–28.

[32] V. N. Gudivada, M. T. Irfan, E. Fathi, D. L. Rao. 2016. “Chapter 5 - Cognitive analytics: Going beyond big data analytics and machine learning,” Handbook of Statistics, 35: 169–205.

[33] MATLAB. 2019. version R2019a. The MathWorks, Inc.

[34] S. W. Doebling, C. R. Farrar, M. B. Prime. 1998. “A summary review of vibration-based damage identification methods,” The Shock and Vibration Digest, 30(2): 91–105.

[35] S. W. Doebling, C. R. Farrar, M. B. Prime, D. W. Shevitz. 1996. “Damage identification and health monitoring of structural and mechanical systems from changes in their vibration characteristics: A literature review,” Los Alamos National Laboratory Report, LA-13070-MS.

[36] W. Fan, P. Qiao. 2011. “Vibration-based damage identification methods: A review and comparative study,” Structural Health Monitoring, 10(1): 83–111.

[37] S. Das, P. Saha, S. K. Patro. 2016. “Vibration-based damage detection techniques used for health monitoring of structures: a review,” Journal of Civil Structural Health Monitoring, 6: 477–507.

[38] G. F. Gomes, Y. A. D. Mendez, P. S. L. Alexandrino, S. S. Cunha Jr., A. C. Ancelotti Jr. 2019. “A review of vibration based inverse methods for damage detection and identification in mechanical structures using optimization algorithms and ANN,” Archives of Computational Methods in Engineering, 26: 883–897.

[39] N. F. Alkayem, M. Cao, Y. Zhang, M. Bayat, Z. Su. 2018. “Structural damage detection using finite element model updating with evolutionary algorithms: A survey,” Neural Computing and Applications, 30(2): 389–411.

[40] Q. W. Yang. 2009. “A numerical technique for structural damage detection,” Applied Mathematics and Computation, 215(7): 2775–2780.

[41] G. Ghodrati Amiri, A. Zare Hosseinzadeh, A. Bagheri, K. Y. Koo. 2013. “Damage prognosis by means of modal residual force and static deflections obtained by modal flexibility based on the diagonalization method,” Smart Materials and Structures, 22(7): 075032.

[42] A. Bagheri, A. Zare Hosseinzadeh, P. Rizzo, G. Ghodrati Amiri. 2017. “Time domain damage localization and quantification in seismically excited structures using a limited number of sensors,” Journal of Vibration and Control, 23(18): 2942–2961.

[43] H. P. Chen. 2010. “Mode shape expansion using perturbed force approach,” Journal of Sound and Vibration, 329: 1177–1190.

[44] R. J. Guyan. 1965. “Reduction of stiffness and mass matrices,” AIAA Journal, 3: 380–380.

[45] A. Zare Hosseinzadeh, A. Bagheri, G. Ghodrati Amiri, K. Y. Koo, “A flexibility-based method via the iterated improved reduction system and the cuckoo optimization algorithm for damage quantification with limited sensors,” Smart Materials and Structures, 2014; 23(4), 045019.

[46] A. Zare Hosseinzadeh, G. Ghodrati Amiri, S. A. Seyed Razzaghi, K. Y. Koo, S. H. Sung. 2016. “Structural damage detection using sparse sensors installation by optimization procedure based on the modal flexibility matrix,” Journal of Sound and Vibration, 381: 65–82.

[47] N. Zhang. 1995. “Dynamic condensation of mass and stiffness matrices,” Journal of Sound and Vibration, 188: 601–615.

[48] M. I. Friswell, S. D. Garvey, J. E. T. Penny. 1997. “Using iterated IRS model reduction techniques to calculate eigensolutions,” Proceedings of 15th International Modal Analysis Conference, 1537–1543.

[49] J. C. O’Callahan, P. Avitabile, R. Riemer. 1989. “System equivalent reduction expansion process,” Seventh International Modal Analysis Conference (IMAC), Las Vegas, Nevada, USA.

[50] C. V. S. Sastry, D. R. Mahapatra, S. Gopalakrishnan S, T. S. Ramamurthy. 2003. “An iterative system equivalent reduction expansion process for extraction of high frequency response from reduced order finite element model,” Computer Methods in Applied Mechanics and Engineering, 192(15): 1821–1840.

[51] Q. W. Yang. 2009. “Model reduction by Neumann series expansion,” Applied Mathematical Modelling, 33: 4431–4434.

[52] K. Y. Koo, S. H. Sung, H. J. Jung. 2011. “Damage quantification of shear buildings using deflections obtained by modal flexibility,” Smart Materials and Structures, 20(4): 045010.

[53] B. Peeters, G. De Roeck. 1999. “Reference-based stochastic subspace identification for output-only modal analysis,” Mechanical Systems and Signal Processing, 13(6): 855–878.

[54] B. R. Seshadri, T. Krishnamurthy. 2017. “Structural health management of damaged aircraft Structures using digital twin concept,” 25th AIAA/AHS Adaptive Structures Conference, Grapevine, Texas, USA, 9–13 January 2017.

[55] A. Bagheri, O. E. Ozbulut, D. K. Harris, M. Alipour, A. Zare Hosseinzadeh. 2019. “A hybrid experimental-numerical approach for load rating of reinforced concrete bridges with insufficient structural properties,” Structure and Infrastructure Engineering, 15(6):754–770.

[56] S. H. Sung, K. Y. Koo, H. Y. Jung, H. J. Jung. 2012. “Damage-induced deflection approach for damage localization and quantification of shear buildings: validation on a full-scale shear building,” Smart Materials and Structures, 21: 115013.

[57] ABAQUS, C. A. E. 2019. “User’s manual.” Abaqus analysis user’s manual.

[58] ARTeMIS Operational Modal Analysis, Structural Vibration Solution A/S, Denmark, version 5, 2016.

[59] A. B. Baggeroer, W. A. Kuperman, P. N. Mikhalevsky. 1993. “An overview of matched field methods in ocean acoustics,” IEEE Journal of Oceanic Engineering, 18: 401–424.

[60] K. L. Gemba, W. S. Hodgkiss, P. Gerstoft. 2017. “Adaptive and compressive matched field processing,” Journal of the Acoustical Society of America, 141(1): 92–103.

[61] J. D. Tippmann, X. Zhu, F. Lanza di Scalea. 2015. “Application of damage detection methods using passive reconstruction of impulse response functions,” Philosophical Transactions of the Royal Society A, 373(2035): 20140070.

[62] L. Chehami, J. de Rosny, C. Prada, E. Moulin, J. Assaad. 2015. “Experimental study of passive defect localization in plates using ambient noise,” IEEE Transactions on Ultrasonics, Ferroelectrics, and Frequency Control, 62: 1544–1553.

[63] X. Wang, M. S. Ghidaoui. 2018. “Pipeline leak detection using the matched-field processing method,” Journal of Hydraulic Engineering, 144(6): 04018030.

[64] E. Lubeigt, S. Rakotonarivo, S. Mensah, J.-F. Chaix, F. Baqué, W. A. Kuperman. 2019. “Passive structural monitoring based on data-driven matched field processing,” Journal of the Acoustical Society of America, 145(4): EL317–EL322.

[65] R. Cui, G. Azuara, F. Lanza di Scalea. 2020. “Composite elastic property identification through guided wave inversion and damage detection by data-driven process,” Proceedings of SPIE 11381, Health Monitoring of Structural and Biological Systems XIV, 113810I.

[66] J. Capon. 1969. “High-resolution frequency-wavenumber spectrum analysis,” Proceedings of IEEE 57(8): 1408–1418.

[67] J. N. Maksym. 1979. “A robust formulation of an optimum cross-spectral beamformer for line arrays,” Journal of the Acoustical Society of America, 65: 971–975.

[68] H. Cox, R. M. Zeskind, M. M. Owen. 1987. “Robust adaptive beamforming,” IEEE Transactions on Acoustics, Speech, and Signal Processing, 35: 1365–1376.

[69] S. U. Pillai, B. H. Kwon. 1989. “Forward/backward spatial smoothing techniques for coherent signal identification,” IEEE Transactions on Acoustics, Speech, and Signal Processing, 37(1): 8–15.